Airborne SAR/IfSAR for Mapping in Urban Areas

By

Mr. Thongthit Chayakula

Ph.D. in Remote Sensing

Department of Geomatic Engineering

University College London

September 2003

ProQuest LLC
789 East Eisenhower Parkway
P.O. Box 1346
Ann Arbor, MI 48106-1346

Acknowledgement

First of all, I would like to thank my supervisor, Professor Ian Dowman for his patience and willing help during my whole research. He has been a valued guide and has provided instructive feedback and continuous assistance. You are the best!

And for everybody in the Department of Geomatic Engineering, UCL, it's always been warm and wonderful since I first arrived. We have been through good and not so good times together. Everyone of you has been a fantastic and very generous helper. I salute you all from the bottom of my heart.

The Intermap Technologies, I thank you very much for providing the STAR-3i SAR/IfSAR data. Without you, this thesis is not possible.

I would also like to thank the Royal Thai Government and Chulalongkorn University for funding me to study in the UK. And this is extended to the staff at the Department of Survey Engineering for both academic and non-academic advice.

For my friends, wherever you are, London, Bangkok, Warwick, Enschede, Kobe, Sydney, Los Angeles, ..., even in cyberspace. Thank you very much, you guys are such wonderful friends.

Finally, a very warm thank you for my family. I thank you very much for your support in every possible way, for your patience, care and love. I love you, Mom and Dad.

And like many people would say " .....They think it's all over..... .....It is now!!!!"

Airborne SAR/IfSAR for Mapping in Urban Areas

Mr. Thongthit Chayakula

Ph.D. in Remote Sensing

University College London

Abstract

There are many problems in topographic mapping in an urban area. Traditional land survey is a very time consuming technique and can be very expensive. Photogrammetry is a popular choice but there are some problems such as clouds and limited operational time. Since Synthetic Aperture Radar, (SAR), is an active remote sensing system and its signal can penetrate through clouds, it can be operated at any time of day and is a independent of the weather. SAR could be a good solution for topographic mapping in an urban area. Combining SAR data and Interferometric radar technology can provide enough information for topographic mapping. Information can be extracted from SAR intensity Image. This thesis focuses on feature extraction and classification for topographic mapping in an urban area from airborne interferometric SAR data. A new algorithm is described which is simple and practical but yet very efficient for feature extraction and for object–based feature classification. An adapted Canny-Petrou-Kittler algorithm is applied for edge detection. Since the algorithm provides good detection, good localization and only one response to a single edge, it is an ideal edge detection for dense urban areas. Since the SAR image is noisy by its nature, small weak edges are expected. The modified non-maximal technique is also proposed to reduce unwanted edge. The technique of generation of bald earth DEM is proposed to obtain a normalised DEM for feature extraction. Region growing from edge detection is then applied to extract a more accurate shape of the feature and generate feature surface by using topographic parameters. The extracted feature is then classified by object-oriented classification technique, in which the classification is performed at object level not pixel level. And at the end of the process 3D city model can be produced.

Contents

List of Figure and Table

List of Figure

List of Table

I. Introduction

1.1 Motivation

In the past decade, there have been major developments in information technologies. Information has become the key for every business; we are now living in the world of information technology. Since Geographic Information System, GIS, has been widely used for many applications, maps have become more significant and contain more valuable information. Information about position plays a vital role in many applications, ranging from emergency services, mobile phone coverage, maintenance services to pizza delivery.

Since there have been rapid changes and construction developments, especially in an urban area, it is necessary to have a system that is able to produce and/or update maps in order to keep up with changes in the real world. There are many techniques and systems that can be used to produce maps in urban areas. Techniques range from land survey to satellite image processing in which the price can range from thousands to millions of pounds. The user has to choose which method is suitable for his needs and budget.

Until now Synthetic Aperture Radar (SAR) has successfully proved to be useful for general mapping. By deriving the third dimension from SAR data, Interferometric SAR (IfSAR) is proving to be even more beneficial. Interferometric SAR is a continuing development of SAR processing for generating Digital Elevation Models (DEMs). SAR and IfSAR systems are capable of providing radar intensity images and a digital elevation model, which are the two main components for producing topographic maps.

In this thesis, a technique for applying airborne SAR/IfSAR data for topographic mapping in an urban area is proposed. The research also includes studies about radar imaging in an urban area, edge detection, feature classification as well as generation of bald earth DEMs. This is to maximise the uses of airborne SAR data for topographic mapping in an urban area. The

technique is proposed to be an alternate choice for topographic mapping in an urban area.

1.2 Objectives

Not much research has been in undertaken the use of SAR and IfSAR in the urban area for topographic mapping. Most present research concentrates on the use of SAR/IfSAR for analysis of natural elements such as crop or forest or in the mountainous area. Moreover, the application of SAR/IfSAR for topographic mapping has mainly been on small-scale mapping, this is because the accuracy of the systems must be assumed. With the most recent research on the accuracy of modern SAR/IfSAR technologies, it has been proved that the accuracy of the SAR and IfSAR are in the acceptable range for topographic mapping. Theoretically, the SAR Interferometry system is capable of providing the accuracy of the DEM at millimetre scale. But practically, the best accuracy now provided by the system is around 30cm, depending on terrain type. Combined with its weather and time dependent characteristics, SAR/IfSAR can be described as a potential system for topographic mapping in an urban area. In order to maximise the potential of SAR/IfSAR data for topographic mapping in urban areas. The objectives of this research are:

- To demonstrate the use of SAR/IfSAR as a strong alternate system for mapping in urban areas.
- To investigate effects and phenomenon presented in applying SAR/IfSAR in urban areas.
- To develop new techniques of Feature Extraction for airborne SAR/IfSAR as well as generation of Bald Earth DEM.
- To apply a technique of Feature-Based Classification to classify the extracted features.

The main achievements of this research is to slow that 3D city model of urban areas can be generated by solely using airborne SAR/IfSAR data. Since SAR intensity image and IfSAR DEM are from the same sensor at the same observing time, co-registrations between datasets are not needed.

Another significant achievement of this research is that new techniques of extraction and classification of features from airborne SAR/IfSAR data have been developed. Even though there are many feature extraction and classification techniques, new techniques are developed to be suitable to characteristics for the SAR/IfSAR.

The top achievement of this research, which combines together with other achievement, is to demonstrate that airborne SAR/IfSAR data can be used for mapping in urban areas.

1.3 Historical Background of SAR

Since the invention of RADAR (Radio Detection And Ranging) during the Second World War, it has been recognised as a tool for detecting and tracking of targets such as aircraft and ships. Ground-based radar systems were initially restricted to military applications. Some earlier radar systems were used for military reconnaissance purposes. The radar was used extensively to support night time bombing during the war. After the war, Side Looking Airborne Radar (SLAR) was developed for terrain surveillance. SLAR can produce imagery at resolutions around 10-20 meters in range. Perpetually cloud-covered tropical areas were mapped for the first time. SLAR had demonstrated the significant benefits of high-resolution radar imaging in mapping. In this case, the radar illuminates a strip of terrain parallel to the flight path. A cathode ray tube and film were used for data display and data recording. In order to achieve a high azimuth resolution in the image, the antenna must be very long. This weakness of an unrealistic antenna length led to the research in new radar technology, later called Synthetic Aperture Radar, SAR.

SAR is also a side-looking instrument like SLAR, but it employs more sophisticated digital signal processing techniques. The US armed forces in the 1950s for the first time demonstrated the fact that a higher azimuth resolution can be accomplished without limitation in range from sensor to ground and without the lengthy antenna. In the early days of SAR, a majority of the developments in SAR systems were funded by the US Department of Defence (DOD). However, there were also a number of civilian US. agencies and universities that were developing SAR. The first non-military airborne SAR system was designed by ERIM and NASA (which later evolved into spaceborne SAR systems for many planetary explorations) because technologies became more and more declassified from the late 1980s onwards. Civilian remote sensing based on SAR was conducted in North America and in many tropical regions, in which mapping was problematic, such as for Darien Province of Panama, Brazil and Columbia (FAO 1993).

SAR is a unique instrument in remote sensing that provides its own illumination source by emitting microwaves and recording their backscattered signals. A sophisticated signal processing system converts SAR signals and the time delay of backscattered energy into a high-resolution image. Since SAR is an active system and has its own illumination, it can be operated day and night and penetrate through the atmosphere, in contrast to other conventional instruments in remote sensing, which are mostly passive optical systems and suffer from cloud occlusion and sometimes from unfavourable solar illumination. In tropical rain areas, SAR may be troublesome, because of some minor dependency on humidity. SAR is a remote sensing instrument with possibilities to control its signal characteristics such as signal strength, frequency, polarisation, pulse repetition and etc., which can respond to type and geometry of the ground in a different way. These effects can induce synergy in remote sensing for deriving new parameters from SAR.

The radar signal is also sensitive to the slope of the terrain, giving a shading effect, which supports the interpretation or even the evaluation of elevation. This phenomenon occurs because the average ground reflectivity is a

function of the incidence angle for a given terrain type, and this average reflectivity is modulated by surface roughness of the ground for each image pixel.

The radar application has been expanded beyond just the mapping task. Radar is now being applied to many other disciplines such as glaciology, hydrology, agriculture, vegetation, environment monitoring and etc. Nowadays radar imaging is one of the crucial tools to deal with the monitoring of our changing environment.

One of latest areas of SAR technologies is Interferometric SAR, which is sometimes abbreviated as IfSAR or InSAR. Although, the theory of signal interference has been in practice for a long time in optical and applied physics, it first came into use in planetary exploration by NASA. L.C. Graham reported on the interferometric techniques to generate topography from SAR data in 1974 (Graham 1974).

Radar Interferometry is based on two image acquisitions of the same zone from slightly different positions of the sensor. The signal-phase shifting of the two antennas are then superimposed and mathematically interfered. The result leads to an interferogram that records only the differences in phase between the two original images. These phase differences give the altitude variation of each pixel and the basic product for digital elevation models. Modern technology in RF and digital electronics allows the deployment of complex imaging radar, not just single frequency, single polarisation, but multispectral, polarimetric systems. Interferometry provides the 3rd dimension into radar imagery with a satisfactory level of accuracy.

1.4 Radar Remote Sensing for Urban Environment

A radar sensor's capability to characterise the physical nature of the land cover over a large region is fundamental to many earth science investigations (Evans et al., 1988). Radar remote sensing provides very different but potentially

complementary information to visible and near infrared sensors (Forester et al., 1996).

Microwave radiation, being of a much longer wavelength than visible/infrared radiation, interacts with fundamentally different properties in the objects being observed, than the optical wavelengths (Schumann, 1996). Optical systems are more concerned with the chemical properties of the targets, whilst SAR imagery provides information on the dielectric properties of materials (Nasr & Vidal-Madjar, 1991). Radar has the ability to penetrate the surface of an object on land which optical wavelengths are unable to do. However, the interaction with microwaves beneath the water surface is substantially limited compared to optical (Schumann, 1996). Some of the differences and distinct advantages which radar has to offer over optical systems include:

i. Its longer wavelength gives it the advantage of being able to penetrate cloud, dusty conditions and often rain.
ii. Being an active system, it can operate at any time of the day or night.
iii. Illumination can be in the optimum direction and incident angle to enhance a desired feature.
iv. Radar systems provide additional information for identifying objects and mapping surface materials due to the backscatter intensity being predominantly determined by different properties of ground targets (such as moisture content and surface geometry).
v. The polarisation of the radar signal can be varied to investigate how different objects depolarise the signal.
vi. Radar's long wavelength enables it to penetrate, to a certain extent, into vegetation, or the terrain surface, enabling the subsurface characteristics to be studied (Xia, 1996).

Apart from their independence from the sun as a source of illumination, one of microwaves greatest assets is its capability to penetrate clouds, and to some extent rain as well as pollution haze, which generally occurs in big cities. Urban environments, like London, that are subject to a lot of rain, pollution haze, cloud cover and heavy congested day time air traffics, require radar systems as their primary method of remotely sensed data collection. This is especially so in tropical countries those are developing rapidly and required relatively fast, efficient information (Ulaby et al., 1981). These also being the regions where least is known about present terrain conditions (Xia & Henderson, 1997).

Microwave provides information about an object's physical structure and electro-magnetic properties. The depolarisation and spectral reflectivity of the radar backscatter from a surface provides information about the surface roughness, geometric structure, morphology and dielectric constant of the surface (Elachi, 1988). The two major characteristics of the object are being its geometric and dielectric properties (Schumann, 1996).

Three types of urban-related projects have been identified for which radar's weather independence can assist: (a) when postponement of data collection owing to bad weather would be unacceptable; (b) analysis of general land-use patterns for large cities; and (c) investigating large regions to determine the location and extent of small centres (Moore, 1968).

Moreover, SAR/IfSAR system could provide both intensity and height information all together in a single flight. SAR intensity image can provide crucial information for texture analysis, data model and speckle. It is also very useful for edge detection since radar signal is sensitive in the range direction, thus edge is quite distinguished in SAR intensity image.

Even though, IfSAR DEM is not directly observed from the sensor, unlike Lidar, but it can provide satisfactory level of accuracy for mapping. IfSAR DEM is actually Digital Surface Model (DSM) in which, height information is height of the terrain plus height of the feature. In order to get the height of the feature, bald earth DEM needs to be generated. Together with

texture information from intensity image and height for IfSAR, the SAR/IfSAR could effectively provide crucial information for mapping.

1.5 DEM for Topographic Mapping

DEMs have been used in many scientific disciplines. DEMs can be derived from different techniques and have different accuracies. In this section the techniques and accuracy of conventional methods will be summarised. This should help to prove the necessity of research on the use of SAR and IfSAR to fulfil some mapping requirements which cannot be done with other sensors.

The DEM data is not only needed for mapping, but also for keeping maps up to date or for change detection. A general purpose DEM is needed for planning, engineering feasibility studies and as base map for land use etc. A DEM is also important for many scientific purposes such as georeferencing satellite data, avionics navigation, telecommunication network planning and operating, hydrological and infrastructure planning, building extraction which will be described in this thesis, etc. There are many ways to produce a DEM. The user has to choose between the possibilities, which largely depend on expense and the required accuracy. For terrain mapping DEM accuracy requirement can range from centimetres for local engineering project to hundreds of meters for global mapping.

1.5.1 DEM Acquisition Technique

There exist many technologies to acquire area coverage of terrain height. Some methods are not complicated and do not need expensive instruments and/or highly qualified personnel. However, they cannot provide a good level in productivity and automation. Some of the techniques need an additional survey effort onsite and others need expensive acquisition equipment and a lot of post-processing e.g. photogrammetry.

Terrestrial surveying is a classical technique and is the most accurate method to obtain ground elevation. Because of the limitation of technique direct access in the field is a must and can be expensive. Therefore terrestrial DEM acquisition is suited only for large-scale mapping or a local engineering project.

Photogrammetry has the advantage that it can remotely explore a whole region. Only a small amount of fieldwork is needed for establishing some ground control points. A cluster of height points can be measured from the stereo image pair. When successive photo strips are exploited, a larger coverage DEM can be rapidly acquired by a photogrammetric instrument or analytical plotter in the office. Expensive equipment and also well-qualified staff are needed in this method of DEM acquisition.

Laser profiling and Lidar have recently played a new role in DEM generation. The systems are based on a laser distance measurement instrument, which is vertically installed on an aircraft and directed perpendicular or near perpendicular to the ground. The height resolution is dependent on wavelength and timing resolution. The systems can produce DEM with high accuracy and can be used in urban areas, where discontinuities of man-made objects can be determined. The intensity of the backscattered signal can also be used to produce an intensity map, which reflects the different features on the ground. The systems can be said to be powerful three dimensional mapping instruments with high resolution.

Deriving terrain height from radar data has aroused interest analogous to radar mapping for planimetry and has been started on a broad scale since the last decade. There are currently three main methods to derive elevation from radar: SAR stereo mapping, shape-from-shading and interferometric processing.

SAR stereo mapping can be achieved through the extraction of three-dimensional geometric data from radar stereo pairs. There are problems relating to the matching techniques and the methods for converting stereo image measurements into geometric information about the object. Amongst other mathematically complicated methods, the selected overlap can be also stereoscopically measured in an analogous way to stereo photogrammetry.

Mapping of lunar features from Apollo-17 imaging radar and the SIR-B mission on the earth are one of the most successful missions with height accuracy of 100m and 10m respectively.

The shape-from-shading makes use of the signal reflectivity as function of terrain slope. This phenomenon can be utilised to calculate slope from reflectivity. If contiguous slopes are integrated, an array of heights can be achieved. However the reflectivity is very difficult to model. It depends on many unpredictable factors other than slope such as vegetation cover and surface roughness. Modelling is even harder in the case of inhomogeneous surface texture, which results in inconsistent reflectivity. Shape-from-shading also needs some type of boundary values or external terrain low-frequency information to succeed.

Interferometric SAR processing can give the best height accuracy in the level of centimetres or millimetre. SAR Interferometry has just begun to be routinely a help in the last few decades and can give the highest accuracy compared to other SAR-derived DEMs. It is probably the only method which gives global coverage without gaps caused by weather conditions. It can be used for global DEM acquisition. And this will be discussed in the later part of this thesis.

Vertical accuracy and sample spacing, which together contribute to the perceived 'detail', are two major metrics deriving the cost and the applicability of DEM products. In Figure 1.1, the unit price of DEM products is shown as a function of vertical accuracy. For relative comparison, the relationship of satellite based DEM products for STAR-3i IfSAR and generic Lidar are shown. Because costs and specifications are often project-specific, there is a broad range for any data type but the trend in the graph is clearly shown, the higher the accuracy, the higher the price.

Even though, Lidar and Aerial Photogrammetry are capable of providing very high vertical accuracy, but both systems are not able to cover the area as much as airborne SAR/IfSAR. It could be said that Lidar and Photogrammetry are more suitable for small area mapping, in which required a very high accuracy

while airborne SAR/IfSAR is more suitable for medium area mapping, in which medium vertical accuracy is required.

It is not only accuracy that SAR/IfSAR couldn't provide at the level of Lidar and photogrammetry, there are also some other limitations of applying SAR/IfSAR for mapping. For example, by the nature of both SAR intensity image and IfSAR DEM, they are noisy and contain many artefacts. There are also problems of radar shadow, radar layover, which are not present in Lidar data. There is also problem of occlusion. It results in the lost information, especially in urban areas, where there are a lot of small details on the ground. But these problems, even though causing some difficulties during the processing, can be eliminated before or during the processing. And it is important to configure every sensor to find the most suitable for a particular job.

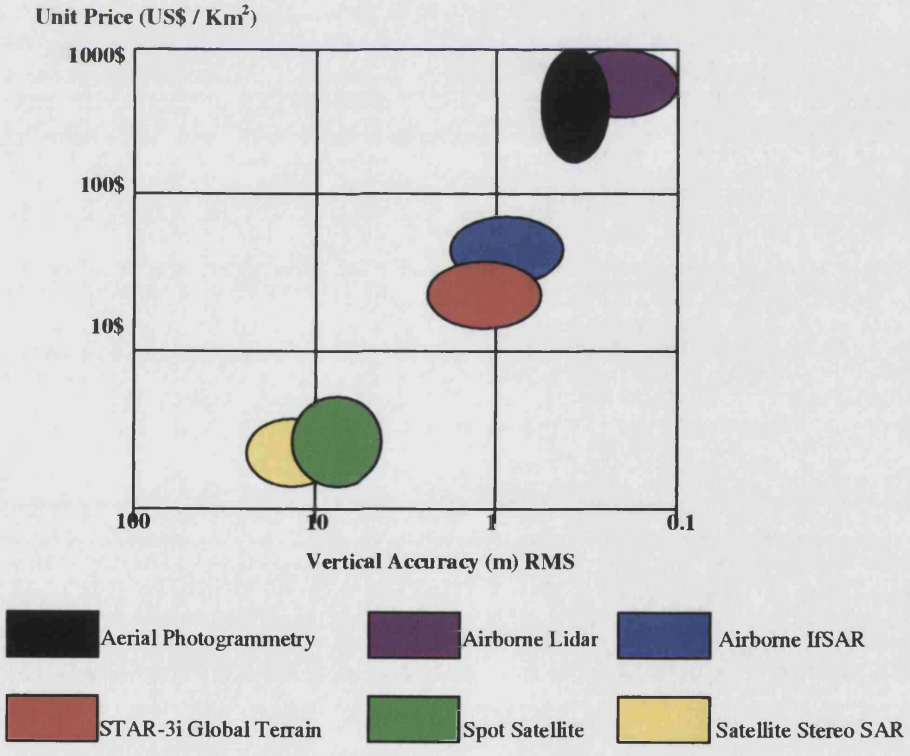

Figure1.1 Relationship between vertical accuracy and unit price of DEM generation techniques (Mercer and Schnick).

1.5.2 IfSAR and Lidar

In recent years, three-dimensional mapping products in the form of DEMs have become much more available due to the implementation of Lidar and IfSAR technologies. Both systems share a number of common features and also number of differences, which are going to be discussed next.

Firstly, common features; they are active remote sensing systems in capable of creating elevation model of the terrain by transmitting pulses and receiving the back-scattered returns. Both systems measure the 2-way time-delay from the transmitting element to the scattering elements and convert this to a range measurement. Moreover, they are equipped with highly accurate positioning data in the form of on-board INS/GPS systems that are used to support the computation of the coordinates of the scattering objects. And the ground swath of data coverage depends on the flying height of the platform. Furthermore, both systems respond to the first surface of contact (assuming it is a solid surface), which may be the bare terrain itself or objects such as buildings resting upon the terrain. The resulting model is usually referred to as a Digital Surface Model, DSM. A goal of users of both types of data is often to create a bald earth DEM from the DSM.

Secondly, the differences; IfSAR wavelengths are capable of penetrating cloud haze, etc. Lidar wavelengths, as used in most mapping systems, are in the near IR (~ 1nm), do not penetrate cloud and are heavily absorbed by water. Furthermore, Lidar samples are 'spot-like' compared to IfSAR's 'area-like' elevation samples. The Lidar illuminates a spot on ground with diameter ranging from 10-100 cm, depending on altitude and other factors. The spot separation is usually 2-5 meters. The resulting data set is an irregular or semi-regular grid of (x,y,z) coordinates. For visualisation and other purposes, these are usually incorporated into a regular DEM using interpolation. IfSAR, on the other hand, creates a regular grid of elevation samples. All the scattering elements within each of the contiguous resolution cells contribute to the observed elevation of that cell. The resulting DEM samples are therefore a result of integration rather

than interpolation. In the case of STAR-3i, the interferogram has undergone some filtering in the upstream stage, so that the sample spacing at the output is usually 3 meters, which is twice the width of the fundamental resolution unit. All other factors being equal, a Lidar DEM would look different than an IfSAR DEM in areas of rapid terrain change due to this interpolation versus integration factors.

1.5.3 DEM Accuracy

DEM acquisition techniques can produce DEMs with differences in accuracy. The mapping community is also interested in other issues like coverage, feasibility and price. Data volume is another important aspect of DEM acquisition. A large volume of DEM data is expensive and difficult to handle with conventional computers. A compromise must be found between height resolution, accuracy and application needs. Sometimes users have to be aware of processing capability due to the amount of DEM data, which is generally large.

The following Table 1. is a summary of techniques for DEM acquisition. It lists exclusively methods, which are applied to the surface of the earth covered with land. Other height acquisitions for sea surfaces are excluded.

DEM Acquisition Techniques	Coverage	Accuracy (Relative)
Terrestrial Survey	Local, large scale mapping	1cm – 10cm
Photogrammetry	Regional	10cm – 1m
Laser profiling	Regional to Local	0.5m-2m
SAR Interferometry	Regional to Global	5m – 20m
SAR Shape-from-shading	Regional to Global	Slope ≤ 2°, 22m
SAR Stereo Mapping	Regional	10-100m
Digitising from Map	Depends on map coverage	Depends on map used

Table1.1 Comparison of DEM acquisition techniques (Santitamnont 1998)

The following Table 1.2 shows DEM accuracy needed by different map scales.

Map Coverage	Scale	Grid Spacing for DEM	Accuracy of DEM (rms.)
Large Scale	≥1:10000	10m	< 1m
Topographic	1:25000 to 1:200000	25m to 100m	1m to 25m
Global	< 1:200000	30m to 5km	10m to 100m

Table 1.2 DEM accuracy requirement for mapping (Adopted from Dowman 1993)

And Table 1.3 also shows the requirement of height accuracy for cartographic mapping as defined by the U.S. National Map Accuracy Standards (NMAS).

Map Scale	Planimetric Accuracy (rms.)(m)	Height Accuracy (rms.)(m)	Cartographic Image Map Resolution (m)	Thematic Image Map Resolution (m)
1:250000	75	15-30	14	≤75
1:100000	30	6-15	6	≤30
1:50000	15	6	3	≤15
1:25000	7.5	3	1.5	≤7.5

Table 1.3. Requirement of images for mapping at various scales (Santitamnont 1998).

With the resolution and accuracy of the airborne SAR system and SAR Interferometry, the data from the system can provide good accuracy for topographic mapping. The scale of the map will be discussed in the later parts of this report as well as the features, which would be shown in the map since the area of interest is the urban area. The one of the main objectives of the project is to use the data from airborne SAR system, both SAR and IfSAR, for topographic mapping in an urban area.

1.6 Interferometry-related SAR Missions

Interferometric synthetic aperture radar observations provide a mean for obtaining topographic terrain maps from acquired data. DEM acquisition with interferometry is based on a SAR system simultaneously surveying the terrain with two slightly displaced antennas. The SAR antennas can be installed on the same platform or on a pair of different platforms. A series of complex algorithms are used to generate the DEM. Radar interferometry was primarily used in earth-based observation, planetary applications e.g. observation of Venus (Rogers and Ingalls, 1969), of the moon (Zisk 1972) and in mapping of elevation on Venus (Rumsey et al, 1974).

In the early 1970s AIRSAR was a radar system, in which a SAR instrument was mounted on a DC-8 NASA aircraft. Since then AIRSAR has grown beyond the JPL's airborne synthetic aperture radar programme. Later in 1986 a new airborne SAR system was tested on a NASA CV990 aircraft. Zebker and Goldstein (Zebker 1986) reported on the effort to derive topographic maps of a portion of San Francisco Bay area utilising data from an airborne SAR system. The derived map covers a region of approximately 11 km by 10 km with samples on an 11m-pixel size. The result was compared with US. Geological Survey contour map and showed a high degree of correlation between the two set of height.

SEASAT is the first JPL/NASA spaceborne mission to study the earth using imaging radar, SEASAT was specifically designed to observe the ocean. It was launched on June 38, 1978 and 100 days later suffered a massive short circuit in its electrical system and stopped functioning. One of the instruments onboard was synthetic aperture radar. Due to US military classification the data became only available to civilian users at the end of the eighties, thus more than 10 years after the launch the SEASAT data set reached the civilian research community. Goldstein et al 1990, first demonstrated an assessment of IfSAR in topography measurement, in which further development was followed in Zebker 1992, Lin 1992.

The Topographic Synthetic Aperture Radar, TOPSAR is an aircraft radar interferometer initiated by NASA. TOPSAR is a single pass interferometer and can rapidly collect the topography by flying over the region in only one flyover. The two TOPSAR antennas are mounted nearly vertically on the left side of the aircraft.

Shuttle Imaging Radar-C, SIR-C is the successor of the radar experiment of the NASA shuttle missions, SIR-A (1981) and SIR-B (1984). The third Shuttle Imaging Radar is a joint project between Jet Propulsion Laboratory (JPL) and the German Aerospace Research Establishment (DLR) with the Italian Aerospace Agency (ASI), who supplied the X-SAR instrument. This mission was called SIR-C/X-SAR, which is the first spaceborne radar with the ability to transmit and received horizontally and vertically polarised waves at both frequencies. The SIR-C/X-SAR is a successful multi-frequency and multi-polarisation radar mission and has provided a powerful data set for global environmental research. Interferometric processing has been accomplished through a processor at DLR Germany and was reported in Moreira et al 1995.

Due to the success of the 3rd shuttle mission the 4th mission was launched in February 2000. The Shuttle Radar Topography Mission, SRTM is a single pass interferometer developed by NASA and National Imagery and Mapping Agency (NIMA) along with the DLR and ASI. The radar system is installed in the shuttle's cargo bay and the two X-band antennas are mounted on a 60m mechanically extensible mast. A second C-band from the former partners (DLR and ASI) is augmented to primary C-band SAR system. The X-band is designed to produce higher resolution topographic measurements in strips nested within the C-band coverage. The Shuttle Radar Topography Mission collected data over most of the land surfaces that lay between 60 degrees north latitude and 54 degrees south latitude. That's about 80 percent of all the land on Earth.

The Canadian's effort recently reported that repeat pass interferometry with RADARSAT is also feasible. The data was obtained as a RAW signal product and processed to single look complex (SLC) form on dtSAR, a workstation based SAR processor developed at German DLR. Interferometric

SAR with RADARSAT is a repeat pass type with a repeat cycle of 24 days and allow the extraction of topographic information. The other Canadian achievement is the simulation with its predecessor airborne SAR (Cumming 1989, 1990 and Laurence 1992).

Interferometry with the European ERS-1 (1991) of the ESA now tends to be a routine mapping procedure. This success is largely due to the stability of the satellite platform and to the availability of a large number of data. Due to the early mission phases of ERS-1 (1991-1995) users can opt for the SAR pair with a repeat cycle of 3, 35 and 168 days. With this orbit strategy about 50% of the repeated scenes can fulfil the interferometric processing criteria (Solass 1994). Based on this data set many DGMs on different test sites were successfully generated by different working groups (Guarieri 1993, Hartl 1993, Prati 1994, Kenyi 1996). After the launch of ERS-2 in 1995, ESA was then operatingERS-1 and ERS-2 in tandem, in which the two satellites flew in nearly the same orbit over the same area in less than one day. In this context, ESA released an announcement of opportunity to scientific academic community to evaluate the potential of SAR interferometry for different disciplines. The TANDEM helped eliminate one of the most problematic temporal de-correlation problems, which is a problem with repeat pass interferometers.

1.7 Summary and Overview of Thesis

Chapter 2 will provide the basic principles and information about SAR and IfSAR as well as the studies about radar imaging and radar issues in an urban area. In the later part of the chapter, information about speckle and SAR data models will be given.

Chapter 3, from the results of the studies of SAR/IfSAR in an urban area and data model in the previous chapter, this chapter will deal with SAR/IfSAR pre-processing and speckle reduction. This also includes a comparison of speckle reduction algorithms and analysis of technique. But it will not go deeper in the

topic of speckle reduction beyond finding the appropriate technique, which suits the data.

Chapter 4 introduces the main processing procedure. This chapter describes the feature extraction process. There are some references to the previous research about feature extraction and generation of bald earth DEM at the beginning of the chapter. The whole process starts with the generation of bald earth DEMs for IfSAR DEM in order to obtain the Digital Surface Model (DSM). Then, the technique of edge detection from intensity images will be assessed, followed by region growing from edge detection on the DSM. These techniques are the major parts to demonstrate that SAR/IfSAR system is a complete system to extract features and do not need any method of data fusing from other sensors.

Chapter 5, Object-based-classification and texture analysis techniques will be described by using information from the part of data model in chapter 2, in order to classify the extracted features. The main concept is to find the most suitable data model for each type of feature, mainly to separate buildings from trees. Some data models will be analysed such as Gamma distribution, K-distribution and log normal distribution. And at the end the 3D city model of any area can be produced. With the addition of OS Landline data, a final product will be more realistic.

Chapter 6, the whole process will be applied on the west of London dataset and the results will be shown in this chapter. There will be an accuracy assessment of the results on both quantitative and qualitative basis. The process will also applied on the Shrewsbury dataset for comparison.

Chapter 7, the conclusion and discussion will be stated in this chapter. The developed techniques try to achieve a goal of mapping an urban area by using airborne SAR/IfSAR data. By developing new techniques of edge detection, non-maximal for elimination of small weak edges, generation of bald earth DEM,

region-growing from edge detection and object-oriented classification, a final result would be a classified 3D model of the area. This will also show the potential and limits of SAR/IfSAR data for mapping in urban areas.

Chapter II.

Basic Principle of SAR and IfSAR System of Urban Areas

2.1 Principle of SAR and IfSAR

2.1.1 Synthetic Aperture Radar

Imaging radar works very like a flash camera in that it provides its own light to illuminate an area on the ground and take a snapshot picture, but at radio wavelengths. A flash camera sends out a pulse of light (the flash) and records on film the light that is reflected back at it through the camera lens. Instead of a camera lens and films, radar uses an antenna and digital computer tapes to record its images. In a radar image, one can see only the light that was reflected back towards the radar antenna.

Typical radar measures the strength and round-trip time of the microwave signal that are emitted by a radar antenna and reflected off a distance surface or object. The radar antenna alternately transmits and receives pulse at particular microwave wavelengths and polarization. At the Earth's surface, the energy in the radar pulse is scattered in all directions, with some reflected back toward the antenna in a specific polarization. These echoes are converted to digital data and passes to a data recorder for later processing and display as an image. Given that the radar pulse travels at the speed of light, which is constant, it is relatively straightforward to use the measured time for the roundtrip of a particular pulse to calculate the distance or range to the reflecting object. The chosen pulse bandwidth determines the resolution in the range (cross-track) direction. Higher bandwidth means finer resolution in this dimension as it can be seen in Figure 2.1.

The length of the radar antenna determines the resolution in the azimuth (along-track) direction of the image: the longer the antenna, the finer the resolution in this dimension. Synthetic Aperture Radar (SAR) uses a techniques to synthesize a very long antenna by combining signals received by the radar as it moves along it's flight track. Aperture means the opening used to collect the

reflected energy that is used to form an image. In the case of a camera, this would be the shutter opening; for radar it is the antenna. A synthetic aperture is constructed by moving a real aperture or antenna through a series of position along the flight track. As the radar moves, a pulse is transmitted at each position; return echoes pass through the receiver and are recorded in an echo store. Because the radar is moving relative to the ground, the returned echoes are Doppler-shifted (negatively as the radar approaches a target, positively as it moves away), as SAR geometry is shown in Figure 2.2. Comparing the Doppler-shifted frequencies to a reference frequency allows many returns signals to be focused on a single point, effectively increasing the length of the antenna that is imaging that particular point. This focusing operation, commonly known as SAR processing, is now done digitally on fast computer systems. The trick in SAR processing is to correctly match the variation in Doppler frequency for each point in the image: this requires very precise knowledge of the relative motion between the platform and the imaged objects, which is the cause of the Doppler variation in the first place. Synthetic aperture radar is now a mature technique used to generate radar images in which fine detail can be resolved. SAR system provides unique capabilities as an imaging tool. Because they provide their own illumination, they can image at any time of day, regardless of sun illumination. And because the radar wavelengths are much longer than those of visible or infrared light, SARs can also see through cloudy and dusty condition that visible and infrared instrument cannot.

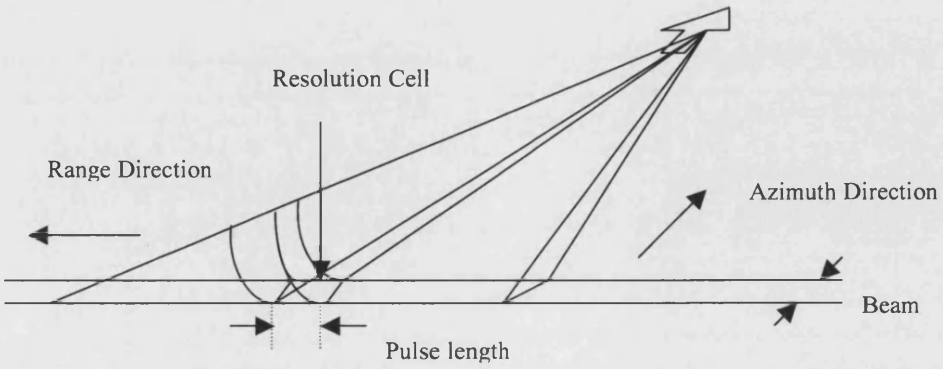

Figure 2.1 Determination of a resolution in range direction.

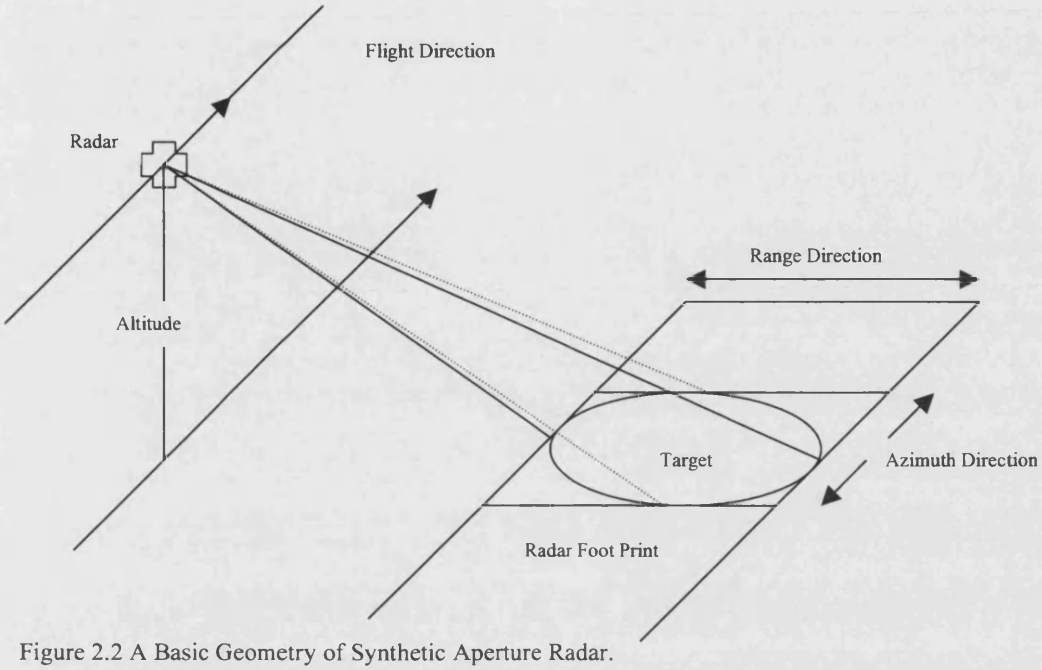

Figure 2.2 A Basic Geometry of Synthetic Aperture Radar.

There is one basic principle of radar imagery, which is central to this project. It is stated that coherent scene illumination, "input to a remote sensing radar from the scene is a linear summation of voltages from reflecting elements that are illuminated by a coherent EM wave field" (Henderson and Lewis 1998). This is to discriminate radar remote sensing from the optical sensors. Natural radiation emitted from an extended source, which is polychromatic, is used by most optical remote sensing systems. Such radiation has a random phase structure between any two arbitrary points in the illuminating field. The resulting reflected EM fields are incoherent. This means that their underlying phases are random, which implies that the combinations of reflections from more than one scene element add in power. In distinct contrast, for most radar, the illumination from each transmitted pulse is essentially monochromatic, emitted from a point source. This implies that the radiating field has structured phase fronts, which may be well represented from most purposes by spherical surfaces, centered at the radar. Thus EM illumination incident on the scene is coherent. This means that the reflections from more than one scene element combine through vector addition. Imagery is generated by processing over a signal ensemble comprised

of reflections from many pulses. If the radar is controlled so that the pulse sequence is mutually coherent, then the pulse-to-pulse phase structure can be exploited during processing. This is the case with a SAR. During observation interval, the relative phase of the reflected field will change if any element of the scene has changing reflectivity. A systematic phase change in the scene can be useful to a coherent radar; it is a basis for moving target detection and radar interferometry. But random phase change may lead to loss of image resolution.

Single Channel Image Types and Speckle Complex Image

At position (x,y), the primary geophysical quantity determining the SAR data is the complex radar reflectivity of the scene and the SAR provides a measurement of this reflectivity. When an electromagnetic wave scatters from position (x, y) on the Earth's surface, the physical properties of the terrain cause changes in both phase $\theta(x, y)$ and amplitude $A(x, y)$ of the wave. The SAR, in fact, measures the number pair $(A\cos\theta, A\sin\theta)$ in the in-phase and quadrature channels of the receiver, weighted by the SAR Point Spread Function, PSF. This estimate of the local reflectivity at each pixel can also be represented by the complex number $Ae^{i\theta}$; in this form, the SAR data are known as the *complex image.*

From the complex image a variety of other products can be formed. For example, images of the real part $A\cos\theta$, the imaginary part $A\sin\theta$, the amplitude A, the phase θ, the intensity $I = A^2$, or the log intensity $\log I$. The use of the intensity is, by analogy with measurements at optical wavelengths, synonymous with power or energy. The log image is also sometimes referred to as the dB image, since for calibrated data each pixel corresponds to a linearly scaled estimate of the backscattering coefficient σ^0, in dBs. The scaling will be unity only when the log image is formed by taking $10\log_{10}$ of each pixel in the calibrated intensity image.

For a properly calibrated system, these are all true measurements of the scattering properties of the Earth's surface, (except for those effects caused by

system noise), but virtually they produce quite different representation. Typically, the real and imaginary images show some structure but appear extremely noisy, the phase image is noiselike and shows no structure while amplitude, intensity and log images, though noisy, are clearly easier to interpret. Of these latter three image types, the amplitude and log images are often preferred since the large dynamic range of the intensity image can reduce the perception of detail.

The noiselike quality characteristic of these types of images and of those produced by other coherent imaging systems using lasers, sonar or ultrasound, is known as speckle. It must be stressed that speckle is *noiselike*, but it is not noise. It is a real electromagnetic measurement, which is exploited. Given that the SAR is making true measurements of the Earth's scattering properties, why do such effect arise? A simple model of how the world might appear to the radar suggests an answer. In distributed targets, each resolution cell is suggested to be as containing a number of discrete scatterers. As the wave interacts with the target, each scatterer contributes a backscattered wave with a phase and amplitude change, so the total returned modulation of the incident wave is

$$Ae^{i\theta} = \Sigma^{N}_{k=1}(A_k e^{i\theta k}) \qquad (2.1)$$

This summation is over the number of scatterers illuminated by the beam; it includes the weighting imposed by the SAR PSF and any attenuation effects caused by the scattering and propagation process. The individual scattering amplitudes A_k and phase θ_k are unobservable because the individual scatterers are on much smaller scales than the resolution of the SAR, and there are normally many such scatterers per resolution cell. This model has already been introduced in terms of small scattering facets and can also be considered in terms of elementary scattering volumes (Whitt et al 1990).

This simple discrete scatterer model is capable of much elaboration, forming the basis of the Neumann series expansion and approaches springing form it, such as the Born and distorted Born approximation (Firsch, Taylor

1972). These provide a mean of relating the observations to the physical properties of the scattering layer, such as the dielectric constant, shape and orientation of the scatterers. These possibilities are not exploited here but simply note that they can all be embodied in the formulation give as (2.1).

An immediate conclusion from Eq.2.1 is that the observed signal will be affected by interference effects as a consequence of the phase differences between scatterers. In fact, speckle can be understood as an interference phenomenon in which the principal source of the noiselike quality of the observed data is the distribution of the phase terms θ_k. To infer this distribution, note that the slant range resolution is typically many wavelengths across. Hence scatterers at different parts of the resolution cell will contribute every different phases to the return (2.1) even if their scattering behavior is identical. As a result, it could be thought of the phase θ_k as being uniformly distributed in $[-\pi, \pi]$ and independent of the amplitude A_k. The sum (2.1) then looks like a random walk in the complex plane, where each step of length A_k is a completely random direction. This problem has been thoroughly treated in Goodman 1984. For large numbers of statistically identical scatterers, the analysis reveals that:

1. The observed in-phase and quadrature components, $z_1 = A\cos\theta$ and $z_2 = A\sin\theta$, will be independent identically distributed Gaussian random variables with mean zero and whose variance $\sigma/2$ is determined by the scattering amplitude A_k that is, will have a joint *probability density function*, PDF given by:

   $$P_{z1,z2}(z_1, z_2) = [1/(\pi\sigma)]\exp[(-z_1^2 + z_2^2)/\sigma] \qquad (2.2)$$

2. The observed phase θ will be uniformly distributed over $[-\pi, \pi]$
3. The amplitude A will have Rayleigh distribution

   $$P_A(A) = (2A/\sigma)\exp(-A^2/\sigma)\ ;\ A \geq 0 \qquad (2.3)$$

   With mean value $\sqrt{\pi\sigma}/2$ and standard deviation $\sqrt{\sigma}(a-\pi)$. Another commonly used statistic is the coefficient of variation (CV) defined as the standard deviation divided by the mean. Hence, for amplitude data this takes the value $\sqrt{4/\pi} - 1$.

4. The observed intensity or power $I = A^2$ will have a negative exponential distribution

   $P_I(I) = 1/\sigma \exp(-I/\sigma)\ ; I \geq 0$ (2.4)

   With mean value and standard deviation both equal to σ, so that in this case CV=1.

5. The log intensity $D = \ln I$ has a Ficher-Tippett distribution (Arsenual and April 1976)

   $P_D(D) = e^D/\sigma \exp(-e^D/\sigma)$ (2.5)

   Whose mean value and variance are $\ln \sigma - \gamma_E$ and $\pi^2/6$, respectively. The symbol γ_E denotes Euler's constant whose approximate value is 0.57722 ref18. This distribution is easily converted to that for a properly normalize dB image, since it can be set that $D_n = 10\log_{10} I = (10\log_{10} e)D$ and hence $P_{Dn}(D_n) = 1/K\ P_D\ (D_n/K)$ where $K = 10\log_{10} e$. Notice that for the log intensity data, the variance is independent of the mean value, unlike the distribution (2.2) to (2.5). Hence, log data is often preferred as a means of standardizing or stabilizing the variance.

The distributions from 1 to 5 are of fundamental importance in handling SAR data. Notice that, with the exception of the phase distribution, they are completely characterized by a single parameter σ, which carries all the available information about the target. From 4, it can be seen that σ corresponds to the average intensity.

2.1.2 SAR Interferometry

Interferometry has been known in Physics and Optical Science for a long time. The interferometric method has been employed to make highly precise distance measurements using phase differences of a coherence light source from two sensor locations. Radar interferometry technology was used for the observation of planets and the moon from earth. The very first interferometric effort was made by Goldstein in 1965. The first attempt in airborne radar

interferometry with earth topography was reported by Graham1974. Since then, the interferometry concept has shown its potential for accurate reconstruction of terrain. The method has been constantly developed, for example, observation of planets and the moon from earth in 1965, observation of Venus from earth in 1969, elevation of the moon surface in 1972, measurement of Venus topography in 1974, airborne interferometry for topographic mapping survey in 1974, spaceborne interferometry with SEASAT in 1988 and etc (Santitamnont 1998).

If two SAR images from slightly different viewing angles are obtained, it will be shown that their phase difference can be used to generate the Digital Elevation Model. SAR interferometers can be categorized on the basis of their configurations into two major groups. The first type is single-pass interferometer, which can be done with radar with two antennas equipped on the same aircraft, or spacecraft and the latter type is a repeat-pass interferometer, in which there is only a single radar antenna. So it has to visit the same scene twice. The basic geometry of interferometric SAR is shown in Figure 2.3. Given two antennas A_1 and A_2, surface topography is given by h, altitude H above the ellipsoid, the baseline B, range to the target ρ, the look angle at target location θ and the angle of the baseline with respect to the horizontal α antenna 1 transmits and receives while antenna 2 receives at the same time as A_1 is defined by:

$$h = H - \rho \cos(\theta) \tag{2.6}$$

Based on the law of cosines, we can state that:

$$(\rho+\delta\rho)^2 = \rho^2 + B^2 - 2\rho B \cos(90-\theta+\alpha) \tag{2.7}$$

Where $\delta\rho$ is the difference on the to slant ranges and α is the orientation of the baseline with respect to the horizon. Solving equation (2.7) for ρ and substituting into equation (2.1) gives:

$$h = H - \{(\delta\rho^2 - B^2) / (2B\sin(\alpha-\theta) - 2\delta\rho)\} \cos(\theta) \tag{2.8}$$

Equation (2.8) reveals an obstacle when trying to determine $\delta\rho$ which is given by:

$$\delta\rho = \lambda\phi / 2\pi \tag{2.9}$$

Where λ is the radar wavelength and ϕ is the absolute phase difference between the two returns. ϕ can not be directly measured by the radar leading to ambiguities. The process of phase unwrapping is used to determine the integer portion of ϕ. After the phase unwrapping process, Digital Elevation Model is the result.

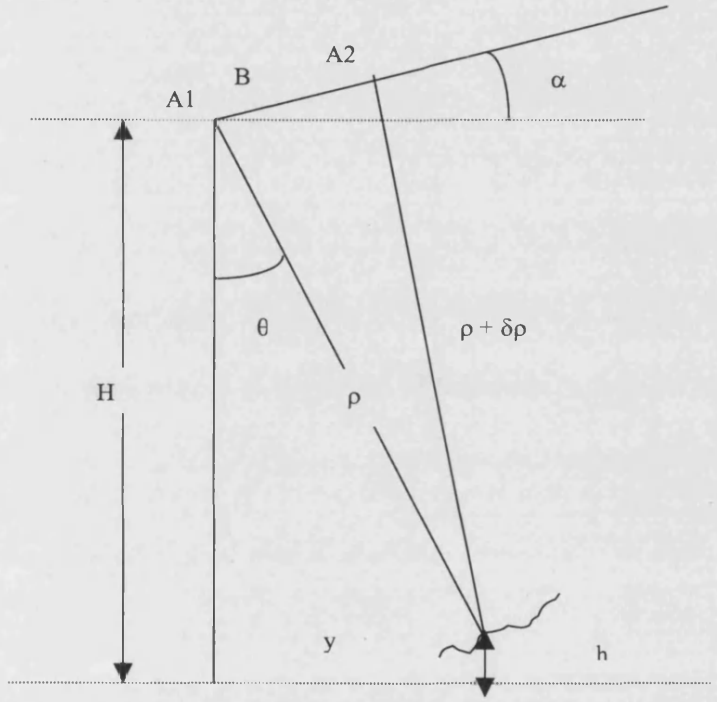

Figure 2.3 A basic configuration of SAR Interferometry.

Phase unwrapping is primarily a problem in the reconstruction of object surfaces in two-dimensional adaptive optics and physics. In the case of synthetic aperture radar processing, a new array of complex numbers is obtained by multiplying the individual pixel of the SLC (Single Look Complex) pair image with its conjugated pixel in the counterpart image. If the phase of each complex number is calculated and depicted as raster image, this kind of image will be called an interforogram or fringe image. This phase array in an interferogram is the array of rounded up interferometric phases. The wrapped interferometric phase has range from - π to π resulting from applying the arc-tangent function. Thus phase unwrapping is the task to reconstruct the interferogram or wrapped

interferometric phase array into array of full cycle interferometric phase one. In applied physics the wrapped phase is know as principal phase value.

Phase unwrapping in IfSAR is even more difficult when the interferogram has low phase to noise ratios or low coherence. Larger arrays of wrapped phase in the IfSAR array make the computing much longer than noise in similar problems in the applied physics. The result interferometric phase array will reflect the topography. With a correct geometric relation the interferometric phase array can be turned into the required DEM. Losing absoluteness of wrapped terrain is another consideration to shift and/or re-scale the unwrapped terrain. In most cases, the final DEM will be resampling to an equidistant raster and georeferenced in a national mapping coordinate system for integration with other geodata.

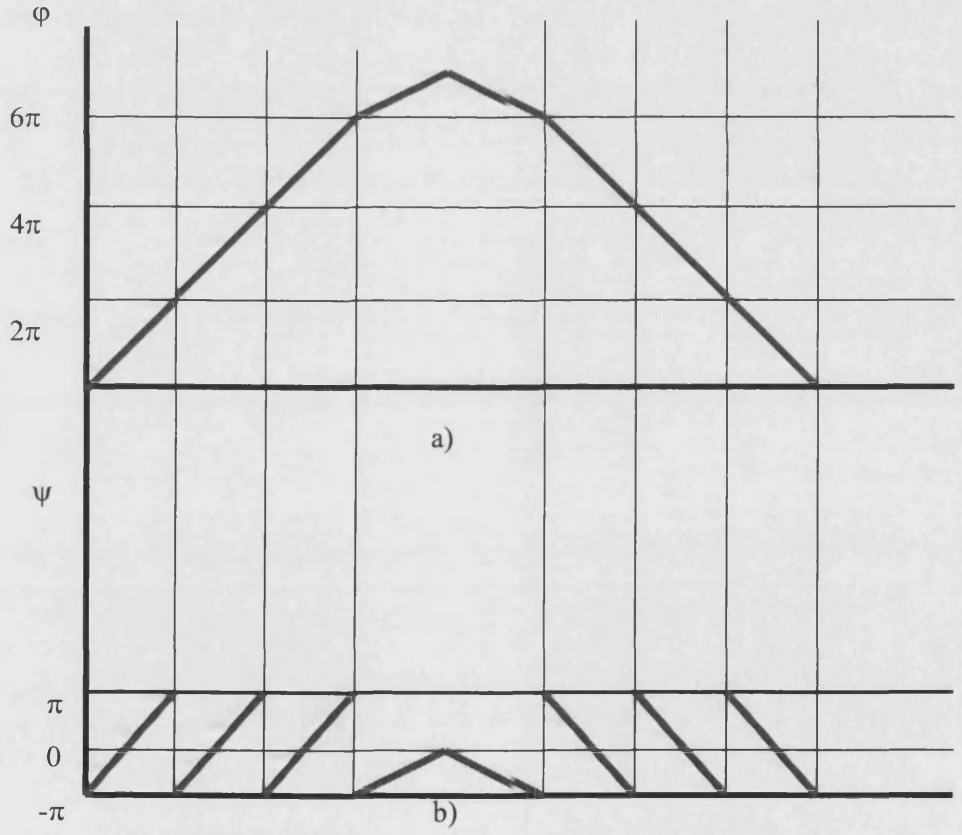

Figure 2.4 a) The unwrapped hill b) wrapped hill for IfSAR.

Two-dimensional (2D) phase unwrapping continues to find further applications in a wide variety of scientific and engineering areas. Goldstein et al 88 and Ghiglia et al 89 first highlighted some common problems and practical solutions for applying the phase unwrapping technique in radar imaging. Since then many phase unwrapping techniques have been suggested Takajo 1988, Goldstein 1988, Robinson 1993, Pritt 1994, Hartl 1995, Fornaro 1996, Pritt 1996, Sebker 1997, etc. Before phase unwrapping, filtering can be applied in order to remove the noise (Lin 1992, Genderen 1997). The proposed phase unwrapping methods can be divided into 2 groups:

- Deterministic method
- Numerical method

The deterministic phase unwrapping method is based on the idea of detection the abrupt changing phase from $-\pi$ to $+\pi$ in the case of decreasing slope or from $+\pi$ to $-\pi$ in the case of increasing slope. If the slope is increasing then a value of 2π is added to the current accumulating phase value and vice versa. The assumption that phase data is adequately sampled must be accepted. At the very first pixel an arbitrary value must be used as start value. Generally, zero is simply assumed. This implies that after phase unwrapping at least one height point value must be known for the offset of the whole height model.

In the following view graph "hill" is a simplified one-dimensional case of surface of phase variation. "Hill" could resemble a similar topography illustrating to help understanding the deterministic phase unwrapping technique.

In the figure 2.4a) the one-dimensional synthetic hill with phase increasing from 0 on the leftmost side to the maximum value of 7π and declining to 0 again is plotted. In the figure 2.4b) the corresponding principal phase array resulting from wrapping the corresponding phase value.

For the above simplified one-dimensional hill, the basic idea of deterministic phase unwrapping previously described can be easily applied. Beginning from the left side with an arbitrary starting height of 0 the height is summed up to the right. At the point where the value changes from $+\pi$ to $-\pi$ a

cycle of 2π is added. At the position beyond the middle of the 2.2b) the discontinuity where the value alters from $-\pi$ to $+\pi$ a cycle of 2π is now subtracted for the accumulated height at that position.

Later researches in two-dimensional phase unwrapping are placed in the mathematical framework of matrix algebra. Many phase unwrapping problems arising in adaptive optics deal with the solution of phase estimation with a relatively small grid, i.e. 64 by 64 pixel or less. The phase unwrapping can be formulated as a special of a second order *partial differential equation* (PDE).

The partial differential equations are classified into three categories hyperbolic, parabolic and elliptic depending on their definitions. In the case of the phase unwrapping solution it can be specified as an elliptic partial different equation. The elliptic partial differential equation can be further categorized into minor classes namely Laplace and Poisson equation. The Laplace's equation is similar to Poisson equation but $\rho(x, y) = 0$. Phase unwrapping can thus be solved by Poisson equation.

There are 2 type of interferometric SAR, which are single-pass interferometry and double-pass interferometry. For the single-pass interferometry the system has to fly over the target only once to collect the data. Most of the single-pass interferometry systems are airborne but still some spaceborne IfSAR system as well. For example, the NASA airborne interferometer, SIR-C, X-SAR is a single-pass interferometer. The signal transmitted by a signal antenna mounted under the right wing of the aircraft. The reflected energy from the ground is received by the right antenna and simultaneously the same signal is received by a second antenna mounted under the left wing. The antenna separation is about 11.1m for SIR-C. The Intermap STAR-3I system is another example for the airborne single-pass interferometer. The system uses 2 antennas installed on a Learjet. The data set used in this project is from this STAR-3I system which is developed by ERIM and operated by Intermap.

Another example of the single-pass interferometer is the spaceborne interferometer using in the Shuttle Radar Topographic Mission (SRTM). The SRTM uses a long boom for separation of the two antennas. The SAR system

and the primary antenna sit in the Space Shuttle's cargo bay, the other one is fixed on the end of the boom.

The double-pass interferometer deploys only one platform, on which is installed only one antenna and SAR system. The system must fly over the same area twice with slightly displaced orbits. The distance between previous visiting and repeating must be kept small to fulfill the interferometric condition, which is expressed by in terms of the baseline length. The signals from the two episodes over the same ground print are used for interferometric processing. The double-pass system is mostly used in spaceborne platform such as the SIR-C/X-SAR mission, the ERS1/2. There might be some ground changes during the second visit, which makes the signal correlation worse. Good geometric condition depends largely on highly precise orbital parameters from the two passes. But in the case of ERS1/2 tandem mission, they have identical platforms with the same radar instruments and systems, it provides the unique opportunity to fly over the same region within a short period of time. This is a solution to a problem of changes of the area during the period of 1st and 2nd visit. The repeat time of the tandem mission is one day.

2.2 Radar Issues in an Urban Area

2.2.1 Characteristic of Radar Remote Sensing

Electromagnetic waves interact with matter through different mechanisms, which are dependent upon the composition and structure of the object. Different mechanisms change the characteristics of the wave (e.g. Polarisation, intensity, direction) such that the properties of the object can be uniquely identified. Physical (slope, morphology, roughness, unhomogeneities) and electrical (dielectric constant) characteristics of the surface, and near subsurface, determine how the radar wave will interact with it (Elachi 1988). Since radar is an active system, the transmitted wave has a defined characteristic,

hence the changes which this wave undergoes following scattering from a surface provide information about the surface.

Microwave remote sensing gives information about the morphological properties of the imaged area, in contrast to knowledge about chemistry of the surface provided by optical remote sensing. This is one reason why radar is showing promising results in the urban area. There are varying factors affecting the intensity of the radar return from objects. The urban environment is a complex mixture of buildings, vegetations and other engineering structures. A building's size, shape, material and spatial layout influence the radar backscatter from an urban scene. The main factors determining the characteristics of radar returns from urban features are the radar system parameters, properties of the surface and environmental variables. Important radar system parameters includes the wavelength, polarisation, look angle, look direction and phase differences of the radar waves. Properties of surface features affecting radar signal returns include the complex dielectric constant, surface roughness and feature orientation. Orientation of features and terrain slope are important in relation to the look direction of the radar system, as the affect the intensity of the radar return. Feature orientation with respect to radar look direction is probably the most important factor with respect to radar interaction in the urban environment. Important environment variables include shape of the land, land cover classes and spatial patterns, vegetation cover, settlement history and local climate (Xia and Henderson, 1997).

The difference between the look angle and incidence angle must be noted. The look angle describes the angle between the horizontal plane at the radar and the line-of-sight to the object. The incidence angle is the local angle, to the normal, which radar contacts a surface feature, and hence depends on the orientation and shape of the object. Also, the look direction is the direction, which the radar is looking, projected onto the horizontal plane.

The wavelength of the radiation with respect to the surface roughness will determine if the scattering will be specular or diffuse. Specular scattering occurs when most of the radar wave is reflected in a mirror like fashion. For a

single flat surface most of the wave will reflect away from the sensor and backscatter will be very low. Energy dispersed in all directions is known as diffuse scattering. The amount of energy scattered in the different directions depends on the surface roughness and also the wavelength of the incident wave (Elachi 1988). For a rough surface, scattering will be uniform in all directions and hence, some of the radar wave will return to the sensor. The longer the wavelength, for a particular surface, the smoother the surface will appear. Rayleigh's criterion is one method of approximation the scattering results for a particular wavelength and surface roughness

$$\text{Rayleigh's criterion: } H \leq \lambda / (8\cos\theta) \qquad (2.10)$$

Where H is the root mean square height of the surface, λ is the wavelength, and θ is the incidence angle (Forster 1994). If H is less than the right hand side of the equation, the scattering will be predominantly specular. Here the incidence angle and look angle are the same if the surface is horizontal. This is an assumption of the flat earth surface.

The wavelength of the radiation will also influence the depth of signal penetration into a vegetation canopy or terrain surface (Xia and Henderson 1997). As stated above, Rayleigh's Criterion is also a function of incident angle. The greater the angle, the more specular the reflection. At large look angles on a radar image, most surface will appear quite smooth. At large incident angles most or all of the energy reaching a smooth surface will be reflected away from the radar system, while at small incident angles the specular reflection returns a lot of the energy to the receiving antenna. Rough surface produces reasonably strong intensity returns over a wide range of incidence angles. The look angle plays an important role in the urban environment. Its influence on range resolution affects settlement delectability. Small look angles produce a poor range resolution compared to larger angles. Higher resolution enables small settlements to be detected and small land cover classes to be mapped. However, larger look angles create more radar shadows concealing land cover.

A radar system can transmit and receive a horizontal (H) and/or vertical (V) polarised wave. The backscatter from a particular surface will depend on the type of polarisation. For example, a horizontal metal wire will have a much higher HH (Horizontal out and Horizontal return) than VV (Vertical out and Vertical return) backscatter component. Surface scattering generally dominates the return for co-polarised imagery. Volume scatter is a major contributor to signal return of cross-polarised imagery.

Another parameter influencing the strength of the signal return is the dielectric constant (ε). The dielectric constant describes a materials scattering and absorption characteristics. The dielectric constant is a complex number having both a real and imaginary component ($\varepsilon = \varepsilon_r + i\varepsilon_r$). The higher the amplitude of the dielectric constant, the stronger the scattering, resulting in smaller depth of penetration into the surface. The dielectric constant will affect the penetration depth, and therefore the origins of a returned radar signal. The dielectric constant of most naturally occurring objects is generally around 3 to 8, while water is approximately 80. Hence a small change in water content of an object will significantly effect its dielectric constant, and hence its scattering characteristics (Schumann 1996). Reinforced concrete, having a high proportion of metal, will reflect a large percentage of the wave, resulting in a minimal depth of penetration into the surface. A tile roof, however, is considered to have a low real component of the dielectric constant, so the depth of penetration into the surface will be greater. Once the wave penetrates the surface, the imaginary component and material composition determine whether the wave continues through the surface with little loss, or if the energy of the wave rapidly dissipates. If the medium below the surface is inhomogeneous, or a mixture of materials of different dielectric properties, then portions of the transmitted wave maybe scattered by the unhomogeneities, back to the surface again (Ulaby et al. 1981).

Radar backscattering in an urban area very depends on a building's size, shape and density. Larger buildings give a stronger backscatter than small buildings of the same material. The shape will also affect the backscatter. The

more building facets and corner structures facing the radar, the stronger the backscatter. A dense urban area results in a higher signal return compared to a sparse region. For example, central business district consisting of many high-rise structures will have a higher backscatter than a low-density residential area.

One of the most important factors affecting the radar return, and the one which makes urban analysis of radar images the most difficult, is the orientation of the building with respect to the radar look angle. A building's orientation is assumed parallel to the street direction. When a street is running perpendicular to the radar look direction, the return signal will be very strong. The reason for this strong response is due to dihedral corner reflection from the vertical building walls and the horizontal surrounding surface, and facet reflection from the building roof facing towards the radar. The backscatter can be very high when the radar incidence angle is normal to the slope of the building roof, since it acts as a mirror reflector. At other times there is diffuse scattering, depending on the type of roof material, its orientation with respect to the incoming signal, and radar wavelength (Xia and Henderson 1997, Ticehurst 1998).

The backscatter is often related to the size of an object and the wavelength λ, with objects approximately the size of the wavelength or larger appearing bright and objects smaller than the wavelength appearing dark. The higher or brighter the backscatter on the image, the rougher the surface imaged. Flat surfaces that reflect little or no microwave energy back towards the radar will always appear dark in images. Vegetation is usually moderately rough on the scale of most radar wavelength and appears as grey or light grey in a radar image. Surfaces inclined towards the radar will have a stronger backscatter than surfaces, which faces away from the radar, which will tend to appear brighter in a radar image. Some areas not illuminated by the radar, like the back slope of mountains, are in shadow, and will appear dark. When city streets or buildings are lined up in such a way that the incoming radar pulse are able to bounce off the streets and then bounce again off the buildings and directly back towards the radar they appear bright in radar image. These backscatter properties are the ideal backscatter of imaging radar. As previously stated, there are many occurrences of

the artifacts in the image as the result of many parameters. More details can be seen in section 2.2.2.

2.2.2 Foreshortening, Radar Layover and Radar shadow

Geometric distortion usually accompanies radiometric enhancement by slopes. Three cases of geometric distortions which are foreshortening, radar layover and radar shadow, are described in this section.

Active microwave radar measures signal travel time. The time delay between the received radar signal reflected from a point 1 and a point 2 determines the size of the imaged region in the radar image. If radar wave front interacts with the local ground near to parallel, the entire area of this near-parallel interaction is imaged only within this short time delay. These conditions apply, if the local incidence angle is near 90°, i.e. if the mountain slope bends towards the sensor direction. In Figure 2.5, only the projection to the radar beam plane is considered. However, all slopes with other azimuhtal directions but considerable projected slopes in the radar beam direction are affected by this phenomenon.

Foreshortening areas can clearly be identified in SAR images. They occur as bright fringes on the sensor-side of the features ad give SAR images of hilly terrain their typical plastic appearance.

An extreme case of foreshortening is layover in which the top of a feature is nearer to the radar antenna than the bottom of the feature. Subsequently, the top is imaged earlier (nearer to near range) than the bottom, thus inverting the local feature geometry. Due to the geometric compression of the area, the effect is only visible as sharp fringe in hilly areas and is associated to the foreshortening effect. Figure 2.5 shows the geometry of radar layover.

The bright pixels in foreshortening and layover areas, even sometimes with saturated intensities in not well-balanced and calibrated SAR systems, are caused by two effects. First, the entire radar energy of a certain volume angle, intended to image a larger region, is detected by the sensor during a shorter

imaging time. The radar energy is compressed to a few resolution cells only. Second, the incidence angle in these regions is near 90°, which mean maximum, mirror like reflection in most radar reflectivity models. So, more power is reflected in these areas than in others.

The occurrence of shadowed regions is also a very special effect in range directions, unparallelised in optical images. In the shadow area there is no image information by geometric relations, not less or non-reflections or returns due to missing energy. Shadow in radar images occur on slope areas, which are bend away from the look direction. If the slope is steeper than the incidence of the radar beam, the terrain is not seen by the radar as examples can be seen in Figure 2.5.

However, filtering of the interferogram or phase image may partially mitigate this effect. While the layover would probably cause elevation information to be lost, depending on the relative magnitude of the scattering cross-sections of the fore ground, nearside and top nearside of the building. For the STAR-3I system, the total horizontal region of uncertainty is approximately equal to twice the height of the building. The example of radar shadow and radar layover from the data set is shown in Figure2.6.

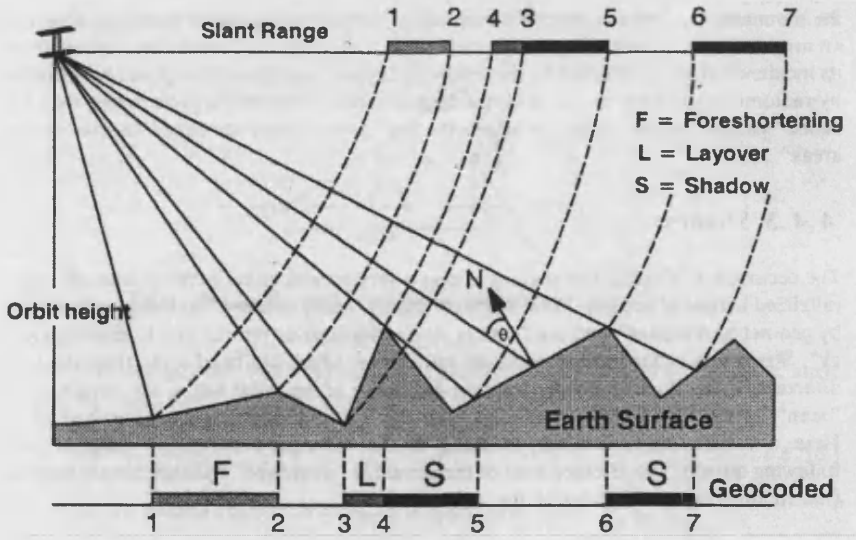

Figure 2.5 Terrain distortions in SAR (Schreier 1993).

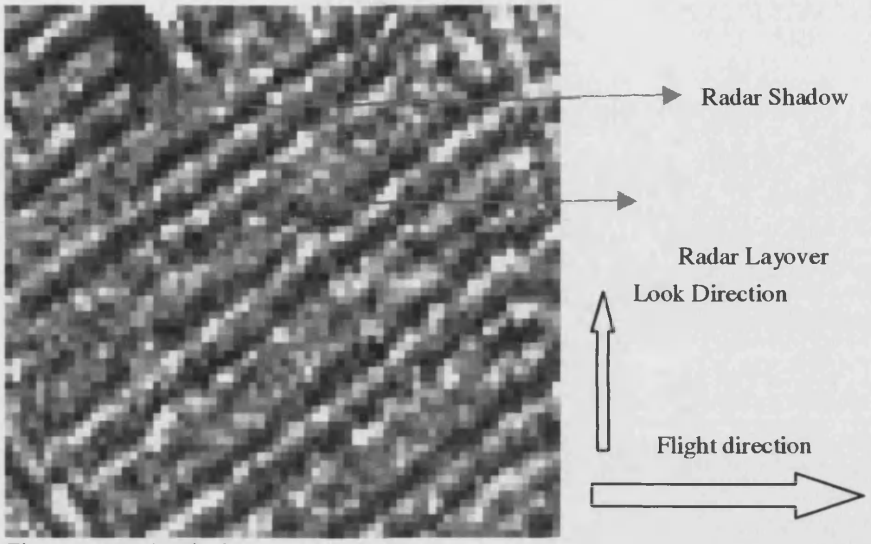

Figure 2.6 Radar shadow and layover.

The radar shadow and radar layover as well as the foreshortening or the effect, which presented in the image due to the geometry of the sensors and the objects on the ground, can be rectified by using another image of the same area from different looking angle. Since the geometry of the image is changed, the effects presented in the image are changed as well. Thus, by combining the information from different images, the true picture of the objects can be mosaiced together.

2.2.3 Coherent and Incoherent Effects.

As stated in section 2.1.1 that reflections from all scatterers combine according to their phase interaction. It would be reasonable to conclude that all scattering, whether from a diffuse or a specular surface, should be described in as coherent. Coherence is the correct physical condition, it is not the implication of terminology frequently encountered. Reflectivity is said to consist of a coherent component and an incoherent component.

Incoherent scattering is used to denote backscatter from a diffuse or electromagnetically rough surface. The term derives from the random phase

imposed on all elemental reflectors due to their randomly distributed position, so that in combination their relative phases are random. Incoherent scattering refers to the ensemble behaviour, in spite of the fact that each constituent is coherent. For most purpose, the term incoherent scattering maybe understood to mean diffuse scattering.

Coherent scattering as used in the literature derives from highly correlated relative phase structure among an emsemble of elemental reflectors. The narrow definition of coherent scattering is used to denote specular backscatter from one or more smooth surfaces. Individual ray's transversing different paths through corner reflection are coherent in this sense. The definition of coherent scattering maybe extended beyond such simple cases. Scattering phase agreement occurs when the ranges to most of the individual scatterers, measured in multiples of the radar wavelength, are approximately the same. The tolerance for phase agreement is about $\lambda/8$, which is the same threshold applied to determine surface smoothness in the Rayleigh criterion. When they are in phase, the individual reflections add constructively, leading to a larger vector sum at the radar than if they had added in random phase, as occurs for diffuse scattering. As is true for all kinds of reflection, the total field sampled by radar is the coherent summation of all contributions. Individual reflections that add in phase imply enhanced brightness in the corresponding radar output. This, therefore, can lead to the misinterpretation for the later processing such as classification or edge detection. Coherent backkscattering can arise from two different geometric arrangements: 1) many scattterers at the same range and 2) scatterers regularly spaced in range.

2.2.4 The specular point

Consider a region of illuminated terrain of size larger than several resolution cells. If the slope of this area is such that the local incident angle approaches zero, then the specula direction is directed back towards the radar. Of course, most surfaces for which the concept of slope is meaningful have a scatterer height distribution that is clustered about the local ground plane. It follows that radar reflections from illuminated areas with small local incident angle are characterised by a large population of individual reflections with correlated phases, which are observed as coherent scattering. This is always the case with altimeters, particularly those intended for use over the ocean, which are designed to be responsive to the specula component of reflection from nadir. The specula point phenomenon occurs frequently with satellite radar viewing mountainous terrain. Mountain imagery is characterised by bright returns from crests and ridges that have extensive facets perpendicular to the radar illumination.

2.2.5 The Cardinal Effect

The second type of coherent scattering occurs for extended features in azimuth that tend to have constant radar range at a tolerance comparable to the radar wavelength. If the scatterer positions are organised such that their average geometric structure is aligned with the phase fronts of the illumination, then the reflections from these scatterers will have correlated phases. This is the defining condition for specular scattering. This phenomenon is known as the cardinal effect. It was noted that reflections from urban areas, often laid out according to the cardinal points of the compass, caused significantly larger returns when the linear features were illuminated at an angle orthogonal to their orientation. This effect is clearly seen in SAR images. As it can be seen in Figure 2.7, the bright pixels are results of the coherent effects, which make these pixels value higher

than they should be. The effect is clearly present in the buildings north of the river parallel to the flight path.

The artifacts presented in the image caused by coherent and incoherent scattering leads to difficulties in image classification since the pixels value of the artifacts are very much higher than the normal pixels of the same conditions. Therefore, those pixels should be not processed with other pixels. This can be done by blocking the processing not to use the pixel at very high pixel value. But it also results in losing some information from the pixels in which it contains a very high level of pixel value by itself not from the effects.

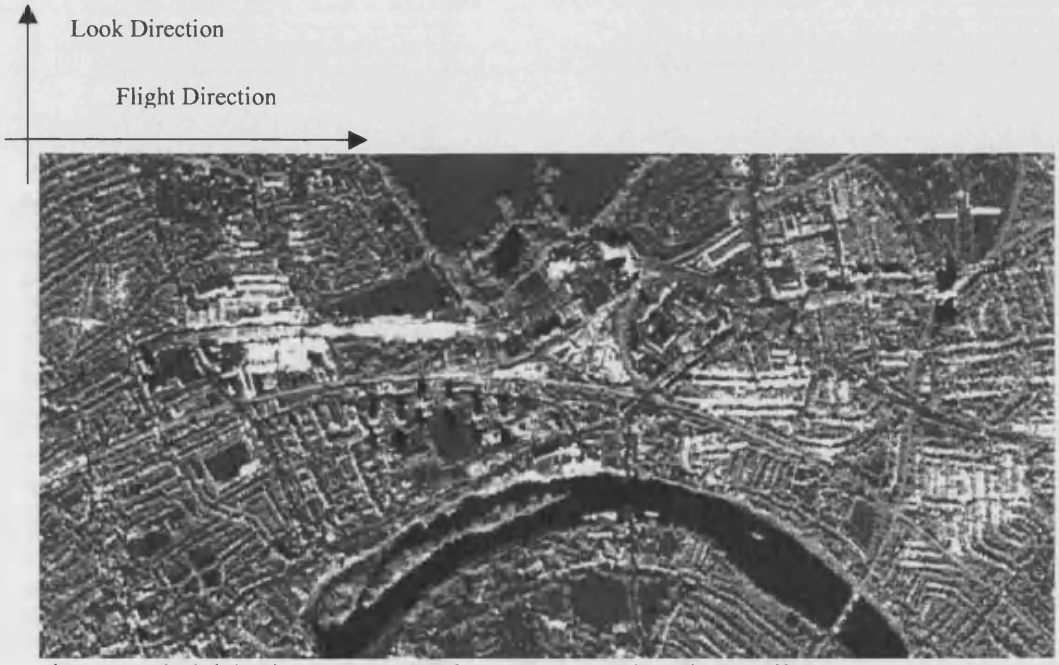

Figure 2.7 The bright pixels are resulted from Coherent and Incoherent effects.

2.2.6 Speckle

Remote sensing radar uses the return signals (echoes) from the terrain to generate an image. The return signal is subjected to random fluctuations in strength that are the result of the interaction of the radar wave or pulse with these rough terrain surfaces. This interference, a result of signals adding in phase and out of phase is known as fading. Fading is responsible for speckle and easily

noticed in high-resolution imagery. The backscatter of each resolution cell or pixel is the combined effect of all the individual objects within the cell, which return or scatter the radar signal. Cells that are adjacent to each other and appear visually very similar may have completely different backscatter at radar wavelengths. This is because the individual objects within the cell are positioned differently giving a different resultant backscatter. The variation in backscatter for otherwise homogenous cell is known as speckle and gives a grainy appearance to radar images.

Speckle sometimes is referred to as the texture of an image, which is the spatial variation in tones or brightness that compose image patterns. However, SAR systems also produce a spatial variance in radiometric output that is referred to as image texture or speckle. This image speckle is a multiplicative random process whose variance and spatial correlation are determined primarily by the SAR system. Speckle influences our ability to estimate image properties and thus is central to information retrieval from individual SAR images. For many purposes the phase inherent in the single-look complex imagery carries no useful information and can be discarded. The information at each pixel is then carried by the *radar cross-section*, RCS, or backscattering coefficient σ^0.

In a SAR image, there is more image speckle than can be seen. Sometimes it is used as a clue in identifying terrain features. Speckle contributes to or detracts from the ability of the interpreter to discern meaningful patterns at all levels of detail. At a coarser scale, speckle pertains to the scene texture in an image and to the detection and identification of feature on the image. For example, urban residential areas forest canopies all exhibit texture that is often unique and thus aid in their identification on radar imagery. Speckle is normally an unwanted and dominating noise that degrades SAR image products, as it is well known And it is also known that speckle carries valuable information about the imaging system itself, and about all digital analysis steps between the original image and any given image product. In the later part of this report, the speckle reduction process will be described as well as the evaluation of speckle

reduction filter for the edge detection and feature classification. More details about speckle modeling and Speckle Reduction can be found in chapter 3.

In fact, there are more effects and artifacts occurring in a SAR image over an urban area but not stated here such as multi-path, which caused by the returned signals that hit more than one features before returning to the sensor, can cause ghosting. Because there is no strong evidence that the effect presents in the image. There are more details on speckle and speckle reduction techniques in Chapter 3.

2.3 Data Model

During the last decade, SAR data modelling has undergone a considerable boom. Several studies have been conducted in order to relate physical features and statistical properties of SAR data and in order to do this some hypothesise and distributions are considered. There are particular properties of SAR images that demand fundamentally different interpretation techniques from optical imagery. In fact, in microwave range, the roughness, the electrical properties, and the shape of the surface influence the returned radiation (Ulaby, 1990) as stated in the previous section. Many sophisticated models have been developed for SAR systems, which need the definition of all the functions needed to reconstruct the image scene from the received signal. Such models, called deterministic, are based on wave propagation equations as a starting point to determine analytical relationships of the backscattering coefficients from the knowledge of the observed scene electromagnetic properties (Ulaby 1990, Tsang et al 1985). Moreover, elaboration of these models imposes various simplifications because of the great number of input parameters needed, which in turn limits their efficiency in various remote sensing applications. In other terms, these models were derived, for describing the SAR signal behaviour, from the geometrical and physical effects, and not for image processing and understanding purposes. Most of the work developed for SAR data modelling consists in deriving the scene properties given the data (Dobson 1995, Ulaby 1990, Van Zyl 1993,Van Zyl 1987, Zebker 1987).

Speckle itself conveys very little information about a scene other than that it contains many randomly positioned scatttering elements. However, in the wooded region it is apparent that there are fluctuations in addition to speckle. Physically, these appear to correspond to strong returns from the crowns of trees with shadows behinds them. If we disregard the deterministic positions of these light and dark fluctuations, we can treat this type of natural clutter as a noise-like texture. Note that texture is a consequence of fluctuations in the Radar Cross Section or RCS; a clutter sample comprised of speckle alone is not considered textured. Texture measures will take the form of spatial average properties describing the depth of fluctuation of the RCS within the local region. These can be single-point statistics, such as the *probability density function* (PDF). More information is contained in two-point properties such as the power spectrum or Auto Correlation Function, ACF.

One of the most important classes of iinformation within an image is contained in its structure. This comprises features such as the boundaries of large areas of texture, for example, fields or woods, as well as discrete objects, such as individual trees, hedges, roads and buildings. The former can be identified readily by exploiting the texture model. However, a simple noise model would be an inappropriate description for an urban area that is made up of discrete objects. The relative positions of objects in man–made clutter are constrained by rules; for example, houses lie along streets, or trees in orchards are arranged in rows, it follows that spatial average properties over a region do not encapsulate the relevant information optimally.

Historically, SAR data models have been largely directed at describing single point statistics through the PDF. Initiallly, therefore, it is important to consider whether typical SAR images are actuallly capable of representation in such simple terms. There are fundamental problems in terms of the nature of the scene being imaged, the physical properties of the imaging process, and finally the analysis of measured data. The scene itsellf, on the coarsest scale is not homogeneous because a map of the area would define boundaries between regions with different properties, fields/woodland compared with land/sea or

forest/mountains at lower resolution. Determinism prevails at the limit of fine resolution where it would be possible, in principle, to represent every scattering element within the scene and derive a unique image under defined conditions. Representation in terms of texture can only apply as an approximation on an intermediate scale when the scatterer spatial distribution appears random.

2.3.1 Empirical data distribution

Early distributional measurements on radar data were carried out at low resolution so that objects, such as trees and houses, were much smaller than a resolution cell. Contributions from RCS fluctuations averaged out so that no spatial variations or correlation effects were visible. The resultant complex field PDF was then Gaussian with Rayleigh amplitude and negative exponential intensity PDFs, respectively.

In order to describe higher resolution data, it was necessary to introduce a second parameter to characterise image contrast. The log normal and Weilbull are two such distributions that have been widely applied. For example, the amplitude of low-resolution sea clutter has been fitted to the Rayleigh distribution, corresponding to pure speckle; while the log normal has been applied at a higher resolution (Trunk 1972, Trunk 1970, Schleher 1975). A wide range of ocean measurements at different resolutions was shown to be consistent with Weibull distribution (Schleher 1975, Fay et al 1977, Sekine et al, 1983). Land clutter was found to be Rayleigh distributed over uniform regions (Valensuela 1972) but log normal over built-up areas (Valensuela 1972, Warden 1970). The Weibull distribution has also been applied extensively to land (Schleher 1975, Booth 1969, Sekine et al 1981), weather (Sekine et al 1979), and sea-ice clutter (Ogawa et al 1987). These distributions can be fitted to either amplitude or intensity data.

The log normal distribution is give by:

$$P(x) = \frac{1}{x\sqrt{2\pi V}} \exp[-\frac{(\ln x - \beta)^2}{2V}] \qquad (2.11)$$

Where x is a generic observable, and β and V are the mean and variance of ln$x$. The mean value and nth normalised moment of this distribution are

$$< x >= \exp[\beta + V/2] \text{ and } x^n \equiv \frac{< x^n >}{< x >^n} = \exp[n)n-1)V/2 \qquad (2.12)$$

The lognormal distribution predicts zero probability of the observable having a value zero. As such it is a very poor representation of the single-look intensity speckle. However, it usually provides a better match to amplitude PDFs, particularly if it is used to represent regions of strong spatial variation such as urban areas. (Valensuela 1972, Warden 1970)

The Weibull distribution is given by:

$$P(x) = \frac{cx^{c-1}}{b^c} \exp[-\frac{x}{b}]^c \qquad (2.13)$$

Where b is a scaling parameter, and c controls the shape. The mean and nth normalised moments of this distribution are

$$< x >= b\Gamma(1+\frac{1}{c}) \text{ and } x^{(n)} = \frac{\Gamma(1+n/c)}{\Gamma^n(1+1/c)} \qquad (2.14)$$

The Weibull distribution is identical to a Rayleigh PDF when c = 2 and to a negative exponential when c = 1. Thus it can describe single-look speckle precisely for either amplitude or intensity. Unfortunately, it cannot represent multi-look speckle exactly. The effect of increasing RCS variations is represented by reducing the value of c.

2.3.2 Product Model

A significant breakthrough in the understanding of radar image properties was the appreciation that many types of clutter derive from two unrelated processes that can be encapsulated in a product model (Ward 1981). In its simple form, this combines an underlying RCS, σ with an uncorrelated multiplicative speckle contribution n; so the observed intensity I, in a SAR image could be expressed as the product $I = \sigma n$. For L-look intensity data, I can be represented as the product of σ with a speckle contribution n, whose PDF is given by:

$$P(n) = \frac{L^L n^{L-1}}{\Gamma(L)} \exp[-Ln] \tag{2.15}$$

This model forms the basis of reconstruction filters and segmentation methods that are designed to derive specific values of σ associated with an observed value I. Note that, in order to exploit this model, it is essential that the speckle and RCS fluctuations have very different spatial scales. Normally the SAR images are resampled so that speckle contributes little correlation between samples. Any RCS fluctuations on a larger spatial scale can then be separated out for further study.

The next component of the product model is to incorporate an RCS model that describes the underlying fluctuations. For a given RCS distribution $P(\sigma)$, the product model asserts that the PDF of the observed intensity is given by:

$$P(I) \equiv \int_0^\infty P(I \mid \sigma) P(\sigma) d\sigma = \frac{L^L I^{L-1}}{\Gamma(L)} \int_0^\infty \frac{d\sigma}{\sigma^L} \exp[-\frac{LI}{\sigma}] P(\sigma) \tag{2.16}$$

The product model represents an important extension to clutter modelling in that it separates two distinct processes. Speckle is purely a consequence of the random distribution of scattering elements, whereas the RCS depends on the physical properties of those elements. Notice that this form of product model is

only appropriate for single images. It is inadequate for multidimensional sources, such as those encountered in polarimetry or interferometry, since it ignores correlations between the images in different dimensions.

2.3.2.1 The RCS Model

Having defined the speckle contribution to the product model, the next state is to discuss the RCS model. Studies of sea clutter by Ward (Ward 1981, Ward 1982) showed that the detected amplitude was Rayleight-distributed in regions of negligible swell, corresponding to pure speckle as expected. Swell has a much larger spatial scale than speckle, allowing the speckle contribution to be averaged out without appreciably degrading the swell component. The underlying swell RCS was usually consistent with a gamma PDF, given by:

$$P(\sigma) = \left(\frac{\nu}{<\sigma>}\right)^{\nu} \frac{\sigma^{\nu-1}}{\Gamma(\nu)} \exp\left[-\frac{\nu\sigma}{<\sigma>}\right] \tag{2.17}$$

Where ν is an order parameter, with moment given by:

$$<\sigma^{n}> = \left(\frac{<\sigma>}{\nu}\right)^{n} \frac{\Gamma(n+\nu)}{\Gamma(\nu)} \tag{2.18}$$

This PDF is completely characterised by two variables: the mean RCS (σ) and the order parameter ν. The square of the contrast, that is, the normalised variance, is a useful quantity to describe such data and is given by var σ /(σ) = 1/ν.

Jakeman and Pusey 1976 proposed a theoretical model that provided important insight into the basis for this empirical form of clutter PDF. The simple speckle model showed that the field within a pixel could be represented as the sum of the contributions from the elementary scatters within the resolution cell. Gaussian speckle then arises from the random interference of many

scatterers and corresponds to the limit as $N \rightarrow \infty$. However, Jakeman and Pusey investigated the effect of assuming that the effective number of scatterers N was itself a random number. If the population N were controlled by random processes of birth, death and migration, the consequent population statistics would be negative binomial (Jakeman 1980). Under these conditions the resultant intensity was shown to be K-distributed (Jakeman and Pusey 1978,1980) rather than the negative exponential form expected from the central limit theorem. This derivation suggests that non-Gaussian clutter statistics can be attributed to the fluctuation in the effective number of scatterers within a resolution cell.

Equivalent information for complex reflectivity could be provided using a Fokker-Planck rate equation to describe the RCS (Jakeman 1980, Oliver and Tough 1986). This can be identified as the continuum analogue of a population operated on by processes of birth, death and migration. The solution to the resulting rate equation yields a gamma-distributed RCS with an order parameter given by the ratio of migration to birth rates and a correlation coefficient at lag X given by (Oliver and Tough 1986)

$$\rho_\sigma(X) = \exp[-\gamma X] \tag{2.19}$$

where γ is the migration rate. While this allows all values of order parameter, it restricts the correlation function to a negative exponential form since it is fundamentally a Markov process. However, it is consistent with the choice of a gamma PDF as a description of the RCS (Oliver 1984, 1985).

The Gamma distribution has the convenient mathematical property that it can be regarded as the resultant of a Gaussian random walk process with the final complex reflectivity at a given position expressed as a vector in 2ν dimensions, that is, $S = (S_1, S_2, \ldots, S_{2\nu})$, representing independent real and imaginary contributions. Note that each of the contribution $S_1, S_2, S_3, \ldots, S_{2\nu}$ represents a one-dimensional Gaussian random walk. The total RCS is then given by $\sigma \equiv |S|^2$, which is equivalent to summing ν independent RCS contributions. For simplicity it is assumed that the correlation properties of each complex reflectivity

component are identical. Any form of valid correlation can be adopted, unlike the solution to Fokker-Planck equation. However, it is only strictly applicable for half-integer values of ν. One consequence of this formalism is that all the higher order correlation properties of S and σ can be derived by exploiting the factorisation properties of Gaussian processes (Oliver 1985, 1986).

Alternatively, these can be derived directly for joint Gaussian processes. For example, the bivariate PDF correlated RCS samples separated by a distance X is given by (Jakeman 1980, Armstrong and Griffiths 1991)

$$P_\sigma(X)\frac{1}{2^{1+\nu}(1-\rho_\sigma(X))\Gamma(\nu)}\left(\frac{\sigma(0)\sigma(X)}{\rho_0(X)}\right)^{(\nu-1)/2}X\exp\left[-\frac{\sigma(0)+\sigma(X)}{2(1-\rho_0(X))}\right] I_{\nu-1}\left[\frac{\sqrt{\sigma(0)\sigma(X)\rho_\sigma(X)}}{1-\rho_\sigma(X)}\right] \tag{2.20}$$

Where $I_n[\cdot]$ is the modified Bessel function of the first kind of order n (Abramowitz, Stegun 1970), and $\rho_\sigma(X)$ is the RCS correlation at lag X defined by

$$\rho_\sigma(X)\equiv\frac{<\sigma(0)\sigma(X)>-<\sigma>^2}{<\sigma^2>-<\sigma>^2} \tag{2.21}$$

Hence, the nth-order normalised two-point moment are given by (Armstrong and Griffiths 1991)

$$\frac{<(\sigma(0)\sigma(X))^n>}{<\sigma>^{2n}}=2^{2n}(1-\rho_\sigma(X))^{\nu+2n}\frac{\Gamma^2(n+\nu)}{\Gamma^2(\nu)}{}_2F_1(n+\nu,n+\nu;\nu;\rho_\sigma(X)) \tag{2.22}$$

Where ${}_2F_1(\cdot)$ is the Gaussian hypergeometric function (Abramowitz 1970). The results for n =1, 2 are identical to expressions derived by exploiting the factorisation properties of the Gaussian random walk (Oliver 1986).

2.3.2.2 The Intensity Model

The combination of the speckle PDF and the gamma RCS PDF is the observed intensity PDF, Oliver 1993, which is given by:

$$P(I)=\int_0^\infty P(I\,|\,\sigma)P(\sigma)d\sigma=\frac{2}{\Gamma(L)\Gamma(v)}\left(\frac{Lv}{<I>}\right)^{(L+v)/2}\times I^{(L+v-2)/2}K_{v-L}\left[2\left(\frac{vLI}{<I>}\right)^{1/2}\right] \quad (2.23)$$

For L-look SAR, where $K_{v-L}[\cdot]$ is the modified Bessel function of order $v - L$. Please note that this tends to the gamma distribution for L-look speckle as $v\rightarrow\infty$. The intensity moments are given by

$$<I^n>=<I>^n\frac{\Gamma(L+n)}{L^n\Gamma(L)}\frac{\Gamma(v+n)}{v^n\Gamma(v)} \quad (2.24)$$

Equation 2.14 can be separated into two, formally similar, parts describing the speckle and cross-section contribution. The normalized variance is given by var I / $[I]^2$ = 1 / L + 1 / v + 1 / Lv, which reduces to var I / $[I]^2$ = 1 + 2 / v for single-look SAR.

The PDF of the amplitude (A = $\sqrt{I}$) is also K-distributed such that

$$P(A)=\int_0^\infty P(A\,|\,\sigma)P(\sigma)d\sigma=\frac{4}{\Gamma(L)\Gamma(v)}\left(\frac{Lv}{<I>}\right)^{(L+v)/2}\times A^{L+v-1}K_{v-L}\left[2A\left(\frac{vl}{<I>}\right)^{1/2}\right] \quad (2.25)$$

With moments given by

$$<A^n>=<I>^{n/2}\frac{\Gamma(L+n/2)}{L^{n/2}\Gamma(L)}\frac{\Gamma(v+n/2)}{v^{n/2}\Gamma(v)} \quad (2.26)$$

Hence, var $A/[A]^2 = L\Gamma^2(L)/\Gamma^2(L+1/2)$ x $v\Gamma^2(v)/\Gamma^2(v+1/2)) - 1$ is the normalized variance, which reduces to $4v\Gamma^2(v)/\pi\,\Gamma^2(v+1/2)) - 1$ for single-look SAR.

These derivations for both intensity and amplitude assume that the RCS fluctuations are on a much greater spatial scale than speckle so that multilooking averages speckle without affecting RCS fluctuations. If the contributions were not separable in this way the result would no longer be K-distributed.

The properties of the K-distributed intensity clutter model arising from a gamma-distributed RCS model can be summarized as follows:

- A gamma-distributed RCS can be derived by solving the appropriate rate equation resulting in arbitrary values of ν but with a correlation coefficient restricted to a negative exponential form.
- The RCS can also be regarded as the resultant of a 2ν dimension Gaussian random walk requiring half integer ν but allowing arbitrary correlations.
- The gamma PDF has the attractive property that it represents a general noise process, of which thermal noise is the special case when $\nu = 1$.
- The gamma distribution is the only form of PDF for the RCS discussed in this chapter that yield a closed-form analytic distribution for the detected intensity, that is, K-distribution.

However, the issue that determines the acceptance of this model is extent to which it is consistent with samples of natural clutter. Previous investigation has shown that K distribution is consistent with a large number of coherent scattering experiments, over wavelengths from optical to sonar, and types of scatterer from atmospheric turbulence to natural radar clutter (Ward 1981, Ward 1976, Jakeman and Pusey 1976, Oliver 1985, Jakeman and Pusey 1975, Oliver 1988). In the radar field the K distribution has been used extensively to represent both sea clutter (Wark 1981,Ward 1982, Jakeman and Pusey 1976, Jakeman and Pusey 1977, Abramowitz 1970, Sekine et al 1980) and land clutter (Oliver 1984, Olvier 1986, Fante 1984, Jao 1984, Oliver 1988, Oliver 1991, Yueh et al 1989, Kreithen 1991). Note that the observed statistics would be modified by any additive input noise in the radar receiver (Watts 1987, Lombardo 1995).

2.3.3 Model Comparison

Having introduced the K, Weibull and log normal PDFs, now the comparison between the PDFs can be formed by considering their mathematical properties and tests done by previous studies (Press et al 1994, Valenzuela 1972, Warden 1970).

The K-distribution provides an excellent fit to the woodland clutter. All other distributions have a negligible probability of being correct. Physically, the exponential would be expected to be incorrect since it cannot describe RCS fluctuations with speckle. The log normal predicts a probability of zero at zero intensity that conflicts with the speckle model, which mean it cannot represent the intensity value of zero. The Weilbull PDF, on the other hand, yields an incorrectly large probability for zero intensity. The gamma distribution matches the low intensities well but predicts probabilities for large intensities that are too high.

It, therefore, might be concluded that only the K-distribution should be retained as a clutter model, with $\nu \rightarrow \infty$ assumed where the statistics appear smoother than speckle fluctuations. This would be premature since, while these results are typical of natural clutter at the study's set of data, many other experimental comparisons have been conducted at differing wavelengths, resolutions and polarisations. The lognormal has been found to be appropriate for urban clutter (Valenzuela 1972, Warden 1970), while the difference between Weilbull and K PDFs is sufficiently small that slight changes in clutter properties make the Weilbull preferable under some circumstances (Schleher 1976, Booth 1969, Sekine et al 1981,1979, Ogawa et al 1987, Kreithen 1991). The final choice of PDF must depend on the observed statistics in the specific clutter sample. However, the product model should be retained because of the physical insight it gives into the speckle process, together with a gamma distribution to describe any RCS fluctuations.

Another reason for not rejecting lognormal and gamma distributions for natural clutter is that they can be useful as approximations to the K-distribution

as sample size becomes small. Thus, in discussing texture and feature classification in later chapters, which should be applied to smallest window size possible, analytical log normal and gamma approximations can be applied with only minor degradation, compared with using K distribution that can only be evaluated numerically. Moreover, since the data used in this research is emphasised on the urban area, the lognormal PDF would be more suitable than K PDF in order to have a precise classification.

2.3.4 Limitation of Data Model

The correlated K-distributed data model is intended to describe extended areas of homogenous clutter textures, which can be regarded as single realisations of stationary noise processes. Thus, it was tested against the homogenous samples. Of course, the model contains no information about the location of the boundaries of particular textures; this could be provided by independent structural information derived, for example, from a map. Image interpretation based on this model uses spatial average properties, measured over some local neighbourhood, to define image properties. While this is appropriate inside extended clutter areas, averaging across boundaries mixes the properties in the overlap region, which is obviously undesirable.

Despite the success of this correlated noise model, it is important to identify its limitations. The first arises from the fact that there are a larger number of individual features in SAR images that cannot be described in term of homogeneous texture at all. Hedges, isolated trees and farm buildings, with associated shadows, are best represented as deterministic structures recording the position and cross section of individual objects within the scene, that is, as in a map. In a military context, isolated objects such as bridges and vehicles clearly belong in the same category. These may requite a totally deterministic solution that models the full physics of the scattering process. For example, deterministic images of dielectric objects, such as houses, can be simulated based on physical optics combined with the Geometrical Theory of Diffraction (Takbasjsh et al

1994a, 1994b). While this represents a solution of the Forward Problem, it is not clear to what extent it is useful in image interpretation. Identifying suitable techniques for extracting information about man-made objects against an extended clutter background represents a combination of textural and deterministic properties.

The second limitation emerges when nominally homogeneous regions are analysed in more detail, particularly as the resolution is increased. Detailed study of the individual textures suggests that, though they appear to be homogenous, they contain more than one component. Upon lifting the PDF to a combination of two k-distributions, described by five parameters instead of two. The additional degree of freedom would be expected to improve the fit. Nevertheless, this improvement seems significant. These textures were actually represented equally well by a two-component log normal mixture. Increasing number of degrees of freedom tends to make the form of PDF less critical. This result establishes that a mixture of processes may be required to describe high-resolution natural SAR clutter where the single-component K distribution model fails.

2.4 Conclusion

The principles of SAR/IfSAR have been described in this chapter. It is important to understand the characteristics of the system in order to maximise the use of the airborne SAR/IfSAR data. The studies have also shown the effects, artefacts, and difficulties as results of applying SAR/IfSAR in urban areas.

The data model of SAR image has introduced. The use of mathematical model to explain how signal and objects on the ground interact to each other has been considered. Empirical data distributions have been described. The distributions were compared against each other in order to find the suitable distribution to describe SAR image. Nevertheless, the data model is not able to precisely describe the SAR image, there are still some limitations in using a data model to estimate the SAR image. Such considerations of the SAR data model leading to object-oriented classification are described in Chapter 5.

Chapter III.

Image Pre-processing and Speckle Reduction

3.1 Introduction

In the previous chapter, the natural phenomenon and also the artefacts of a SAR image have been described. These effects have good and bad influences on the processes of feature extraction and classification. The preprocessing step is a routine step for SAR processing. This is to keep, as much information in the data set as possible while reducing the noise or suppressing the unwanted information. The speckle reduction process is one the most common and the most important preprocessing steps for SAR imagery. From the data model in the previous chapter, this chapter begins with a speckle model, followed by speckle filters and the evaluation of the filter performance.

3.2 Speckle Model

The statistics expected from a distributed scene at a single point of observation is the traditional approach to speckle. The term "fading" is in common use to denote the variation in reflectivity at each observation point. For synthetic aperture radar imagery, however, the spatial properties of speckle are at least as important as the per-pixel properties.

Speckle is often modelled as a multiplicative random noise process, which is statistically independent of the scene, although this relatively simple representation is not always appropriate. When using the multiplicative model, speckle usually is understood to imply an idealised circularly symmetric Gaussian random process. The idealised form of such a Gaussian process is known more formally as fully developed speckle. In many practical situations, speckle is not fully developed, recognition of which may be helpful in quantitative image interpretation.

Multiplicative noise model

It is customary to represent speckle as a random process, which appears as a multiplicative modulation of the scene (power) reflectivity. The multiplicative noise process is statistically independent of the reflectivity random process. The multiplicative model is strictly valid only when the speckle is fully developed, and when there is rather small change in contrast within each neighbourhood being modelled. Aptness of the multiplicative noise model decreases with increasing compromise on these two conditions.

It has been shown that the multiplicative model must be enriched by additional terms when there is a gradient in scene contrast over a distance of several resolution cells or less. Thus, either for image simulation or for image interpretation, speckle analysis is best confined to areas having mean reflectivity that is constant over an area larger than several resolution cells. Indeed, in order to have sufficient data for estimating the sample statistics, many resolution cells are preferable. By definition, speckle analysis requires an area of homogenous distributed scatterers (Tur et al 1982, Madsen 1986).

Fully developed speckle

Speckle is a term that has various levels of meaning in popular usage. It is helpful to identify the case of fully developed speckle, which is the intended but understated meaning in many contexts. Goodman 1986 provides an elegant summary of the issues involved. Fully developed speckle statistics are obtained if and if only:

i) There are a large number of scatterers contributing to the signal at each observation opportunity.

ii) None of the scatterers is so strong that it tends to dominate the total reflected signal

iii) The contributing scatterers are statistically independent of each other, and

iv) The phase of the contributing scatterers must be uniformly distributed over $[0, 2\pi)$.

The first three properties provide a basis for the central limit theorem, from which it follows that the real and the imaginary parts of the complex sum are statistically independent Gaussian random variables. In its strictest form, all scatterers are required to have to same magnitude of reflectivity, although the constraint of ii, is a practical one, and leads to similar results. The fourth property assumes that the real and the imaginary components have equal variances, leading to circular complex Gaussian statistics. This model for fully developed speckle leads to the exponential PDF described in the previous section, and is the conventional assumption implied for most speckle discussions.

Speckle is interesting and valuable both in its fully developed state, and also as it appears when certain of the fundamental conditions are compromised. Some of the compromises are noted here.

If the number of scatterers per resolution cell is not large, then there still will be coherent interference between each contribution, but the statistics stray from the fully developed speckle case. In general, there is no closed form mathematical modelling for the transition from many scatterers to one scatterer. Although the classic lower limit of many is often cited as five, it has been shown that more than 10 scatterers are required to assure convergence of the statistics to the fully developed case (Vachon 1987).

If on average there is only about one scatterer per resolution cell, then it is popularly accepted that the signal doesn't suffer speckle. The situation is subtler, however. When there is an extended area of random scattering, statistical variations in scattering still occur, even for a very small number of scattering elements. Both through analysis and experimental investigation, there is evidence that phase and amplitude modulations of a given isolated scatterer occur for average scatterer densities in the scene as small as one per 10 resolution cells (Jakeman and Pusey 1976, Vachon 1987). Thus, the transition from an isolated coherent reflector to pure speckle spans a wide range of individual scatterer densities.

If the number of scatterers in each resolution cell is random, then the classical mathematical approach gets much more complicated. Of course, for many radar applications, there may also be a large number of contributing scatterers. Experience has shown, when the mean reflectivity is constant across resolution cells, that the observed speckle statistics seem immune to variations in the number of individual contributions (Henderson and Lewis 1998).

3.2.1 Statistical Characterisation of Speckle noise

Speckle is essentially due to the coherence of the radar waves and the roughness of the terrain with respect to the wavelength used. It is the result of constructive and destructive interference between the reflected signals from scatters within one resolution cell. Speckle is not random in the sense that if a target is imaged at two different times from exactly the same point in space and with exactly the same incidence angle, then the same backscatter value is measured. Nevertheless, it is treated as a random variable and considered as multiplicative noise since its local standard deviation depends on the local mean value (Goodman 1976). In dark areas, the speckle standard deviation is small, while in bright areas it is rather large. The multiplicative model states that, under certain condition, the observations with in SAR images are the outcome of the product of two independent random variables, one modelling the terrain backscatter and the other modelling the speckle noise (Goodman 1976). Speckle in a single-look intensity image has an exponential distribution (Laur 1989):

$$P(I) = (1/2\sigma^2) \exp -(I/2\sigma^2) \qquad (3.1)$$

Its mean and standard deviation are the same and equal to $2\sigma^2$ where σ is the average value of the intensity measured by sensors, called average radar reflectivity. Speckle in a single-look amplitude image has a Rayleigh distribution (Laur 1989).

$$P(A) = (A/\sigma^2) \exp -(A^2/2\sigma^2), \text{ for } A \geq 0 \quad (3.2)$$

Its mean and standard deviation are $\sqrt{\pi}/2\sigma$ and $(\sqrt{2}-\pi/2)\sigma$ respectively. Speckle in multi-look intensity image appears by taking the average over k independent samples leading, thus, to a Gamma distribution characterised by:

$$P_K(I) = \frac{k^k}{(2\sigma^2)^k \Gamma(k)} I^{k-1} \exp(-\frac{kI}{2\sigma^2}) \; I,k > 0 \quad (3.3)$$

Where $\Gamma(\cdot)$ is the Gamma function. Its mean and standard deviation are $2\sigma^2$ and $(2\sigma^2)/(k)^{1/2}$, respectively. For multi-look amplitude image, no simple closed-form expression can be found for speckle distribution. However, if the multilook amplitude image is calculated by taking the square root of the multilook intensity image, the multilook amplitude speckle can be approximated with the square root of Gamma distribution. The result is the Chi-square distribution given by Laur 1989:

$$P_k(A) = \frac{2k^k}{(2\sigma^2)^k \Gamma(k)} A^{2k-1} \exp(-\frac{kA^2}{2\sigma^2}) \;\; A,k > 0 \quad (3.4)$$

Its mean and standard deviation are given as follow

$$m_A^k = (\frac{\Gamma(k+0.5)}{\Gamma(k)})\sqrt{\frac{\sigma^2}{k}} \;\; , \;\; \sigma_A^k = ((k - \frac{\Gamma^2(k+0.5)}{\Gamma^2(k)})(\frac{\sigma^2}{k}))^{1/2} \quad (3.5)$$

For an easy computation of these quantities the following first order development of some Gamma function's properties can be used, given in Abramowitz 1972, for small number of k such as in Nicholas et al 1997.

$$\frac{\Gamma(z+a)}{\Gamma(z)}=(z-1)^{a}(1+\frac{a(a+1)}{2(z-1)}+O(\frac{1}{z}))\Rightarrow\frac{\Gamma(k+0.5)}{\Gamma(k)}=\sqrt{k-1}(1+\frac{3}{8(k-1)})+O(\frac{1}{\sqrt{k}})(3.6)$$

Thus, the mean and standard deviation given in Eq3.5 can be approximated as: $(1\text{-}1/(8k)(2)^{1/2}\sigma$ and $1/(2k)^{1/2}\sigma$, respectively.

The presence of speckle renders image interpretation difficult and reduces the performances of classification algorithms. Speckle reduction is a necessary procedure before an automatic and efficient class discrimination can be performed.

3.3 Multilook processing

The simplest approach to de-speckling is to average the intensity over several pixels within a window centred on a specific pixel. This is tantamount to assuming that the RCS is constant over the filter window. If this assumption is incorrect, the method is fundamentally flawed. The joint probability that all N pixels have this mean value is given by:

$$P(\sigma \mid I_1, I_2, ..., I_N) \propto \prod_{j=1}^{N} P(I_j \mid \sigma) = \prod_{j=1}^{N} (\frac{L}{\sigma})^{L} \frac{I_j^{L-1}}{\Gamma(L)} \exp[-\frac{LI_j}{\sigma}] \qquad (3.12)$$

for L-look SAR, where pixels are assumed independent. The MLE for σ is then given by

$$\sigma_{ML} = \bar{I} \qquad (3.13)$$

which is the average intensity over all the pixels in the window, corresponding to multilooking. Note that if this applied to a single pixel the MLE is equal to the intensity of that pixel.

The multilooking despecking method reduces the SD of the speckle variations in regions of relatively constant RCS by a factor $\sqrt{N}$, it also degrades

resolution by the same factor resulting in the blurring of small objects. Only if features of interest within the scene occur on a large enough scale can multilook images be effective. An adaptive approach that matches the size of a window to the scale of objects of interest would provide optimum despeckling at the required resolution. Where fluctuations were consistent with a constant RCS the window size can be increased to improve depspeckling as far as possible.

3.4 Speckle Reduction

Speckle causes many difficulties in SAR processing. One of the major difficulties when classifying synthetic aperture radar images is the existence of speckle. By influencing on the pixel distribution of SAR images, speckle could change shape and type of data distribution, therefore, leads to misclassification. Edge detection is also affected by the presence of speckle. Since an edge detection algorithm searches for edges in a SAR image at pixel level, the "speckled pixels" could leads to mis-detected results.

Even though, information carried in speckle may be useful for advanced analysis. It is necessary to eliminate speckle in order to get accurate results from SAR classification process. In the next section, four speckle reduction techniques are described as well as the analysis of their results and performances.

Conventional linear filtering is constrained by the principle of conservation of confusing: what is gained in image variance is lost in image resolution. Adaptive speckle reduction filters promise to do better, and will be reviewed in the later part of this thesis.

Before applying a speckle reduction filter, the objective should be clearly identified. If a quantitative image analysis is to follow the application of speckle reduction, then there are implicit requirements on the radiometric transformations involved. For example, if calibration is anticipated using point targets as references, then speckle- filtered images must retain relative gain levels of mean reflectivity of a homogeneous class. It has not yet been

demonstrated that any adaptive speckle reduction filter is able to meet these quantitative radiometric requirements (Henderson and Lewis 1998).

On the other hand, if the objective is simply to derive an image that "looks better", then less stringent criteria maybe applied. It would seem essential, however, to compare the performance of various speckle reduction schemes based on a set of objective performance indices in which some famous techniques will be tested against some important criteria in the later part of this chapter.

Qualification of speckle reduction filters should be based on an extensive analysis of performance against actual SAR data, and not on simulated data. Most SAR simulation packages fall far short of correctly representing point, edge and contrast gradients in the scene, and for situations in which there may be only a few scatterers per resolution cell. None of these situations adequately support the circular Gaussian scattering model on which SAR image simulations depend, yet these include scene elements that are important in applications. The development and application of adaptive speckle reduction filters continue to be active topics in SAR image analysis (Henderson and Lewis 1998).

3.5 Speckle Reduction Techniques

In this part of the chapter, 4 famous speckle reduction techniques are introduced. They each have different approaches for reducing speckle in SAR imagery. These will be described individually later in this part.

3.5.1 Lee-Sigma Filter

- Lee Filter

The Lee filter (Lee 1981) makes use of the statistical distribution of the pixel values within each moving window in order to establish the central pixel value. It is based on the Minimum Mean Square Error (MMSE) criterion and performs a linear combination of the observed intensity, I, and the local average

intensity value, $\hat{I}$ within a fixed window (Lopes et al. 1993). Lopes et al. 1993 have shown that this filter may be formulated as

$$\hat{R}(t) = I(t)W(t) + \hat{I}(t)(1 - w(t)) \tag{3.7}$$

where $W(t) = 1 - (C_u^2 / C_I^t(t)), C_u = \sigma_u / \overline{u}$ is the coefficient of variation of the speckle, and $C_I(t) = \sigma_I(t) / \overline{I(t)}$ is the coefficient of variation of the image.

- Lee-sigma filter

The Lee-sigma filter was proposed by Lee 1983 as a simpler alternative to Lee filter, although it is still based upon the same multiplicative speckle noise model. Within a normally distributed random sample of points, 95.5% fall between two standard deviations either side of the mean. It is reasonable to assume therefore that values outside this range are likely to be part of a different distribution (Shaw and Wheeler 1994). The Lee-sigma filter averages only those pixels in the filter window which lie within two standard deviations of the central pixel. Those pixels which have a value not belonging to the same distribution as the centre pixel are excluded, thus preserving edges and textural variations.

3.5.2 Frost Filter

The frost filter differs from the Lee and Lee-sigma filters in that the scene reflectivity is estimated by convolving the observed image with the impulse response of the SAR system. The frost filter (Frost et al. 1983) is given by the following adaptive impulse response function:

$$m(t) = K_2 \exp[-KC_I^2(t_0) \mid t \mid] \tag{3.8}$$

where K is the filter parameter, K_2 is a normalizing constant, and $C_I(t_0)$ is computed over a uniform moving window centred at t_0.

3.5.3 Gamma-MAP Filter

The Maximum a Posteriori, MAP, approach to speckle reduction was initially proposed by Kuan et al 1987. To carry out this filter, the a priori knowledge of the point distribution function of the scene is required. In the original formulation, the image reflectivity was assumed to be Guassian distributed. However, previous works (Jakeman and Pusey 1976, Jao 1984, Oliver 1986, 1988) has shown this to be invalid as it implicitly assumes a negative reflectivity. Vegetated areas have been shown to be more accurately modelled using a Gamma distributed cross-section. Therefore, Lopes et al 1990 modified the Kuan et al 1987 MAP filter by assuming a Gamma distributed scene.

The Maximum A Posteriori (MAP) filter attempts to estimate the original pixel DN, which is assumed to lie between the local average and the degraded (actual) pixel DN. MAP logic maximizes the *a posteriori* probability density function with response to the original image. Many speckle filters (e.g. Lee-sigma, Frost) assume a Gaussian distribution for the speckle noise. But some works have been shown that speckle is more properly modeled as having a Gamma distribution cross-section. This algorithm incorporates this assumption. The exact formula used is the cubic equation:

$$\hat{I}^3 - I\hat{I}^2 + \sigma(\hat{I} - DN) = 0 \qquad (3.9)$$

Where:

$\hat{I}$ = sought value

I = local mean

DN = input value

σ = original image variance

3.5.4 Local Region Filter

The local region filter initially separates a moving window into eight regions (N, E, W, S, NE, SE, SW, NW) based on angular position in relation to the central, target pixel. Within each region, the variance of the image intensities is calculated. A comparison is then made between the variance values of each region. The pixel of interest is then replaced by the mean of all pixel values within the region with the lowest variance, representing the most uniform area.

This algorithm is based upon the assumption that pixels within the region with the lowest variance are minimally affected by speckle and yet are similar to the pixel of interest (Capstick and Harris 2000).

3.6 Speckle Reduction Techniques Comparison

A number of filtering algorithms dealing with multiplicative noise have been proposed and widely used in the SAR image processing. Some notable ones include Lee's filter, Frost's Filter, and the Gamma-MAP filter as stated in the former part of this chapter. Quantitative evaluation of a filter includes several criteria such as equivalent number looks, mean bias, edge preservation and texture preservation. Among these the most important are (Dong et al 2000):

- Preservation of the global mean
- Reduction of the local standard deviation
- Preservation of edges
- Texture preservation (restoration)

Existing speckle filtering algorithms can effectively reduce the speckle level. These algorithms however also, more or less, smear edges and blur images. Adaptive filters take account of a speckle distribution model, compute local statistics in moving window and assign a pixel's values accordingly, often leading to better results compared to non-adaptive filters. However, smoothing uniform areas and at the same time preserving and enhancing edges is difficult to

accomplish, because the former requires abandonment of high frequency components while the latter needs the preservation of high frequency components as much as possible. One method to minimise the deficiency of smearing edges, for instance, is to use edge-directed windows, rather than the traditional square windows.

There are 4 speckle reduction filters, which have been tested in this project, which are Lee-sigma filter, Frost filter, Gamma-MAP filter and Local Region filter. All of the filters had been tested on intensity images by applying the filter in 3 different test-sites: building area, green area and the whole image. This is to assess the performance of the filters for the edge detection purpose as for it leads to the main purpose, feature extraction for topographic mapping. All of the four filters are adaptive filters in which the processing depends on the local properties of the pixels unlike the simple filters that apply the same algorithm to all pixels. Most of the filters tend to be based on local statistics, which are normally defined as the mean and variance of pixels in the moving window. If the variance in the moving window or local variance is high, then the edge or feature can be presented in the window and vice versa.

To evaluate the performance of the proposed filtering algorithm, we have to follow the criteria for a speckle filter. As indicated above, the most important ones include mean preservation, reduction of standard deviation, edge preservation and texture preservation (restoration).

3.6.1 Mean Preservation & Reduction of Standard Deviation

In the SAR imagery, it is assumed that the features or objects contained in the image, when displayed in the histogram analysis, are the data situated around the mean. On the other hand, the noise or speckle is outside the value of 2SD (Standard Deviation $= \sqrt{\frac{Variance}{Mean}}$ = Coefficient of Variance = σ), which affects on the higher the standard deviation of the image. A good filter should preserve the mean of the image and reduce the standard deviation. The root of the reason

is to keep the information from the image as much as possible while reducing the speckle as well. Thus the speckle reduction should reduce the local SD but not the global SD. In order to assess the performance of the filters, three test areas were set. The first area is the whole intensity image or mixed texture area. The second one is the building or non-uniform area and the third is the ground area or uniform area. Figure 3.1a) shows the whole area of the test image, Figure 3.2a) shows the building or non-uniform area and Figure 3.3a) shows the ground or uniform area.

The statistical data of the filtering results were compared to the original statistic as shown in the Table3.1 below:

		Mean	SD
The Whole Image	Original image	50.839	40.856
	Frost	50.605	40.605
	Gamma MAP	49.285	31.925
	Lee-Sigma	46.573	31.717
	Local Region	48.139	36.11
Non-Homogenous Area	Original image	51.887	31.304
(Building Area)	Frost	51.636	30.659
	Gamma MAP	50.595	21.144
	Lee-Sigma	47.02	22.069
	Local Region	48.717	25.911
Homogenous Area	Original image	23.535	5.917
(Ground Area)	Frost	23.515	5.249
	Gamma MAP	23.063	5.161
	Lee-Sigma	23.89	3.588
	Local Region	23.833	3.939

Table 3.1 Mean and SD of the filtered Images.

Figure3.1 shows the original and filtered images of the whole test area. Figure 3.2 shows the original and filtered images of building or non-uniform area and Figure 3.3 shows the original and filtered images of ground or uniform area.

From Table3.1, it can be seen that in the whole image or mixed texture area, the Frost filter performs very well in preservation of the mean but provides the lowest performance in reducing the standard deviation, not only in the first test image but also in the other two test images. In contrast, the Lee-Sigma and Local region filters are able to provide a good level of standard deviation reduction but the results of both filters are very poor in keeping the mean. The Gamma-MAP filter is likely to be the best filter in this test. It performs very well in both mean preservation and reduction of standard deviation conditions even though the performance over the uniform area is not so well. The overall performance of the Gamma-MAP filter is then better than the others since the data set is mixed residential area with some small ground area.

3.6.2 Preservation of Edge

After the speckle reduction filters were applied to the image for the first two tests, the filtered images then sent to the process of preservation of edge test. The assessment of edge preservation is to accuracy and completion of edges contained in the filtered images. In this project, the Prewitt, 3*3, edge detection kernel is used in order to detect edges in the direction of Northwest only since the buildings in the test image mostly line-up in the direction. The edge images of the filtered image then were produced. The edge images are shown in the Figure3.2. The reference used in this test is the Ordnance Survey Landline Map 1998. By comparing the landline map over the edge images, the quantitative comparison between the detected edges and the edges in the references can be seen. To qualitative evaluation the edge images, the length of detected edges are calculated as well as the length of edges in the reference as it can be seen in Figure 3.4. This is to assess the quality of edge preservation of the speckle filter and the residual of the visible noise left on the images.

Image Type	Possible Detected Edges (m)
Reference (OS Landline)	67512
Gamma-Map Edge	78000
Frost Edge	82287
Local Region Edge	82112
Lee-Sigma Edge	79212

Table 3.2. Length of the possible detected edges from filtered images

Figure 3.1 a) The original image of the whole test area.

Figure 3.1 b) Gamma-MAP filtered image of the whole test area

Figure 3.1 c) Lee-Sigma filtered image of the whole test area.

Figure 3.1 d) Frost filtered image of the whole test area.

Figure 3.1 e) Local Region filtered image of the whole test area.

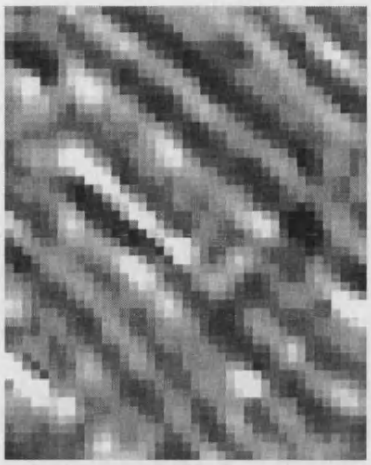

Figure 3.2 a) The original image of building or non-uniform area.

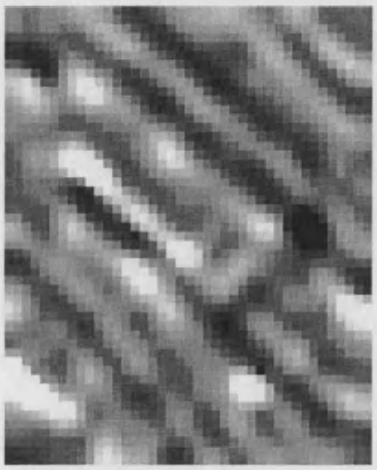

Figure 3.2 b) Gamma-MAP filtered image of building or non-uniform area.

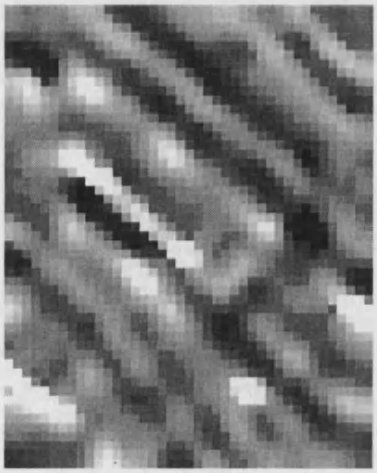

Figure 3.2 c) Lee-Sigma filtered image of building or non-uniform area.

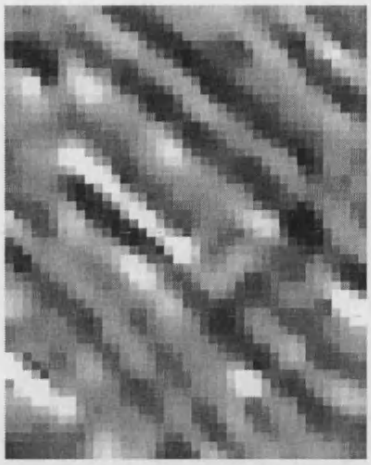

Figure 3.2 d) Frost filtered image of building or non-uniform area.

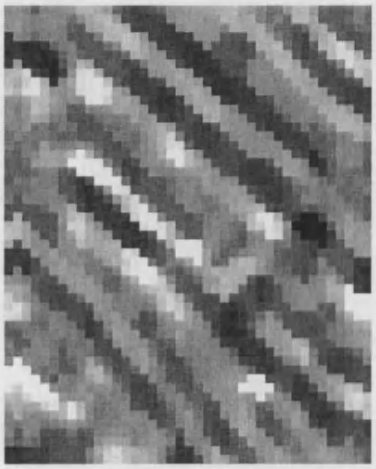

Figure 3.2 e) Local Region filtered image of building or non-uniform area.

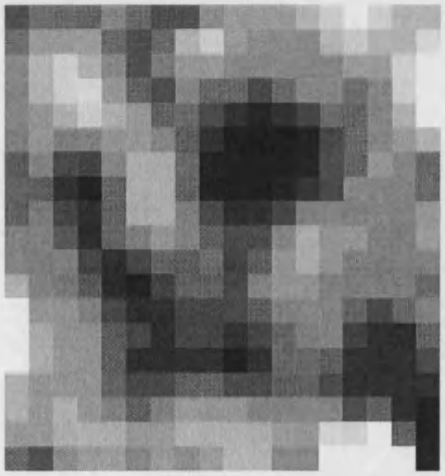

Figure 3.3 a) The original image of ground or uniform area

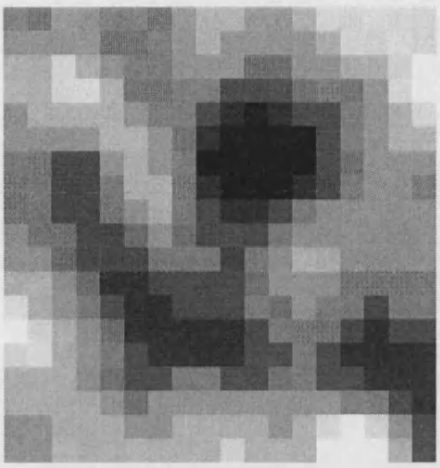

Figure 3.3 b) Gamma-MAP filtered image of ground or uniform area.

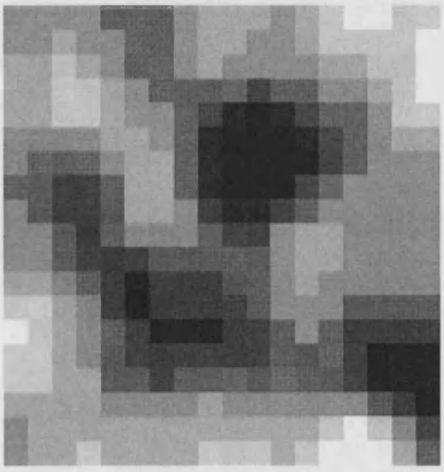

Figure 3.3 c) Lee-Sigma filtered image of ground or uniform area.

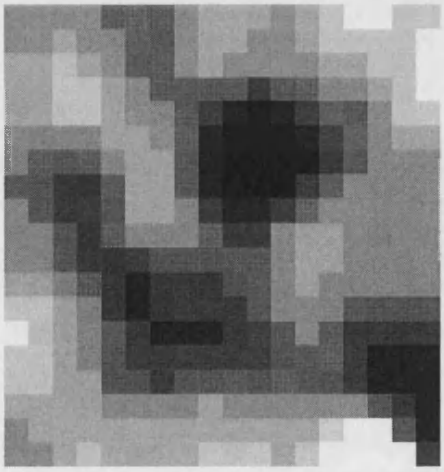

Figure 3.3 d) Frost filtered image of ground or uniform area.

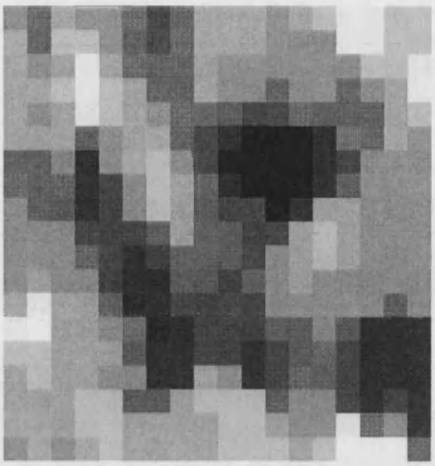

Figure 3.3 e) Local Region filtered image of ground or uniform area.

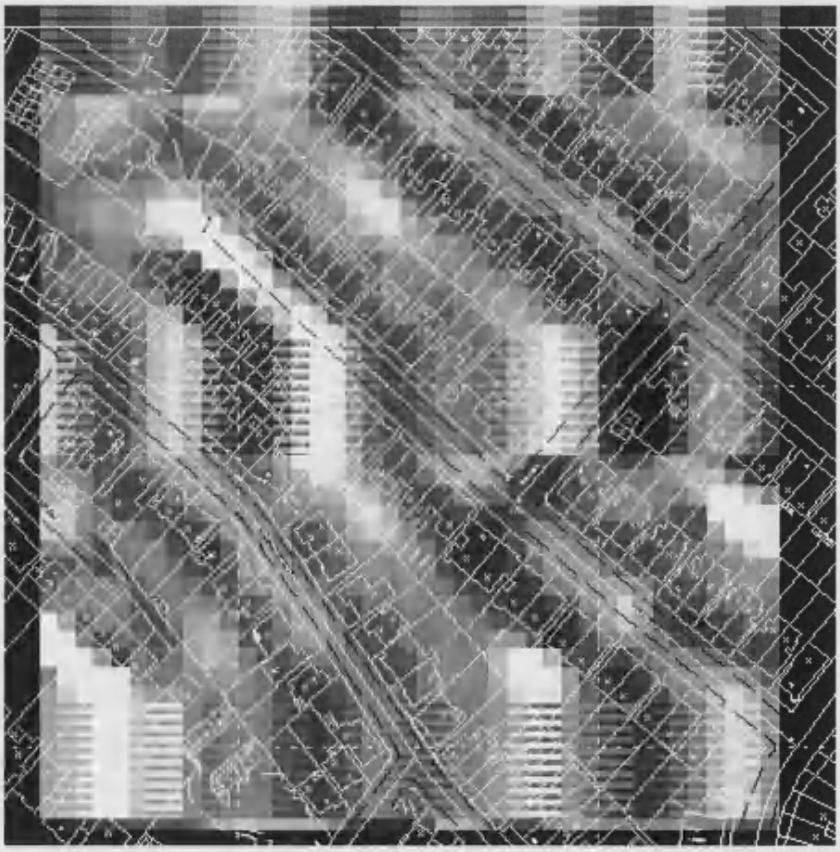

Figure 3.4. The comparison between the Landline map and the filtered image.

From Figure 3.2, all of the filters perform very well in term of preservation of edge. The possible detected edges are all preserved and detected by the filters. But there are some unidentified edges presented in the images. Thus, the areas of edges in the Table 3.2, are higher than the reference. The nearest result compare to the reference edges in OS landline map is from the Gamma-MAP filter. But this is on an assumption that there is no change between the acquiring times of the image and OS landline map. Although providing the best result from all of the tested filters, there are still some noises or unidentified edges presented in the Gamma-MAP result edge image. Even the speckle reduction filters do the speckle suppression but some noise remains after the process of reduction.

3.6.3 Texture Preservation (Restoration)

Texture preservation is another criterion when evaluating a speckle filter, as texture is important information presented in an image. The most widely used textural measures are considered as estimation of the statistics of the various histograms. In particular, four 1^{st} order textural measures based on the histogram (density distribution) and four 2^{nd} order textural measures based on the co-occurrence matrix are selected and used to evaluate filters in terms of texture preservation.

It has been found that apart from the mean preservation, none of the existing filters is able to maintain other textural measures unchanged, as image data are changed by filters. In fact, texture in SAR images can be considered as consisting of two components: intrinsic texture of the scene backscatter and texture due to speckle. Speckle filtering algorithms should aim at reducing the speckle texture and preserving the intrinsic texture. Obviously, the texture of an image with speckle and the texture of the same image without (or with less) speckle are different. The appropriate term for evaluating filters, therefore, should be referred to texture restoration (preserving the intrinsic texture and removing speckle texture). Two algorithms for the texture preservation were

used, the first one is variance and the later one is MED (Mean Euclidean Distance) where;

Mean Euclidean Distance = (3.10)

$$\frac{\sum[\sum_{\lambda}(x_{c\lambda}-x_{ij\lambda})^2]^{1/2}}{n-1}$$

In which:

$x_{ij\lambda}$ = DN value for spectral λ band and pixel (i,j) of multispectral image

$x_{c\lambda}$ = DN value for spectral band λ of a window's center pixel

n = number of pixels in a window

$$\frac{\sum(x_{ij}-M)^2}{n-1}$$

Variance = (3.11)

In which:

X_{ij} = DN value of pixel (i,j)

N = number of pixels in a window

M = mean of the moving window

	Variance Value	Mean Euclidean Distance
Original image	19.673	19.588
Frost filtered image	18.457	18.016
Gamma-MAP filtered image	10.988	10.124
Lee-Sigma filtered image	12.151	12.151
Local-Region filtered image	15.336	14.485

Table 3.3 Texture analysis results.

The algorithms were both assigned on the whole data set. From Table3.3, it can be clearly seen that all of the filters are not able to maintain the texture value of the image as stated before. But from the statistic in the table, it might be said that the Frost filter provides the best result compare to the other four. From the result of Table3.1, the Frost filtered image is very similar to the original image which mean that the pixels value are just slightly changed from the original, thus when calculate the Variance and Mean Euclidean Distance is calculated, the results are so similar.

All of these studies are to draw attention to the point that the speckle suppression method is important in SAR or radar imagery. And it has an influence on the edge detection. Moreover, speckle reduction is important for the later part of SAR image classification. This project will not go deeper in comparing the speckle filter or investigate further in speckle reduction since the main objective is to do the feature extraction and classification.

3.7 Information in speckle

Speckle carries information that maybe used to advantage by the analyst. This sub-section outlines some techniques that have proven to be useful (Handerson and Lewis 1998).

3.7.1 Histogram analysis

For an equivalent number of looks, and for an area of a SAR image with constant mean reflectivity, the shape of the histogram should hold no surprise. A SAR histogram is a plot of the number of occurrences of radar brightness values plotted as a function of digital number (DN). For a given number of equivalent looks, the general pattern and the mean and standard deviation of the histogram should agree with the corresponding probability function.

Consider the example for Figure 3.5, in which the horizontal axis is in terms of the digital numbers of image brightness (amplitude), and the vertical expresses the number of occurrence events of each DN. This histogram is characteristic of one batch of SAR data from Almaz, available commercially. In this case, the general trend is satisfactory, but there are anomalies in the smoothness of the data. With well over 1000 points plotted, the data should be better behaved. As it happens, there are spikes in histogram that regularly occur with DN. This is not a natural distribution of reflectivity brightness. Rather, this type of pattern is indicative of improper data manipulation such as bit truncation, or nearest neighbour interpolation. If a histogram such as this is encountered, do not trust the data for further quantitative analysis until the cause is determined, and its consequences estimated.

Consider another example, Figure 3.6 illustrates a more complicated histogram. Analysis of the complete histogram would show a variance that is larger than expected. On closer examination, however, if the histogram were interpreted as two over-lapping distributions, then the data would make more sense. Each histogram individually, has appropriate mean and variance relationships. If it is established independently that indeed three or two classes of reflectivity contributing to the histogram, then such template matching maybe used to assist in image analysis.

For any given data set, it is helpful to search for areas that appear to have uniform average reflectivity. For each such area, the histogram should be consistent with predicted behaviour.

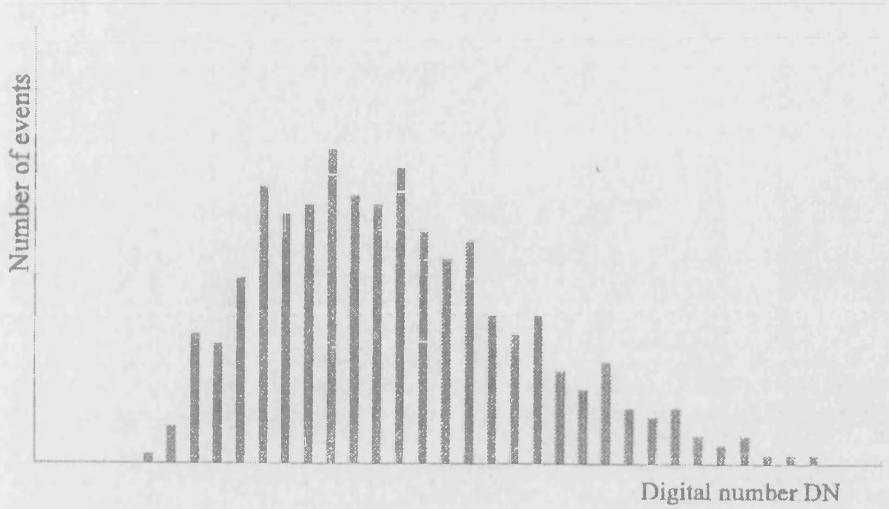

Figure 3.5 Typical histogram after nearest neighbour resampling or bit reduction, showing anomalous frequency of occurrence for uniformly spaced digital numbers (Handerson and Lewis 1998).

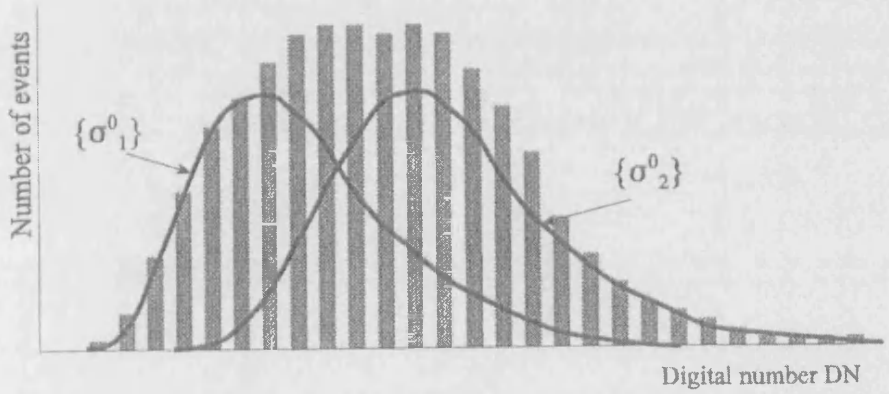

Figure 3.6 Typical histogram for a scene having two regions of different mean reflectivity (Handerson and Lewis 1998).

3.7.2 Response function estimation

If an area has a reasonable single mode histogram, then further analysis is indicated. From the corresponding image data, the two-dimensional spatial auto-correlation function may be plotted. This provides an estimate of the impulse response of the system. Likewise, under the same circumstances, the image spectrum may be plotted, which is an image of the spectral pass band of the

radar/processor combination. Of course, if there is a trustworthy isolated point scatterer in the same neighbourhood of the scene, then its response also should be plotted, and compared to the estimate derived from the speckle auto-correlation function.

What if there is scene texture in the area of interest? The system spectral response may still be estimated from spectral analysis of image data created using an intentionally incorrect focus for the processor (Vachon and Raney 1988). This is a consequence of the principles discussed above. Scene texture in the image is suppressed with mis-focus, whereas speckle texture remains the same. Of course, the trick works only if one has access to the original SAR data. An example of this method is shown in Figure 3.7. In this figure, three sets of spectra are shown, with progressively poorer focus from top to bottom. (The upper two plots have been offset vertically for clarity.) The correctly focused spectrum is the upper one, showing the contribution of the wave contrast pattern in the image. The speckle spectrum is essentially the same for all three-focus settings. In each case, the solid line is the Gaussian nest fit to curve to the data. The zero frequency value, proportional to the average reflectivity in the scene patch, has been suppressed.

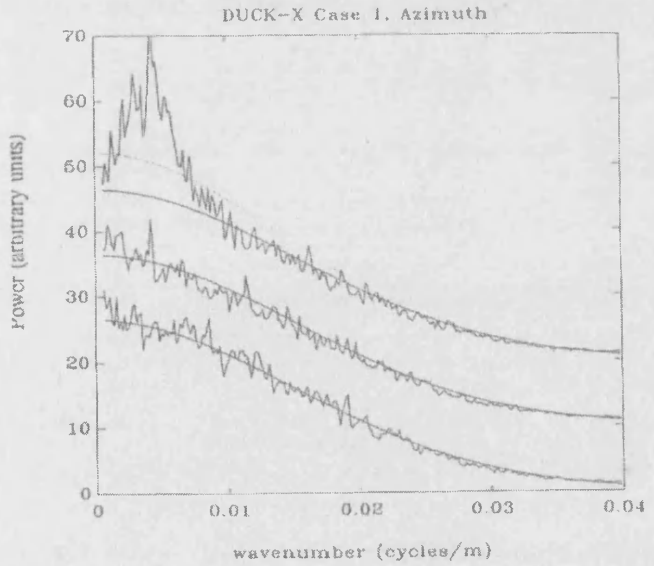

Figure 3.7 Spectral distribution of the same SAR image, for correct focus (upper trace), and progressively increasing mis-focus. The plots have been offset vertically for clarity. (P Vachon, CCRS)

3.7.3 Scene texture enhancement

The speckle spectrum usually dominates the image spectrum, as illustrated by the previous example. This is undesirable for applications in which spectral analysis of a SAR image should lead to information on scene texture. For example, in oceanographic wave analysis, the wave patterns are of interest. The relative contrast of wave signatures in imagery may be increased markedly by removing the system spectrum (Beal et al., 1983), which requires knowledge of the speckle spectrum at the image coordinates of interest. One means of achieving image spectral compensation, and hence relative enhancement of the scene texture, is to divide the image spectrum by the speckle spectrum, and to subtract the resulting constant component from the ratioed spectra.

Such spectra compensation may be realised either in one or in both dimensions. More sophisticated methods have been used, such as template matching, and subtraction of the estimated spectrum (Goldfinger, 1982).

The technique is used routinely in wave analysis of oceanographic SAR data. It should be generalisable to any application, such as forestry, for which a scene texture discriminator is of interest, and of which the scene texture component is expected to have a magnitude larger than the spectral speckle noise.

3.7.4 Scene coherence estimation

Unlike scintillation caused by atmospheric refraction, which constantly changing, speckle, in principle, is unchanging. Consider a scene in which the reflection arises from many individual scatterers that are constant over time. If this scene is viewed through the same geometry on two different opportunities, then the same speckle pattern should be observed. Statistical stability between two observations of a scene leads to a unity mutual coherence function, which is one requirement for successful interferometry (Henderson and Lewis 1998).

The implication is that a departure from mutual coherence in the speckle field resulting from two supposedly identical observations is itself a quantitative measurement of potential value. Less than unity mutual coherence indicates detailed changes in the scattering surfaces on the order of a fraction of the illuminating wavelength. The resulting coherence map may be used to separate different classes of vegetation, wet vegetation from dry, or ice from water, under appropriate observational circumstances in each case.

3.8 Discussion

In this chapter, the 4 speckle reduction techniques have been investigated by using the important 4 criteria as guideline. All the filters were found to be capable of reducing speckle in different manners, which provide different results. From the studies in the past, iterative speckle reduction and pre-filtering processes are proved to be able to give a better rate of reduced speckle in the image. Each speckle technique has its own strength and weakness points. It is necessary to choose the suitable speckle reduction technique depending on objectives of project, data set, etc.

In conclusion speckle is the second order variation of the radiometric brightness of a radar image caused by the mutual coherence of the signals used to build the image. Unlike the case of most incoherent sensors, for SAR the magnitude of speckle is significant. Speckle is both friend and foe. At first encounter it is troublesome, particularly when interpreted only in terms of its radiometric statistics per pixel. If quantitatively interpreted, however, speckle yields information of value both for system characterisation and, in certain cases, for image analysis.

During the process of digital SAR image analysis, it is a good practice to verify speckle statistics at each stage, using areas that seem to have constant mean reflectivity. The original image file should be well behaved when subjected to speckle analysis. This means that the local histogram and equivalent number of looks should be consistent with theoretical expectations. The two-dimensional

autocorrelation function should have a corresponding mean-squared-to-variance ratio, and should have widths consistent with range and azimuth resolutions.

All operations on the image file should lead to predictable transformations of the speckle statistics. In particular, neither radiometric re-scaling nor spatial re-scaling should change the relative speckle level. A spatial averaging operation, no matter how implemented, should lead to a predictable and verified increase in the mean-squared-to-variance ratio.

Chapter IV
Image Feature Extraction

4.1 Introduction

This chapter describes the system developed for feature extraction for SAR/IfSAR in urban areas. It describes the background techniques and how to apply it for feature extraction in SAR image. It begins with a guideline to the whole process, which provide a clear view of how the SAR and IfSAR data are analysed. The processes start with generation of bald an earth DEM. The constrained gradient edge detection is followed. And the chapter ends with the process of region growing from edge detection.

4.2 Processing Procedures

SAR/IfSAR is a system capable of providing an intensity image and a DEM. The approach is to demonstrate the capabilities of SAR/IfSAR data for feature extraction in an urban area.

Since the elevation information or DEM obtained from IfSAR is a so-called Digital Surface Model, DSM, which contains not only terrain surface but also buildings and other objects, the height of the objects on the DEM is the height of the object plus the height of the terrain. In order to get the real height of the object, the terrain height or Digital Terrain Models, DTM or Bald earth DEM has to be subtracted from the DSM. The result is a DEM where the height is the height of features, which can be called a feature surface. The feature surface then will be later used for region growing from edge detection technique to get a more accurate shape of the feature. The technique for generation of a bald earth DEM will be discussed in a later part of this chapter.

The whole process shows capabilities of SAR/IfSAR for mapping in urban areas without any additional information. Even though Lidar is capable of provide a better DEM, but in discrimination between buildings and tree can be difficult. Due to restriction to surface geometry, number of object types, which

can be discriminated with a Lidar DSM is very limited (Haala 1999). Spectral information is required for classification process. This requires data fusion and also image co-registrations between Lidar DSM and spectral images. SAR/IfSAR, on the other hand, doesn't need any data fusion or image registration since both DSM and spectral image (intensity image) are originally from the same sensor.

Firstly, The SAR intensity image, after despeckling, is processed to obtain the edges of features. The techniques used for edge detection is adapted from Canny edge detector (Canny 1986). By using constrained gradient-based edge detector and modified non-maximal, the process is more suited to SAR data. Not only edges are the result from the edge detection technique, but also corner points of those edges. These corner points are used as the seed points for the later part of region growing process. The process itself performs a region growing by analysis of the mathematical parameters for topographic structure as the main criteria. The region growing result comes in the form of polygons representing features, which are classified by feature based classification technique along with texture analysis algorithm. The classification and texture analysis are described in chapter V of this thesis. The whole process procedure is shown in Figure4.1.

In this research, IfSAR DEM provides information for generating normalised DEM and also for feature extraction. SAR intensity image provides information for feature classification and also boundary information for feature extraction.

The edge detection algorithm is adapted from Canny edge detection technique, which is a multi-step edge detection algorithm. Some changes have been made from the original Canny technique in order to make the edge detection more suitable for the SAR image as described in section 4.3 below.

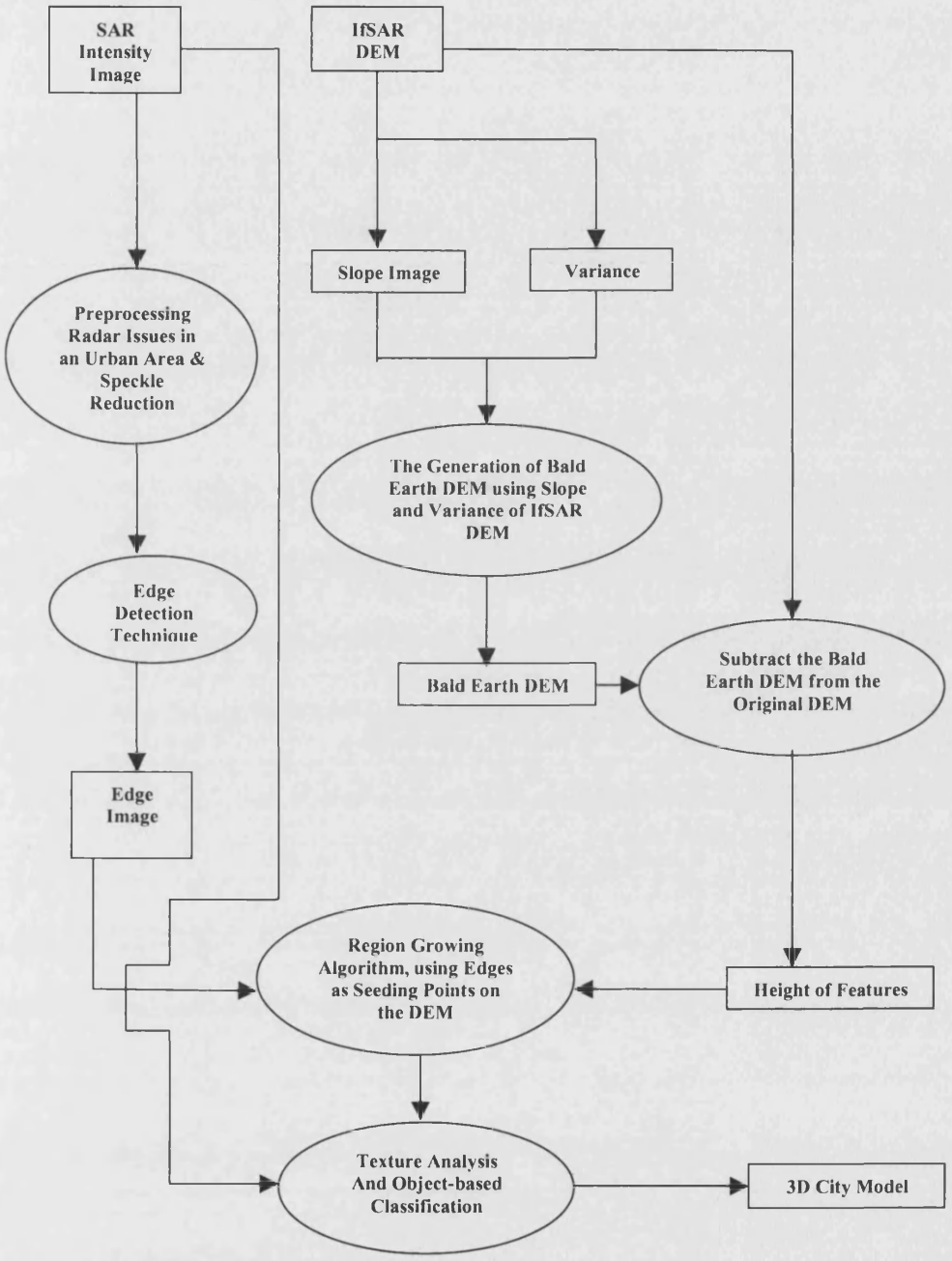

Figure 4.1 The flowchart of the processing procedure.

The detected edge does not only provide the information about the boundary of feature but is also used as the seed point for the later part of region growing. Since the SAR intensity image is noisy, it is expected that there are many small

edges detected. Thus, the non-maximal technique is applied to remove these small edges.

From the generation of bald earth DEM, the normalised DSM, which is the difference between the DSM and IfSAR DEM (DTM), theoretically, should contains only "off-terrain" points or features. But IfSAR DEM is noisy by its nature, and some ground points might be left on the normalised DSM. By using the boundary or edge as the seed point, the region growing technique, which is described in section 4.5, is able to provide a more clearly result of the "off-terrain" points or features than in the normalised DSM. Moreover, the small edges, which are left from the non-maximal process, are eliminated if those edges cannot provide any grown region. This serves as a self-checking algorithm, which takes care of these small edges. The small edges might be detected incorrectly, or detected correctly but the features, which provide the edges, are not significantly large enough to provide a region bigger than 1 pixel.

Results from region growing algorithm come in the form of polygons of features. Each polygon represents a feature, which consists of pixels. The object-oriented classification is then applied to classify the polygons not the pixels. The region growing works like a data format transformation from raster to vector data for classification. More on object-oriented classification and its benefit can be found in Chapter V.

4.3 Constrain-based Edge Detection

Many computer vision tasks start from a simple image description usually obtained by a contour extraction process. The latter involves three steps (Lacroix 1988): first, the local edge strength and direction are computed, then local maxima are selected, and finally edges are linked in order to form one-pixel-wide contours. The Gaussian gradient, first introduced by Marr 1982 and then justified by Canny, is a very efficient tool for the first step. However, as this operator is optimised for detecting a step edge in white noise, it hardly responds to thin lines and it does not respond at the middle but at each side of larger lines.

Most line detectors designed so far implicitly use an intensity model (Nevatia and Babu, 1980). Masks are used as templates: the best fit provides the operator output and the characteristics of the template are assigned to the pixel. The results thus depend on how well the templates may represent a give line. Other detectors use the gradient; in Burn et al 1986, for example, a segmentation based on the gradient orientation guides the road detection. Finally, some road finders use the edges as in Mckeown 1990, where the author defines road-centre hypotheses as anti-parallel intensity edges.

Edge detection is one of the fundamental operations in computer vision with numerous approaches to it. In an historical paper, Marr and Hildreth 1980 introduced the theory of edge detection and described a method for determining the edges using the zero crossing of Lapacian of Gaussian of an image. Haralick 1984 determined edges by fitting polynomial functions to local image intensities and finding the zero crossing of the second directional derivative of the functions. Canny determined edges by an optimisation process and proposed an approximation to the optimal detector as the maxima of gradient magnitude of a Gaussian-smoothed image. Clark 1989 and Ulupinar and Mdeioni 1990 independently found a method to filter out false edges obtained by the Laplacian of Gaussian operator. Bergholm 1987 introduced the concept of edge focusing and tracked edges from coarse to fine to mask weak and noisy edges. A curve-fitting approach to edge detection was proposed by Goshtasby and Shyu 1995 in which edge contours were represented by parametric curves that fitted to high-gradient image pixels with weights proportional to the gradient magnitudes of the pixels. Recent advances in edge detection include a method by Elder and Zycker 1998 to determine edges at multitudes of scales, and an adaptive smoothing method by Li 1998 to remove noisy details in an image without blurring the edges. Many other edges detection techniques have been proposed. From a survey and comparison of the edge detectors, the reader is referred to the paper by Heath et al 1997.

In this research, it shows that imposing constraints on the gradient field enables to enhance features such as lines or corners. Thus, a new method to

detect lines at their middle and corners without inspecting neither the local intensity nor the local curvature is proposed.

The technique is adapted from the Canny edge detection. A typical of the Canny edge detector follows the steps below (Ding and Goshtasby 2001).

1. Smooth the image with an appropriate filter to reduce undesired image details.
2. Determine gradient magnitude and gradient direction at each pixel.
3. If the gradient magnitude at a pixel is larger than those at its two neighbours in the gradient direction, mark the pixel as an edge. Otherwise, mark the pixel as background,
4. Remove the weak edges by non-maximal technique.

In order to make the technique suitable for noisy SAR image, Step 3 of the procedure has to be changed. In the SAR image, by applying the Canny edge detection alone, there are many edges that are missed because of the procedure on Step 3 of the technique (Ding, Goshtaby 2001).

The proposed technique, which details can be found in section 4.3.1, changes the Step 3 in the procedure to be as followed.

1. Smooth the image with an appropriate filter to reduce undesired image details.
2. Determine gradient magnitude and gradient direction at each pixel.
3. If there is, in the nearest neighbourhood, two gradient vectors pointing in opposite directions, at each side of the current, mark the pixel as an edge.
4. Remove the weak edges by the modified non-maximal.

Details of modified non-maximal technique can be seen in section 4.3.4. The proposed technique provides a more precise elimination of unwanted edge.

4.3.1 The gradient-based line detector

Gradient vectors located at each side of a bright/dark line are pointing towards/against each other at each side of the line. The scalar product of a displaced gradient vector is thus a good indication of the presence of a line. More precisely, consider the eight neighbours of a given pixel p, and arrange them in pairs (a_k, b_k) such that b_k is the symmetrical of a_k with respect to p as shown in Figure 4.2 a). If the dark lines are sought, only consider pairs such that:

$$\overline{d_k} \cdot \overline{G(b_k)} \geq 0, \tag{4.1}$$

where d_k denotes the displacement vector from p to b_k; in the case of bright lines, use the ≤ 0 instead.

Then, compute nk, the negative dot product of the gradient vectors taken at each pixel of such a pair:

$$n_k = -\overline{G(a_k)} \cdot \overline{G(b_k)} \tag{4.2}$$

The bar operator b at p is defined as:

$$b(p) = \max\{0, \max_k\{n_k\}\} \tag{4.3}$$

Let m denote the pair providing the maximum of the negative dot product as it can be seen in Figure 4.2 b). The local direction perpendicular to the bar is taken as the direction of the vector: $\overline{g_m} = \overline{G(a_m)} - \overline{G(b_m)}$. The output *b(p)* thus depends on the size and contrast of the line: a large-contrast line may produce the same output as a thin poor contrast line. If this is seen as a drawback, a further processing that produces an output proportional to the contrast of the line maybe used. Let c be the chain code associated to $\overline{g_m}$. Three other pairs are them investigated; they are made of the points lying in the directions c, c+1 and c-1 and their symmetrical pixel with respect to p. Let (u_k, v_k) with k =1, 2, 3 denote these pairs as in Figure 4.2 c). If the line is larger than one or two pixels, the gradient will be more important at u_k and at v_k than at a_m or b_m. The line detector computation will thus be larger for the pairs (u_k, v_k) than (a_m, b_m) pairs. A new approximation of the bar direction may then be computed at the pair providing the largest line detector; then, pairs lying in the further neighbourhoods maybe

investigated while the line detector output is larger. The number of times a further neighbourhood is investigated provides an approximation of the line width.

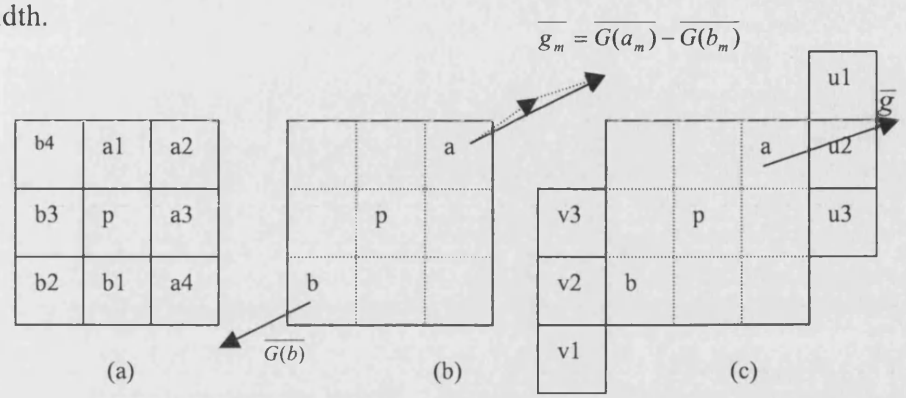

Figure 4.2 a) The (a_k, b_k) pairs. b) Direction perpendicular to the bar. c) Extended neighbourhood (Lacroix and Acheroy 1998).

According to this simple model, the operator will respond as long as there are, in the nearest neighbourhood, two gradient vectors pointing in opposite directions, at each side of the current pixel. The operator will thus respond at the centre of discs, along the skeleton of elongated blobs, and on any curvilinear line, even if the latter does not have a constant width; it may also respond at the beginning of diagonals of triangles. To be more precise, it will respond as long as the angle between the gradient vectors of one of the explored pair is larger than 90 degrees. Thus, the technique is a rotationally symmetric detector, in which gradient magnitude of an edge is not affected by its orientation. Gradient direction is an accurate estimate of the edge orientation. It is sensitive to the sub-pixel location of an edge (Ziou 2001). A post-processing might be necessary to remove the undesired features in which will be described in the later part.

4.3.2 The gradient-based corner detector

A corner is characterised by a local change in the contour direction. The cross product of two parallel vectors is null while it is maximum when the vectors are right angle. Corners occur at edge points in which a significant

change in gradient direction takes place. Thus, we developed an operator that exploits this property.

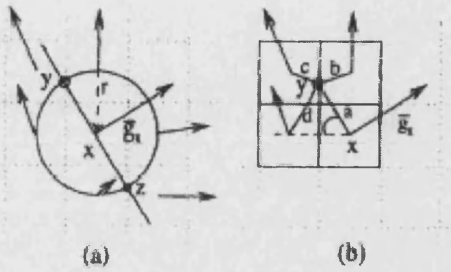

Figure 4.3 Corner computation: a) gradient vectors involved in the corner computation at *x*; b) coefficients involved in the computation of the gradient at *y* (Lacroix and Acheroy 1998).

The gradient is evaluated at y and z, two points located at the intersection of a line and a circle, the line being the normal to the gradient direction at the current pixel x, and the circle being centred at x with a radius r equal to one as it is displayed in Figure 4.3. We have tested several measures using the gradient at x, y and z. The best results were obtained by the following computation: as x should be corner point, we first require the two cross products $\overline{g(y)} \otimes \overline{g(x)}$ and $\overline{g(x)} \otimes \overline{g(z)}$ to have the same sign. The corner measure is then:

$$C(x) = \frac{\overline{g(y)} \otimes \overline{g(x)} + \overline{g(x)} \otimes \overline{g(z)}}{\max\{\overline{g(y)}, \overline{g(z)}\}} \tag{4.4}$$

The numerator depends on the variation of gradient direction in the pixel neighbourhood and on its norm. Taken alone, it would generate high responses in the presence of high gradients of slightly different directions; the denominator thus compensates for this effect and by the same time sets the corner output range to the gradient output range. This makes an improvement of corner measure as proposed in Lacroix and Acheroy 1996.

The gradient at y and z is computed using a linear combination of the gradient at the four nearest neighbours. The coefficients of the combination are inversely proportional to the distance to the nearest neighbours. These distances are labelled a, b, c, d, so we have:

$a = 1$

$b = \sqrt{2(1-\sin\alpha)}$

$c = \sqrt{1+d^2-2d\cos\alpha/2}$

$d = \sqrt{2(1-\cos\alpha)}$

Dark corners in which: $\overline{g(z)}\cdot\overline{d_z} \geq 0$, where $\overline{d_y}$ and $\overline{d_z}$ respectively denote the vector from x to y and from x to z; bright corners are obtained using the $\leq$ condition instead.

4.3.3 Gradient assessment

Before performing the edge detection and gradient computation, it is necessary to decide whether or not an observed gradient magnitude G is statistically significant and therefore participates in some edges it to decide there is an edge (statistically significant gradient) when,

$$P(\text{edge}|G) > P(\text{nonedge}|G) \tag{4.5}$$

By definition of conditional probability,

$$P(\text{edge}|G) = [P(G|\text{edge})P(\text{edge})]/P(G)$$
$$P(\text{nonedge}|G) = [P(G|\text{nonedge})P(\text{nonedge})]/P(G) \tag{4.6}$$

Hence the decision for edge is made whenever,

$$P(G|edge)P(edge) > P(G|nonedge)P(nonedge) \quad (4.7)$$

From Haralic and Shapiro 1992, P(G|nonedge) is known to be the density function of a χ_2^2 variate. But P(G|edge) is not known.

It is possible to infer P(G|edge) from the observed image data since P(G), the density function of the histogram of observed gradient magnitude, is easily calculated. Now,

$$P(G) = P(G|edge)P(edge) + P(G|nonedge)P(nonedge) \quad (4.8)$$

Hence,

$$P(G|edge) = [P(G)-P(G|nonedge)P(nonedge)]/P(edge)$$
$$= [P(G)-P(G|nonedge)P(nonedge)]/[1-P(nonedge)] \quad (4.9)$$

This means that once the prior probability for nonedge is specified, the density function for P(G|edge) can be calculated. Once P(G|edge) is known, the appropriate threshold t for G is determined as the value t for which

$$P(t|edge)P(edge) = P(t|nonedge)P(nonedge) \quad (4.10)$$

This relation, together with the relationship for P(G |edge), implies that the threshold t must satisfy

$$P(t) = 2P(t\ |nonedge)P(nonedge) \quad (4.11)$$

Hence $P(t)$ is the observed density for the test statistic G evaluated at t, $P(t|nonedge)$ is the value of the density function of a χ_2^2 variate evaluated at t, and P(nonedge) is a user-specified prior probability of nonedge.

For the module, the Hummel and Lowe implementation of Gaussian gradient (Hummel and Lowe 1988) is applied. It is the most attractive approach as it is based on the gradient of the intensity regularized by a Gaussian, the only regularizing function that is separable and isotropic (Lacroix and Acheroy 1998).

The x component of the gradient is computed by first convolving the columns of the image with a mask c[j] = R[j], then convolving the lines of the resulting image with a mask d[I] = -∂R(i), where R(i) and ∂R(i) are the mean value of a 1D Gaussian over the interval [i–0.5, i+ 0.5] and of its derivative respectively. As masks are finite, the last coefficient at r is computed from the mean over the interval [r-0.5, ∞]. More precisely;

$$c[j] = 0.5erf(j + 0.5/\sqrt{2\sigma}) - erf(j - 0.5/\sqrt{2\sigma})), for 0 \le j \le r_j$$

$$c[r_j] = 1 - \sum_c j$$

$$c[j] = c[-j] \text{ for } j < 0$$

$$d[I\} = e^{-((I-0.5)/\sqrt{2\sigma})^2} - e^{-((I+0.5)/\sqrt{2\sigma})^2} \text{ for } 0 \le I \le r_i$$

$$d[r_i] = 1 - (1 - e^{-(0.5/\sqrt{2\sigma})^2}) - \sum d[i]$$

$$d[i] = -d[-I] \text{ for } I < 0$$

Inverting the role of lines and columns provides the y component. The first module thus outputs two real raster $G_x(I, j)$ and $G_y(I, j)$.

4.3.4 The Non-Maximal

In order to eliminate unwanted pixels or those, which are not local maximal from edge image, the non-maximal suppression algorithm has to be applied by using Lewis 1988 techniques adapted from Canny. Canny developed an algorithm where an edge pixel is passed if its strength is greater than the two pixels which lie on a line parallel to the gradient of the edge in equation and on either side of the edge (see Figure 4.4)

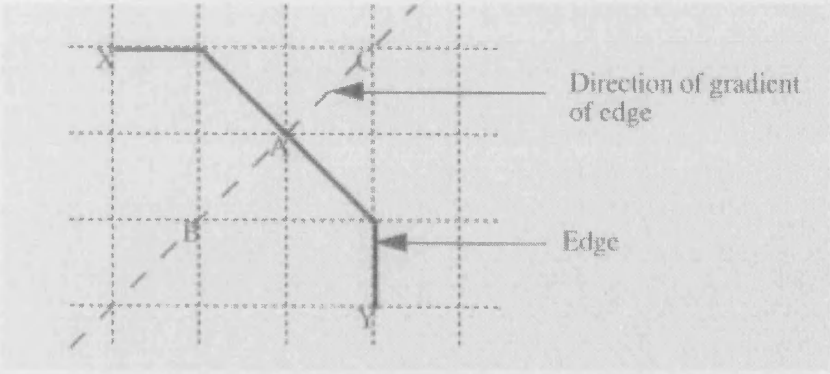

Figure 4.4 Canny Non-Maximal (Lewis 1988).

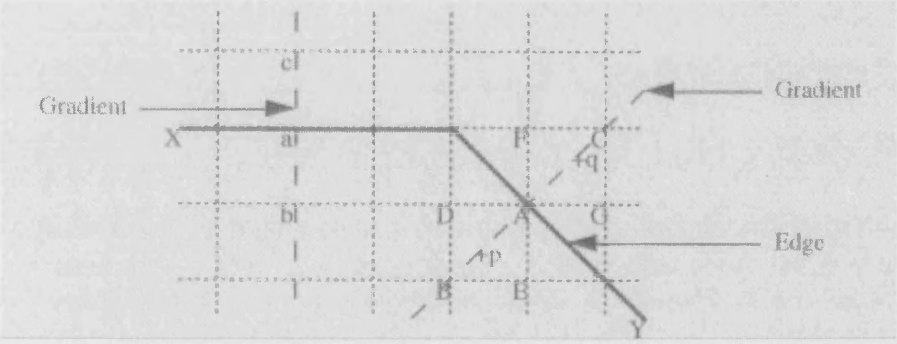

Figure 4.5 Adapted Non-Maximal (Lewis 1988).

In Figure 4.4, the pixel in the equation is at A and the edge runs from X to Y. At A the direction of the gradient of edge is NE and SW. Therefore, if the strength of A is greater than the strength of both B and C then it is passed, else it is eliminated. Lewis recognized that this method of comparing the strengths of pixels was inconsistent for edges with different directions. In Figure 4.5, pixel *a* is compared with pixels *b* and *c* to see if it should be passed. Likewise, pixel A is compared with pixels B and C. however, distance *bc* is much less than distance BC, giving the inconsistency. The strength of A should really be compared with the strengths of *p* and *q*. these strengths are calculated by linear interpolation between the points B, D, E and C, F, G respectively. The result is that the adapted non-maximal suppression is more accurate. It is necessary to threshold the edge image in order to suppress edges which are not wanted, but were not eliminated by the non-maximal suppression routine. Unfortunately it is

sometimes found that edges, which delineate important features in the image may in places be weaker than unwanted edges and therefore automatic thresholding of the edge image somehow is very difficult. Many very complex algorithms and techniques are required for automatic thresholding. Furthermore, those algorithms required a number of parameters to be set and hence the solution is far from automated.

4.4 Generation of Bald Earth DEM

DEMs created by Interferometric SAR (IfSAR) have created a new wide-area availability demonstrated by SRTM's global data set on the one hand and by the STAR-3i airborne IfSAR on the other. The STAR-3i DEM is normally produced at 5meter postings with an accuracy at the 1-2 meter (RMS) level and as such provides a level of detail that approaches that of Lidar while retaining wide area coverage and lower cost (Sties et al, 2000). The day/ night cloud penetration advantages of radar are well known, and this, together with its high altitude and fast flying platform, contributes to the rapidity with which it is able to acquire data. However among its limitation is the fact that the DEM thus created is a 'first surface' model –more correctly called a Digital Surface Model (DSM). Like other technologies, it responds to the surface of the scattering object situated on the terrain surface such as buildings or a soft object such as an individual tree or a wooded area. For many applications a so-called 'bald-earth' or 'bare-surface' DEM is required. This is one for which objects situated on the terrain surface has been removed. Irrespective of the technology, photogrammetric, Lidar and IfSAR, editing is usually invoked to create bald-earth DEMs.

In recent year, some efforts have been made on this subject and a number of methods have been developed. Various methods for the automatic detection of buildings and trees from high-resolution digital surface models have been developed (Haala and Brenner, 1999; Soergel et al, 2000; Wang and Scheknk, 2000). Some methods use image-processing techniques such as classification method and image understanding methods to remove buildings and trees (Lu et

al, 1998). Due to the complexity of remotely sensed imagery, objects cannot be classified accurately with the existing classification method. As well, image understanding techniques are not mature enough to recognize objects from image reliably. Zhang and Tao 1999 proposed a method for automatic generation of bald earth DEMs based on observation that local minima usually correspond to true terrain points. In their method, local minima are extracted and false terrain points are removed by comparing them with a trend surface, which is determined by surrounding terrain points. This method generally works well in residential areas, but needs further improvements to deal with mountainous areas (Tao et al, 2001). There is also a technique developed by Intermap and University of Calgary in Canada: TerrainFit® is a method of removing objects from the terrain surface while retaining the details in that surface, which is fully automated and runs on desktop PC. In standard production mode, false stereo image pairs are created from the corresponding orthorectified radar images (ORRIs) and are taken, together with the TerrainFit ground points, into a stereo editing environment, where additional quality control and editing activities take place manually (Coleman and Mercer, 2002).

In this chapter the method of generation of bald earth DEM from IfSAR DSM is presented. The method uses an image pyramid of input DSM data, and generates bald earth DEMs hierarchically through this pyramids. It is assumed that true terrain points usually correspond to local minima when the terrain is relatively flat, and therefore objects on the terrain such as buildings and sparse trees can be removed through the generation of image pyramid. An approximate bald-earth DEM can be derived from the image at the top of the pyramid by interpolation. In order to obtain an accurate bald earth surface, images at lower levels in the pyramid are used since they are resampling at higher resolution. The generated bald surface at each level is used as a reference for the image at the next level to eliminate false terrain surface points and the remaining terrain points are used to interpolate a new bald earth surface. This process is repeated through the image pyramid until the bottom level is performed.

Due to the effects of rapidly changing terrain slope, the generated bald-earth DEMs can be incorrect in some areas. To mitigate these problems, a self-diagnostic process is incorporated in the method that can locate problem areas and correct them automatically based on the difference map, i.e. the difference between the original DSM and the generated bald earth surface.

4.4.1 Generation of bald earth DEM by Hierarchical surface fitting

Generation of an image pyramid is actually a process of image filtering in which high-frequency components are filtered out. For digital surface data, objects on the ground such as buildings and trees are removed during the creation of the image pyramid. Therefore, a bald earth DEM can be generated from the image data at the top of the pyramid. However, the generated bald-earth DEM is inaccurate due to the low spatial resolution of the top image. To obtain an accurate bald earth DEM, high-resolution image data, i.e. images at lower levels of the pyramid should be used. In images at lower levels of the pyramid, some points are not true terrain points when they are on top of buildings or trees. Points on top of buildings and trees must be removed before a bald earth DEM is interpolated. In order to eliminate these points, the generated bald earth DEM at a higher level is used as a reference surface and points with a distance to the reference surface larger than the given threshold are removed. In this way, no-terrain surface points are removed and bald earth DEM can be interpolated hierarchically. The main advantage of the hierarchical surface fitting method is that objects on the ground with widely varying spatial extents, such as buildings and trees, can be removed more reliably and thus, a more accurate bald earth DEM can be produced. The process consists of the generation of an image pyramid from the original DSM data, the derivation of an initial bald earth DEM, the extraction of terrain surface points and the interpolation of the bald-earth surface

4.4.2 Generation of DEM Pyramid

An image pyramid is a series of images with different resolutions, which are usually generated, from the original image by resampling. There are two common ways for resampling an image. One is to take the average of pixels in a defined window and the other is to convolute the original image with a kernel function, for example Gaussian function. The image pyramid used in this study is different from the traditional one in image processing in two aspects. First, the value of a pixel in an IfSAR DEM image represents the elevation of a terrain point instead of the grey value expressing the reflectance of terrain or an object in a small area. Secondly, the image at a higher-level in the pyramid is generated by taking the minimum value in the search window from the IfSAR DEM using the bigger searching window than in the lower-level image. In this way, the points on buildings, trees, and noisy data can be removed gradually. The total number of levels of the image pyramid depends on the spatial resolution of the input DSM data and the maximum size of buildings to be removed from the DSM data.

It is assumed that non-terrain surface points are removed during the generation of the image pyramid and the remaining pixels at the top-level image of the pyramid are true terrain surface points. Thus a true bald-earth DEM can be generated by interpolation. The levels of image pyramid can be seen in Chapter 5.

4.4.3 Hierarchical Interpolation of Bald Earth DEM

Due to low-spatial resolution of the top image in the pyramid, the derived bald earth DEM is inaccurate and cannot be used as the final product. To yield an accurate bald earth surface, the images at lower levels of the pyramid are used and a bald earth surface is generated hierarchically through the image pyramid. At each level, various types of terrain points are extracted and evaluated using original IfSAR DEM surface as a reference surface. A more accurate surface is

then interpolated using the verified terrain surface points. This process is repeated until the image at bottom level is reached.

To interpolate a bald earth surface at each level, terrain surface points should be extracted. In order to extract these points some conditions should be set. Considering the complexity of the terrain surface, other types of terrain surface points such as slope points and points in flat area are also detected in addition to local minimal. From the information provided, the strategy to extract surface point can be set by using 2 main parameters: slope and variance of the surface. Slope parameter is used for eliminating the edge points or wall type of points. Even though the surface of the terrain is quite rough and the true surface is known not to be so smooth, but the slope of the points are still relatively flat compare to the edge or wall type of points. The variance value is set to eliminate points at the top of the feature. At the top-level image with a large resolution, the big features can be eliminated and in the lower level image with finer resolution small features can be eliminate. Thus, the true terrain points can be extracted more accurately.

Since not all the extracted points are true terrain surface points, false terrain points should be removed before a bald earth DEM interpolated. As one point has very limited information, it is difficult to differentiate between a true terrain surface point and a false point by using information associated with it alone. To eliminate spurious terrain surface point effectively, the extracted points are compared with the derived bald earth DEM. When the distance from a point to reference surface is larger than the given threshold, it is considered as a spurious surface point. The criterion for eliminating spurious surface points can be described as:

If $|h_i - h_i^0| < T_h$, point I is accepted, otherwise it is a spurious point.

When h_i and h_i^0 are the elevation of points I on the original DSM and reference surface respectively. And T_h is threshold value.

The threshold value is then set according to the first evaluation of the IfSAR DEM. Since the accuracy of the *STAR-3i,* is around 2m (Mercer and Schnick, Sties et al 2000, Xiaopen et al, Fisher and Dowman 2002). The threshold value then set to be 2m. The point, which the difference is more than 2m, is then eliminated.

To interpolate a bald earth surface at each level, terrain surface points should be extracted. To create an accurate bald earth surface, sufficient terrain points should be used. It is assumed that local minima in DSM images usually correspond to true terrain surface in residential areas. Considering the complexity of the terrain surface, other types of terrain surface points such as slope points and points in the flat areas are also detected in addition to local minima.

4.4.4 Interpolation of Bald Earth Surface

After false terrain surface points are removed, the remaining points are used to interpolate a new bald earth surface. There are a number of methods available for DEM interpolation. Two of the well known are Spline and Inverse Distance Weighted (IDW).

Spline is the technique that fits a minimum curvature surface through the input points. Conceptually, it is like bending a sheet of rubber to pass through the points, while minimizing the total curvature of the surface. It fits a mathematical function to a specified number of nearest input points, while passing though the sample points. This method is best for gently varying surfaces where change in physiography or other phenomenon is not abrupt. It is not appropriate if there are large changes in the surface within a short horizontal distance because it can overshoot estimated values. The regularised method yield a smooth surface as the weight parameters defines the weight of the third derivative of the surface in the curvature minimisation expression (Unser 1999).

IDW is interpolation technique weights the contribution of each input points by a normalised inverse of the distance from the control point to the

interpolated point. IDW assumes that each input point has a local influence that diminishes with distance. It weights the points closed to the processing points, greater than those farther away. A specified number of points, or all points within a specified radius is used to determine the output value for each location. The power parameter in the IDW interpolator controls the significance of the surrounding points upon the interpolated value. A higher power results in less influence from distant points. Each line in a barrier input line theme is used as break that limits the search for input sample points. A line can represent a cliff, ridge or some other interruption in a landscape. A choice of number of barriers will use all points specified in the number of neighbour or within the identified radius (Shepard 1968, Fisher et al 1987).

The results from the two interpolation techniques are different. The studies suggest that neither estimation process could be generalised for a particular application. Thus, the choice of proper interpolation technique is highly area specific. Again spline suits to those areas where there are little variations in the data within a short horizontal distance. IDW on the other hand suits for such kind of data, in which the value has a local influence that diminishes with distance. Since there are a lot of variations in the generated bare-earth DEM in the entire area and with the prior knowledge of the physiography of the area, the result obtained from IDW interpolation is found to be closer to the expected value. Therefore, IDW interpolation technique was found more appropriate for this application.

Since the points are not scattered evenly and covered all the area, the "gap" in which the interpolation cannot be performed is expected. There are many techniques to fill this gap. But in this research, the gap is left unfilled and the areas of the gap are not used for the further processing. Figure 4.6 a) displays finale result of the bald earth DEM and Figure 4.6 b) displays the original IfSAR DEM (DSM).

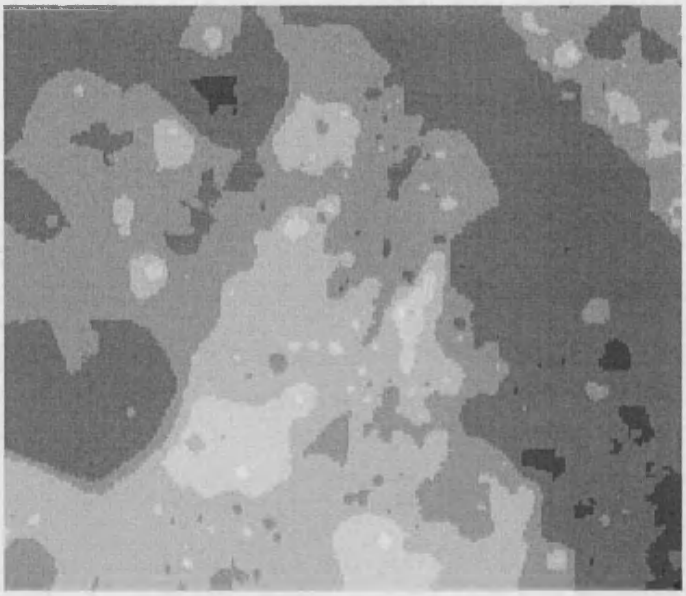

(a)

(b)

Figure 4.6 a) The generated bald earth DEM. b) The original IfSAR DEM (DSM).

4.5 Region Growing from Edge Detection

4.5.1 The technique

From the bald-earth DEM, the feature surface can be obtained by subtracting the IfSAR DEM by the generated bald-earth DEM. Still, some features are not clearly distinguished from the ground as it is shown in the Figure 4.7. It is necessary to completely separate the features out from ground and group them together for later feature classification.

Figure 4.7 The Normalised DEM, IfSAR DEM subtracted by generated Bald Earth DEM

Normally, in order to perform region growing technique, the seed points are needed at the beginning as the starting point. The point must be part of the feature otherwise the grown region would not be the wanted feature. But in our research, it is clearly known that the detected edge from edge detection is definitely part of the feature. So, instead of wasting time to search and plant the seeding point, the edge and corner point can be used as the seeding point for the region growing. The edge would be more precise than the searched points. Moreover, the final grown region would be more accurate in term of size and shape because the edges could be the vital parameter to limit the size of the

feature as it is assumed that pixels grown from the same seed edge should be the same feature. And this could lead to a less confusing process of region merging and splitting. This processing might not be the really region growing, it is more about grouping pixel together into feature.

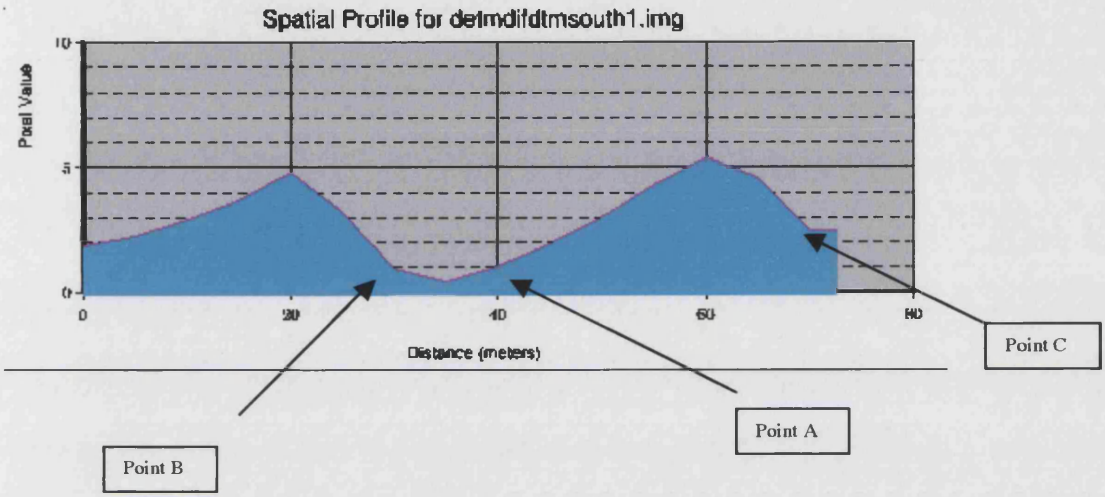

Figure 4.8 Profile of 2 buildings from the feature surface.

In Figure 4.8, the profile from "feature surface" of 2 buildings is shown. Point A, B and C are the point represent where the edges are, in which is the starting point for region growing. There are two main conditions for the region growing. The first one is the region growing would perform up the slope of the feature. And the latter one is that the point in which its height is lower than the height of the edge will not be part of the feature. As it is noticeable that at the side of feature, the slope value would be very high, compared to the ground point or top of the feature. Thus it can count as part of the feature. While the top of the feature, where the slope is estimated to be around the same as the ground, can be distinguished from ground by the second condition. The point whose height is lower than the height of the edge will not be count as the feature, so the ground point will be eliminated and the point at the top of the feature where its slope is low still be part of the feature. Mathematically, the notion of topographic

structure on continuous surface can be formulated. The following mathematical parameters are used to form the equation for topographic structure:

∇f = gradient vector of a function f

$||\nabla f||$ = gradient magnitude

$\varpi^{(1)}$ = unit vector in the direction in which the second directional derivative has the greatest magnitude

$\varpi^{(2)}$ = unit vector orthogonal to $\varpi^{(1)}$

λ_1 = value of the second directional derivative in the direction of $\varpi^{(1)}$

λ_2 = value of the second directional derivative in the direction of $\varpi^{(2)}$

$\nabla f \cdot \varpi^{(1)}$ = value of the first directional derivative in the direction of $\varpi^{(1)}$

$\nabla f \cdot \varpi^{(2)}$ = value of the first directional derivative in the direction of $\varpi^{(2)}$

A study (Haralic and Shapiro 1992) has established the relationships between these parameters and concluded it in Table 4.1.

$\|\nabla f\|$	λ_1	λ_2	$\nabla f. \varpi^{(1)}$	$\nabla f. \varpi^{(2)}$	Label
0	-	-	0	0	Peak
0	0	0	0	0	Flat
+	-	-	-, +	-, +	Hillside (concave)
+	0	0	*	*	Hillside (slope)
+	+	0	-, +	*	Hillside (convex)

Table4.1 Adopted from Haralic and Shapiro 1992. Mathematic properties of topographic structure. 0 means not significantly different from zero; + means significantly different from zero on the positive side; - means significantly different from zero on the negative side; and * means it does not matter.

The single linkage region growing technique is most suitable because the scheme regards each pixel as a node in a graph. Neighbouring pixels, whose properties are the same as the conditions, are joined by an arc or edge in this case. It is more suitable than Hybrid-linkage since the hybrid-linkage depends so

much on edge detection, which may provide too much region linkage. Furthermore, a region cannot be declared a segment unless it is completely surrounded by edge pixel. That would cause problems in the case of edges with gaps or unclosed edges.

4.5.2 Region merging and splitting

From region growing, there are many small features or polygons created along with the big features or polygons. Some are from the real same feature and some are not. The first separation between these polygons can be done by looking at its original of the region growing. That can provide the first separation clue since if the polygons are generated from the same origin edge they should be from the same real feature. Nevertheless, the edge from the edge detection might include edge from other features or exclude edges from its own real feature. Some small polygons as small as one pixel might also generated. It is necessary to merge or split these polygons. Even though polygons are generated from the DEM, but the merging and splitting perform under the information from the intensity image. Statistics of each polygon are taken from the intensity image, since the statistics from intensity image could provide characteristics of the returning signal of the features, which is helpful in determination whether features are the same. Moreover, statistics from the DEM are not able to provide enough accurate information to perform merging and splitting.

Both splitting and merging depend on estimating whether two regions belong to the same population or not. The crucial issue is whether the decision to merge is reliable, which depends on the statistical criterion adopted to control merging. In fact, an identical criterion can be used to describe both splitting and merging. Merging using Moments, MUM, is based on the student t-test, is one of the merging implementation. For the sub-polygon A and B, calculation of co-variance is:

$$\text{var}\{A+B\} = (N_a \text{ var } A + N_b \text{ var } B) / (N_a + N_b - 2) \text{ x } (1/N_a + 1/ N_b) \quad (4.12)$$

where var A, var B and var {A+B} are the variances and N_a and N_b are the number of pixels in each polygon, respectively.

Then the normalised difference could be calculated:

$$t \equiv |A - B| / \sqrt{(\text{var}\{A+B\}} \quad (4.13)$$

and apply the student *t*-test for $N_a + N_b - 2$ degree of freedom to the data. This evaluates the probability that A and B should be merged. There is a study suggests that the method of merging using moment or covariance analysis is somehow not appropriate because of the speckle in the SAR image. But since in this part of the research, the image had been through the speckle reduction process, effects from speckle, which would influence the performance of the technique, would be minimal.

The result of the region growing process with region merging can splitting can be seen in Figure 4.9.

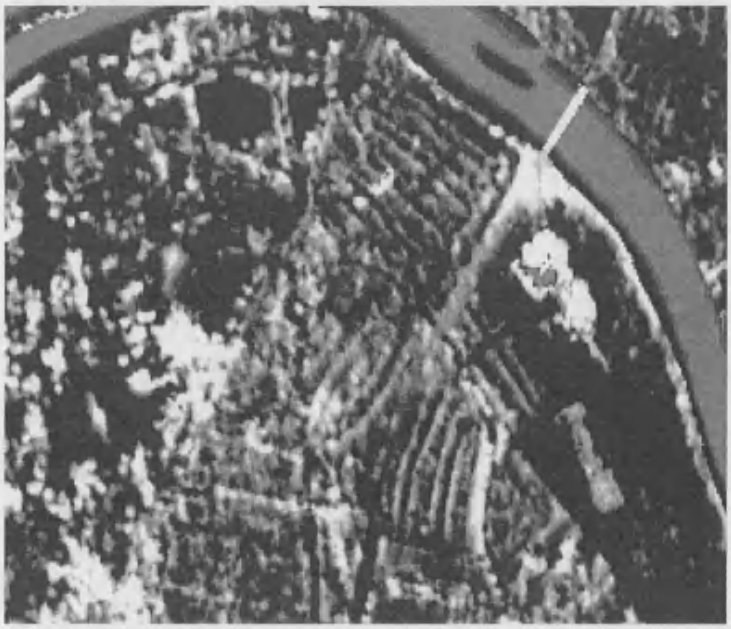

Fixture 4.9 The Final product from region growing with merging and splitting.

4.6 Conclusion

From edge detection from SAR intensity image, generation of bald earth DEM and region growing from edge detection from IfSAR DEM, the data from airborne SAR/IfSAR has shown its capability for feature extraction in an urban area without any other help from other type of dataset.

From edge detection technique, the gradient field using either the dot product or the cross product of displaced vectors helps the extraction of features such as lines and corners. The line extraction operator presents several interesting aspects: it produces a clean output, it can cope with noise in the intensity image, it detects straight and curvilinear lines of various widths, it may generate an output dependent on the line contrast, and it may provide approximation of the local line width and direction. The edge detection technique not only provides the boundary of feature but also can be used as seeded point for region growing algorithm. This technique eases the problem of finding a seeded point and since the seeded point is the edge of the feature itself, the result is expected to be more accurate.

The generation of bald earth DEM by using image pyramid and hierarchical interpolation yields a good compromise result between elimination of features and losing the true elevation height. The method incorporates a self-diagnostic process for automatically locating problem areas using a difference level created from the intermediate bald-earth DEM and the original DEM. this is very important because the method does not need human intervention before a final bald earth DEM is generated. A small of residual errors may remain in the derived surface, which require manual editing at the final.

The feature surface, in which generated from subtracting IfSAR DEM from the bald earth DEM, might not purely contain the height of feature but some of ground points might be included in the surface image. Though it would be eliminated in the process of region growing.

The Region growing process has shown a good performance in generation of feature objects. The main problems of the technique are that small features would be easily neglected. And only features with height can be

extracted. Features without height such as road, walkway, cannot be extracted. But these are also advantages in the sense that small unwanted edges which got through the non-maximal process are eliminated at this process if they cannot provide any feature object from region growing.

Chapter V
Theory of Texture Analysis & Classification

5.1 Introduction

Having introduced the data model for SAR intensity image in Chapter 2, the concepts for that chapter are now applied on this chapter for feature classification and texture analysis. In the first half of this chapter, the texture analysis is described as a continued part of the data model from Chapter 2. This consists of texture analysis from data model and texture analysis for object based classification. In the later half of the chapter, the object oriented classification technique is stated. This includes human perception and object oriented analysis, why object oriented analysis, and concept and classification at the final part of the chapter.

5.2 Texture analysis

From the result of the data model in chapter 2 and speckle reduction in chapter 3, the information in the intensity image is carried at the single-pixel level. However, this is not the only type of information contained in a SAR image. In an urban area scenario, there are many objects in the area. Regions of buildings, trees and others are comprised in the scene. Suppose that the classification of remote sensing data is to distinguish those regions that correspond to buildings and trees. It is apparent that the radar return in the image falls into two categories. One is corresponding to the trees and green areas. The others correspond to building areas.

It is demonstrated in chapter 2 that clutter textures could be described by the normalised variance. Thus, single-point texture statistics can be utilised as a mean of characterising clutter in image interpretation. This chapter is concerned with establishing optimum means for extracting the texture information for object-oriented classification.

5.2.1 Data model and texture analysis

In this section, how texture information can be derived without any knowledge of the data distribution is briefly discussed. However, where prior knowledge of the form of PDF is available, it should be exploited. Model-based texture parameter estimation is discussed in the later part of this section as well as Maximum Likelihood texture estimators for various forms of PDF, leading to texture measures that can be used in texture characterisation.

5.2.1.1 Model-free texture exploitation

It is not possible to select texture measures that optimise the information content without a specific model for the data. However, suboptimal results can be obtained with noncommittal approaches. For example, The Kolmogorov-Smirnov test, K-S test, compares Comulatives Distribution Function, CDF of two data sets. Alternatively, moments of the data PDF might be compared (Stephens 1970, Press et al 1994). The ability to discriminate between textures would then depend on the accuracy with which these moments were estimated (Oliver and Quengan 1998). The selection of which particular moment to adopt is crucial. If the form of the PDF is know, then those moments that optimise the information about the texture can be selected. Some simple moments are able to optimise the particular form of PDF (Lombardo and Oliver 1994). And the form of the data PDF can be approximated in terms of a mixture of simple analytic distributions, each of which possesses an analytic solution (Blacknell 1994, Luttrell 1990).

This whole section is to point out that if the data model of the data is unknown, there are still some methods available to solve the statistic distribution for the data set.

5.2.2.2 Model-based texture parameter estimation

So far, none of models for data, in attempting to derive information from the texture have been exploited. However, the previous section indicates that an optimum texture measure is determined by the form of the data. For the remainder of this section it is assumed that a data model is known, characterised by its single point PDF. This PDF then determines optimum measures for texture parameters and classification.

1. *Derivation of Maximum Likelihood Estimates (MLE) for different PDFs*

In this section MLEs for the parameters values are derived, implied by assuming different forms of PDF to characterise the data. These different PDFs, introduced in Chapter 2, lead to a variety of texture measures.

1. Gaussian Distribution

Suppose the data have a Gaussian PDF of the form

$$P(x) = \frac{1}{\sqrt{2\pi V}} \exp[-\frac{(x-\mu)^2}{2V}] \tag{5.12}$$

where μ and V represent the mean and variance of x. The resulting log likelihood over N pixels is given by

$$\lambda = -\frac{N \ln(2\pi V)}{2} - \frac{N\overline{(x-\mu)^2}}{2V} \tag{5.13}$$

with MLEs for mean and variance given by

$$\mu = \bar{x} \text{ and } V = \overline{x^2} - \bar{x}^2 \tag{5.14}$$

This Gaussian PDF could represent either the intensity or the amplitude of the data. Self-normalised texture measures of the form

$$V_I \equiv \frac{\overline{I^2}}{\overline{I}^2} - 1 \tag{5.15}$$

And

$$V_A \equiv \frac{\overline{A^2}}{\overline{A}^2} - 1 = \frac{\overline{I}}{\overline{A}^2} - 1 \tag{5.16}$$

have been proposed (Oliver 1993, Blacknell 1994, Lambardo and Oliver 1994) for intensity and amplitude data, respectively, which would therefore be ML measures when the appropriate PDF was Gaussian.

2. Log Normal Distribution

Suppose the data follow a log normal distribution of the form

$$P(x) = \frac{1}{x\sqrt{2\pi W}} \exp[-\frac{(\ln x - \beta)^2}{2W}] \tag{5.17}$$

where β and W are the mean and variance of ln x. The associated log likelihood is given by

$$\lambda = -\frac{N}{2}\ln(2\pi W) - N\overline{\ln x} - \frac{N\overline{(\ln x - \beta)^2}}{2W} \tag{5.18}$$

and the MLEs of β and W by

$$\beta = \overline{\ln x} \text{ and } W = \overline{\ln^2 x} - (\overline{\ln x})^2 \tag{5.19}$$

The variance of log measure for intensity, defined by

$$V_L \equiv \overline{\ln^2 I} - (\overline{\ln I})^2 \tag{5.20}$$

has also been proposed as a suitable texture measure (Kreithen et al 1991)

3. The K Distribution

Chapter 2 showed that natural clutter can often be represented by a K distribution of the form

$$P(I) = \frac{2}{\Gamma(L)\Gamma(\nu)}(\frac{L\nu}{\mu})^{\frac{L+\nu}{2}} I^{\frac{L+\nu-2}{2}} K_{\nu-L}[2\sqrt{\frac{\nu LI}{\mu}} \tag{5.21}$$

For L-look SAR, where μ and ν are the mean and order of the intensity PDF, respectively. In this case the associated log likelihood is

$$\lambda = N\ln[\frac{2}{\Gamma(L)}] - N\ln\Gamma(\nu) + \frac{N}{2}\ln[\frac{L\nu}{\mu}] + N(\frac{L+\nu-2}{2})\overline{\ln I} + N\overline{\{\ln K_{\nu-L}[2\sqrt{\nu LI/\mu}}$$

(5.22)

Unfortunately, there is no exact analytic form for the partial derivatives of the last term in (5.22), which prevents a derivation of the MLEs. These have to be determined by a numerical search over μ and ν to find the largest value of λ; the corresponding values of μ and ν are the MLEs. Since this is very time consuming, it is useful to provide approximate forms for the K distribution that have analytic solutions.

An analytic (Oliver 1993) approximation of a K distribution intensity in the limit of large L is

$$P(I) = \frac{\sigma^{\nu-1}}{\Gamma(\nu)}(\frac{\nu}{\mu})\exp[-\frac{\nu I}{\mu}] \times \{1 + \frac{\nu}{L}(1+\nu - \frac{2I(1+\nu)}{\mu} + \frac{\nu I^2}{\mu^2})\} \tag{5.23}$$

leading to a log likelihood over N samples give by

$$\lambda = Nv\ln v - Nv\ln\mu - N\ln\Gamma(v) + N(v-1)\overline{\ln I} - \frac{v\bar{I}}{\mu} + \frac{1}{2L}\{Nv(1+v) - \frac{2Nv(1+v)\bar{I}}{\mu} + \frac{v^2\overline{I^2}}{\mu^2}$$

(5.24)

The MLEs for mean and order are then give by

$$\mu = \bar{I}(1+\frac{1}{L}(1+v-\frac{v\overline{I^2}}{\mu^2})) \tag{5.25}$$

and

$$\ln v - \psi^{(0)}(v) + \frac{v}{L}(\frac{\overline{I^2}}{\bar{I}^2}) = \ln\bar{I} - \overline{\ln I} + 1/2L \tag{5.26}$$

These reduce to the results for a gamma distribution as $L \to \infty$ when speckle contributions would be averaged out. Note that the right hand side of (5.26) involves a normalised log measure, define by

$$U \equiv \overline{\ln I} - \ln\bar{I} \tag{5.27}$$

which has been used as a texture measure (Lombardo and Oliver 1994, Oliver 1993). When (5.26) is inverted it provides a close approximation to the ML solution for the order parameter for K distributions with large numbers of looks, and is exact for a gamma distribution. However, the normalised log in (5.27) provides a poorer approximation to an ML estimate for v single-look images. It corresponds to approximating a K distribution by a gamma distribution, as proposed by Raghavan (Raghavan 1995), and has been widely applied widely in texture analysis (Lombardo and Oliver 1994, Blacknell 1994, Oliver 1994).

5.2.2.3 *Uncertainty in order parameter estimates*

In the previous section ML texture measures V_P, V_A, V_L and U were derived corresponding to particular PDFs. In this section the same texture measures are applied to characterise data that assumed to be L distributed. Obviously, a texture measure arising from a PDF that was close to a K distribution is expected to yield the greatest statistical accuracy.

From this point on, single-look SAR is assumed since it yields maximum resolution and retains all the texture information available to the sensor. The expected values of the texture estimators can be related to the order parameter, in the limit of large N, by evaluating appropriate moments of the K distribution. Thus,

$$\langle V_I \rangle = \frac{\langle I^2 \rangle}{\langle I \rangle^2} - 1 = 1 + \frac{2}{\nu} \tag{5.28}$$

$$\langle V_A \rangle = \frac{\langle I \rangle}{\langle A \rangle^2} - 1 = \frac{4\nu\Gamma^2(\nu)}{\pi\Gamma^2(\nu + \frac{1}{2})} - 1 \tag{5.29}$$

$$\langle V_L \rangle = \langle \ln^2 I \rangle - \langle \ln I \rangle^2 = \psi^{(1)}(\nu) + \frac{\pi^2}{6} \tag{5.30}$$

and

$$\langle U \rangle = \langle \ln I \rangle - \ln \langle I \rangle = \psi^{(0)}(\nu) - \ln \nu - \gamma_E \tag{5.31}$$

The value of ν can be estimated by inverting Eq. 5.28-5.31.

These texture measures are estimated over a window of N pixels. Approximate values for their mean and variance can be derived by performing perturbation expansions of V_P, V_A, V_L and U about their expected values. The bias is derived by taking the expectation value of these expansions. The variance is obtained by squaring the expansion before taking the expectation value. Both

bias and variance to first order in $1/N$ have been derived (Oliver 1993, Blacknell 1994). For small windows (< 200 pixels) the second-order term is also required (Lombardo and Oliver 1994).

In describing K distributed texture, the bias and variance of the estimate for ν are used rather than the measure from which it is obtained. The relation between small changes in the texture measures and the estimates for order can be derived by differentiating (5.28) to (5.31). Following the method of the section of estimating moments, the bias in the order is derived by taking ensemble averages of these differentiated expressions and substituting for the bias in the texture estimators. Similarly, the variance is derived by squaring the differentials of the expectation values before taking ensemble averages and substituting for the variance of the texture estimators. The most convenient way to present the result is in the form of relative bias and variance, denoted by $\Delta\nu/\nu$ and $\delta\nu^2/\nu^2$, respectively, where a subscript denotes the mean from which the estimate was obtained. Summarising the obtained results:

$$\frac{\langle \Delta\nu \rangle_{\nu_L}}{\nu} = \frac{\nu}{N}(1+\frac{1}{\nu})(1+\frac{6}{\nu}) \tag{5.32}$$

$$\frac{\langle \Delta\nu \rangle_{\nu_A}}{\nu} = \frac{\pi\Gamma^2(\nu+\frac{1}{2})}{4N\nu\Gamma^2(\nu)(1+2\nu(\psi^{(0)}(\nu)-\psi^{(0)}(\nu+\frac{1}{2})))} \times (\frac{12\nu\Gamma^2(\nu)}{\pi\Gamma^2(\nu+\frac{1}{2})} - 4 - \frac{3}{2\nu}) \tag{5.33}$$

$$\frac{\langle \Delta\nu \rangle_{\nu_L}}{\nu} = \frac{\psi^{(1)}(\nu)+\frac{\pi^2}{6}}{N\nu\psi^{(2)}(\nu)} \tag{5.34}$$

where $\psi^{(2)}(.)$ use the tetra gamma function and

$$\frac{\langle \Delta\nu \rangle_{U}}{\nu} = \frac{1+\frac{2}{\nu}}{2N(\nu\psi^{(1)}(\nu)-1} \tag{5.35}$$

for the relative bias in order parameter from V_P, V_A, V_L and U, respectively. The corresponding expressions for relative variance are

$$\frac{\langle \delta v^2 \rangle_{V_I}}{v^2} = \frac{v^2}{N}(1+\frac{1}{v})(1+\frac{4}{v})(1+\frac{5}{v}) \tag{5.36}$$

$$\frac{\langle \delta v^2 \rangle_{V_A}}{v^2} = \frac{1}{N(1+2v(\psi^{(0)}(v)-\psi^{(0)}(v+1/2)))^2} \times (\frac{16v\Gamma^2(v)}{\pi\Gamma^2(v+1/2)} - 5 - \frac{1}{v}) \tag{5.37}$$

$$\frac{\langle \delta v^2 \rangle_{V_L}}{v^2} = \frac{\psi^{(3)}(v) + 2\psi^{(1)^2}(v) + \frac{2\pi^2}{3}\psi^{(1)}(v) + \frac{11\pi^4}{90}}{N(v\psi^{(2)}(v))^2} \tag{5.38}$$

where $\psi^{(3)}(.)$ is the tetra gamma function, and

$$\frac{\langle \delta v^2 \rangle_{U}}{v^2} = \frac{\psi^{(1)}(v) + \frac{\pi^2}{6} - 1}{N(1-v\psi^{(1)}(v))^2} \tag{5.39}$$

The uncertainty in the estimated order parameter is greater than the bias since the latter is of order $1/N$ whereas its standard deviation is of order $1/\sqrt{N}$. It is therefore possible to ignore the effects of bias for simplicity, particularly for large N. In order to compare the performance of different measure, a plot of their predicted relatives standard deviation is shown in Figure5.1. These predictions are compared with numerical results for the exact K distribution. Some simulated results are also included (Oliver and Quegan 1998).

The first conclusion that can be drawn is that there is good agreement between theory and simulation, except for V_I with small values of order parameter where the discrepancy can be partially resolved by introducing the second-order term (Lombardo and Oliver 1994), with still higher order needed for $v \leq 0.4$.

At this step the performance of the different measures is then compared. The numerical ML calculation for the exact K distribution (Blacknell 1994), denoted by the full curve, effectively represents the envelope of the optimum performance of the approximate analytic measures. It can be seen that U is best for $v<3$, whereas V_A should yield a closer approximation to the true ML solution over the range $0.1 < v < 10$ (Jahangir el al 1996). Equation 5.24 suggests that the MLE for a K distribution should combine U and V_I rather than V_A. Joughin et al 1993 used numerical simulation to show that the variance of the estimate of v exponentially related to its mean value.

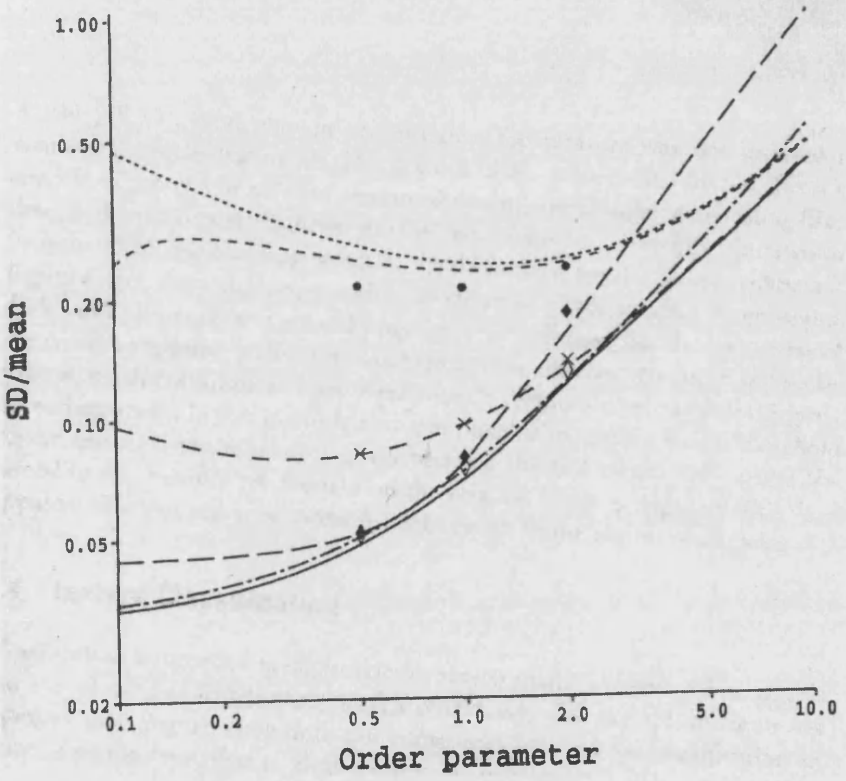

Figure 5.1 Comparison of predicted relative standard deviation in order parameter from different measures. Window 32 by 32 pixels; simulation over 10^3 samples. Exact numerical ML solution for K distribution (full). Theoretical results for approximations denoted by increasing dash length: V_I first-order theory, second-order theory and simulation (•); V_A: theory and simulation (×); V_L: theory and simulation (♦); U: theory (long and sho--rt dashes), simulation (◊)(Oliver and Quegan 1997)

In the limit of large v, the minimum variance for unbiased estimators is approximately given by Cramer-Rao bound that has the value v^2/N (Lambardo and Oliver 1994). The errors in all the measures considered here have this form, with constants of proportionally taking the value 1.0, 1.63, 11.9, and 2.58 for V_P, V_A, V_L and U, respectively. Thus, V_I is asymptotically the optimum estimator for large v where it attains the Cramer-Rao bound. However, it is the worst estimator in the opposite limit where U appears best.

For large values of v the texture fluctuations are very weak and the intensity distribution tends to the negative exponential speckle PDF for single-look imagery. Strong texture is of more interest, corresponding to smaller values of v where V_L and U provide reasonable approximations to the true MLE.

This is proposed for the main criteria for classification of the SAR data. The information from the texture analysis, data model and texture exploitation provide vital clues in classification. As it is stated previously that classification is not just for a single-pixel but it can also be for the region. Therefore, the information obtained in this section will be benefit of in the later part of object-oriented classification.

5.2.2.4 *Texture analysis for object-based classification*

The results obtained from the region-growing process came in the form of polygon of objects. Since one polygon represents one object, the statistic of all pixels in that polygon also represents the statistic of that particular object. Thus, the characteristic or statistic of all the pixels in the object is represented by one set of values or statistic parameters instead of the "per-pixel" statistic. The classification is then applied to classify between the polygons them self, not to classify between the pixels. Moreover, step-by-step classification can be applied onto the data. The classification step can always be carried out from time to time in order to classify the classes from minimum of two classes to more, unlike the "per-pixel" classification in which the classification has to be done at one time only.

From the information of texture exploitation in the previous section, the parameters for data model and from texture exploitation can be obtained. But please note that the data model described both in Chapter 2 and in the previous section are used to describe the whole scene of the image. In this research, the advantages and information from data model and texture exploitation is main sort of information to describe and classify the feature objects or polygons. Data model is then for calculation the model of the polygons not for the whole scene.

The main classification purpose in this research is to separate the buildings, trees and water bodies out of each other's. The data model then calculates PDF for each feature object in the scene independently from each other. Parameters of PDFs are therefore obtained and also type of the PDFs.

Previously stated in the Chapter 2, Valenzuela et al 1972, Warden 1970, found that lognormal distribution has been found to be appropriate for urban clutter since it represents the high value data such as the return signals from the builds very well. On the other hand, gamma distribution matches the low intensity well, such as reflection from the trees. This technique has been put to tests in this research and will be used as the main criteria for the classification. By setting the rule those feature objects, which can be better represented by log normal distribution than normal distribution, those feature objects will be classified as buildings. On the other hand, feature objects, which can be better represented by normal distribution than log normal distribution, those feature objects will be classified as trees.

The results can be found in Chapter 6 and the classification details and techniques can be found in the later section 5.3.3.

5.3 Object-based Classification

The result from feature extraction and region-growing technique comes in format of small and large group of pixels which each group represents one object. Classification is performed by looking at statistic property of each object

instead of every single pixel. The statistic property of each object is derived from statistic of intensity value in SAR intensity image of pixels in the object group.

In the later sections, a comparison between pixel-based and object-based classifications is stated. Followed main concept of object based classification as well as the classification techniques.

5.3.1 Pixel-based and Object-based classification

The pixel-based classification means the classic image classification method that classifies images according to the spectral information in the image and the classification manner is "pixel by pixel" and one pixel can only belong to one class. There are two primary types of pixel-based classification algorithms: unsupervised and supervised. Unsupervised classification algorithms cluster data according to several user-defined statistical parameters in an iterative fashion until either some percentage of pixels remain unchanged or a maximum number of iterations have been performed. This method of classification is most useful when no previous knowledge or ground truth data of an area is available. However, the classes determined by the algorithm still require land cover identification by an experienced analyst, which can be a significant disadvantage in using this method. In supervised classification, the image analyst supervises the pixel categorisation process by specifying numerical descriptions of the various land cover types present in an image. Training samples that describe the typical spectral patter of the land-cover classes are defined. Pixels in the image are compared numerically to the training samples and are labelled to the land-cover class that has similar characteristics (Tadess et al 2003).

The object-based classification concept is that important semantic information necessary interpret an image is not represented in a single pixel, but in meaningful image objects and their mutual relationship (Baatz et al 2001). The first step of the process is to generate image objects or segments, which is done by the feature extraction process in chapter 4. The image objects are classified by

using information representing those objects. The main rule or criteria for classification is from the section 5.2.1.

Two most evident differences between pixel-based image classification and object-based classification are:

1. In object-based classification, the basic processing unit are image objects not single pixel.
2. Object-based classification uses soft classifiers that are based on fuzzy logic not hard classifiers.

Pixel-based approach is based on conventional statistical techniques, such as parallelepiped, maximum likelihood and minimum distance procedures. The classic classification approach classifies an image pixel be pixel at one time for the whole image. While the object-based classification, the objects are classified step by step by a fuzzy rule which can be single condition or consisted of combination of conditions (Baatz et al 2001).

Since remote sensing application community is interested in image resolutions that will help them observe and monitor their specific objects of interest. The increasing resolution and the physical properties of objects in the images with a geometrical resolution of 5 meter or less leads to very complex spectral analysis (Kok et al 1999). The mixed pixel problem and the increasing difficulties in the spectral analysis of high resolution images make it necessary to develop a method of object-based classification. The object-based classification helps in reducing the large number of units to be handled in the processing. Moreover, the object-based technique can cope with the noisy SAR images.

Though, there are major drawbacks of the object-based classification. The first one is that the image segmentation or feature extraction is the first step and is very important. The inaccurate result from feature extraction can leads to the very poor result of classification. The second problem is discrepancy. Discrepancy was created because in object-based classification, objects are used as classification units and this classification may lose some detailed information if compared with the pixel-based approach with single pixel as classification unit (Baatz et al 2001).

These aspect might explain why the approach of object-based image analysis has an enormous potential and leads to better classification results quantitatively in terms of classification accuracy as well as in a qualitative sense, new classes to tasks can be addressed. With an object-oriented approach a semantically better structured, more detailed and more local analysis becomes possible with all the resulting consequences for the automated understanding and the utilisation of geographical data.

5.3.2 Basic concepts and classification

Classification is intended to determine the closet match between a data sample and a set of samples representing the different classes. Classification can also be used to discriminate between regions having the same form of PDF. In this section, a method based on fitting texture parameters with one in which a hypothesis test is applied directly to the data is compared. In this research, the intention of classification is to separate building, trees and water bodies from one another. And since the data set resolution is 5m, the individual building or tree might not be able to detected or classified. But blocks of buildings or groups of trees, which present well in the data, are the main target to be classified.

5.3.2.1 Classified by fitting

In this approach each texture sample is represented by an estimated order parameter, obtained by fitting. These estimates are compared with reference values and the sample assigned to a class. This process can be optimised if the $P(v)$ is known, then it would be possible to calculate the log likelihood of a sample belonging to each class.

5.3.2.2 Direct classification

There are many occasions when determining estimator values as part of the classification process is not required. For example, the K-S test, introduced in the section 5.2.1, provides a non-parametric method that classifies the data directly. If the form of the distribution is known, it is better to test directly whether the data is consistent with the candidate PDFs. Oliver and Quegan 1998 compared numerical evaluation of the log likelihood for the exact K- distribution with analytical results for the approximate gamma and log PDFs and it could be said that approximate forms of PDF lead to a slight reduction in the probability of correct classification. The K-S test, which is not matched to the form of the data PDF, yields significantly poorer classification, as expected. This again reinforces the importance of using any information available in exploitation image data. It is better to use any one of these theoretical forms for the PDF than to be noncommittal. Since most data can be represented within the span of possible distributions, one of the approximations can be applied for all data without significant degradation. And Oliver and Quegan 1998 also suggested that the direct method, which is based on log likelihood or K-S test, is more reliable than fitting, since one can always identify the closet class, whereas fitting procedures are not very robust.

In this research, the form of PDFs for classification is known. From the researches in the past (Oliver and Quegan 1998, Valenzuela et al 1972, Warden 1970) and also some investigations in this research, which the results posted in the Chapter 6, it has been found that log normal distribution is the most suitable for describing the feature objects of building and normal distribution is the most suitable for describing the feature objects of trees. The water body, from the data set used in this research, can be described by a uniform value.

The classification therefore means to find the best fit from those 2 PDFs for the feature objects. The fitting classification method is used because the distribution functions are known and could yield more accurate results than direct classification without any prior knowledge. Figure 5.2 a) shows the original histogram of lognormal distribution and b) shows the histogram

distribution of the building object and Figure 5.3 a) shows the original histogram of normal distribution and b) shows the histogram distribution of the tree object.

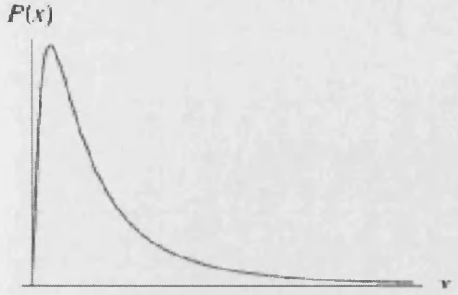

Figure 5.2 a) The shape of the lognormal distribution

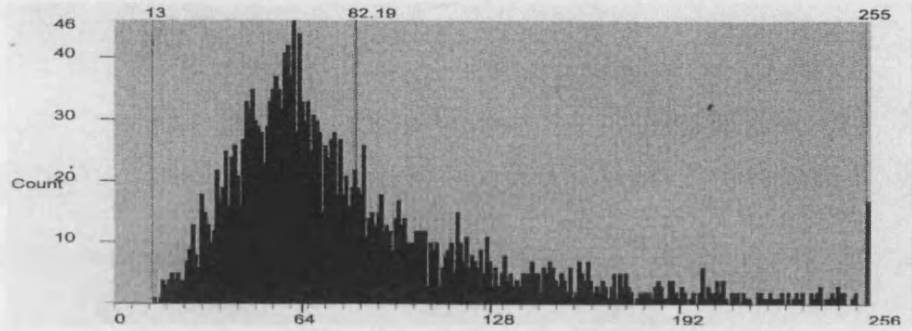

Figure 5.2 b) A pixel distribution of feature object classified as building.

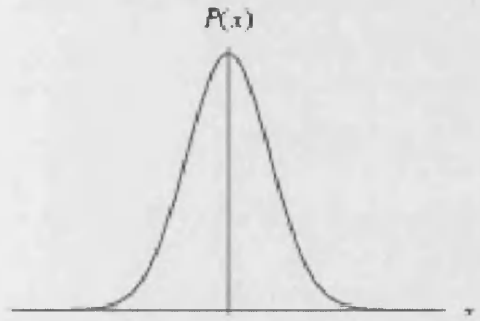

Figure 5.3 a) The shape of normal distribution

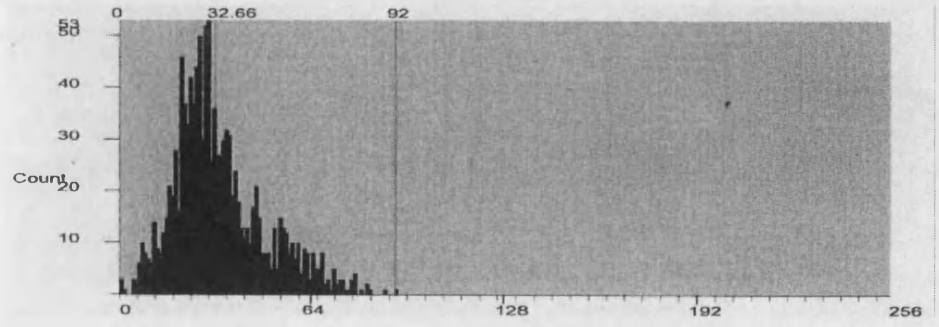

Figure 5.3 b) A pixel distribution of feature object classified as tree.

After the classification there still might be some incorrect classification as a results from the previous region splitting/merging in the process of region growing. Since the land cover in urban area is complex, some small polygons or sub objects, which were merged together to form big polygons or super objects could be incorrectly putted in together. This therefore yields inaccurate results of the classification. Some techniques have been invented to deal with these types of problem. The following techniques are the samples of the invented techniques to deal with those types of problems

5.3.2.3 Classification-based fusion

The principle of classification-based fusion developed by the author is simple: All adjacent image objects that represent identical structures or are parts of identical structures or have identical statistics, are merged into new image object. This way, a number of image objects forming an urban area can be merged into one image object representing entire urban area. The example in Figure 5.4 a) is feature objects right after the classification and in Figure 5.4 b) is feature object after classification-based fusion.

In principle, this technique is the same as region merging but the technique is region growing based on objects. The statistic parameters used for merging these sub objects are from section 4.5.3 region merging using moment and also applied to the later techniques. By comparing the covariance between these sub-objects, a decision can be made whether these sub-objects should be merged together.

Figure 5.4 a) Feature objects after classification.

Figure 5.4 b) Feature objects after classification-based fusion.

5.3.2.4 Classification-based border optimisation

The main purpose of this technique is the shape correction of image object based on sub objects. The basic principle is that a sub object, which was assigned to a class in another group other than the class of its super object, is treated as "heterogeneous" or "not belonging" to this super object. Sub objects situated at the border of their respective super object and member of another group will be re-grouped to become sub object of a neighbour super object, provided that this neighbour super object is of the same statistic structure group as the sub object. The result of such border optimisation appears in Figure 5.5. The image represented by the affected super object alters: whereas the former super object loses the area represented by the re-grouped sub object, the new super object gains this area.

In this case, a main clue for decision of "belong" or "not belong" to the super object is by comparing the covariance between the neighbour super object and the suspected sub-object using technique from section 4.5.3.

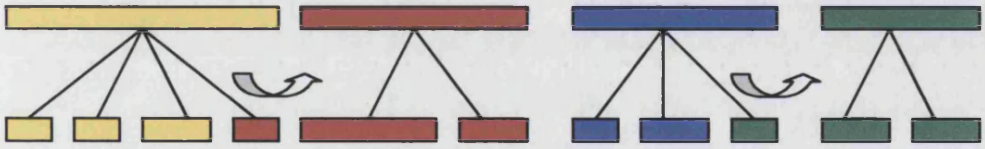

Figure 5.5 a) Feature object before border optimisation process

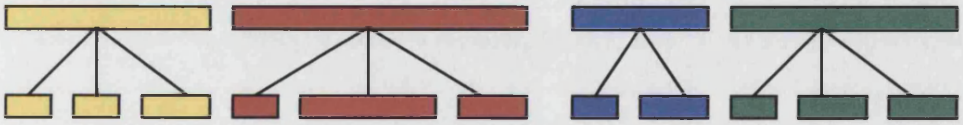

Figure 5.5 b) Feature objects after border optimisation process

5.3.2.5 Classification-based image object extraction

The technique above does not benefit for classification in the case that there is another sub object actually in the group of super object. For example, there can be a tree inside a building block or vice versa, a small building inside the group of tree. *A classification-based image object extraction* is needed. In contrast with border optimisation, the extraction of sub objects handles all sub objects, even image objects situated geographically within a super object. If a

sub object is assigned to a different group than its super object, the connection between these two objects will be de-allocated. The super object "loses" the area represented by the sub object. Instead, a new image object identical to the sub object will be produced and inserted in the network as its new super object. Figure 5.6 a) shows the example of feature objects containing wrong sub objects. And Figure 5.6 b) shows the feature objects after classification-based image object extraction process.

This is a continued case from the classification-based border optimisation. From a calculation of covariance of a suspected sub-object and 2 super objects, the sub-object cannot be merged with either super object, the sub-object is then assigned super object.

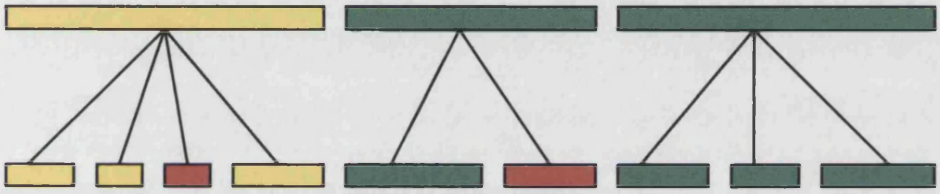

Figure 5.6 a) Feature objects containing wrong sub objects

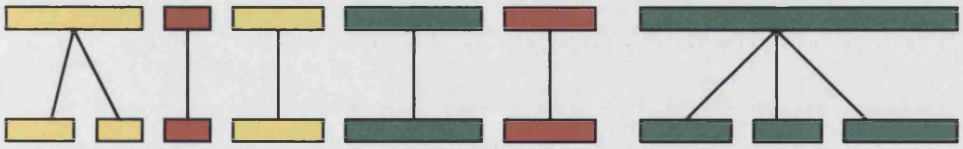

Figure 5.6 b) feature objects after classification-based image object extraction process

5.4 Conclusion

The main concept of object-oriented classification has been introduced as well as the texture exploitation for classification and also classification techniques. It is important to consider the kinds of application and data types of which texture measures would be relevant. In exploiting RCS information, the value of RCS has direct physical significance. However, the connection between the value of a texture measure and a physical property of the scene is ambiguous. Clearly, texture describes the depth of fluctuation, which depends on both

physical RCS and spatial relationships between objects in the scene. Thus, discriminating between regions of different texture is allowed to distinguish between different scene categories. A texture measure can be used either to classify into region of different textures, which either depend on a prior reference data base or maybe learned from the data or in this case, in the segmentation process (region growing). The former approach identifies a texture sample with the nearest member of a reference set, while the later provides data-driven separation into an unknown number or regions or in this case polygons.

But since urban areas are complicated, some comprehensive approaches are needed and different additional techniques have to be investigated to cope with different types of urban area and to different types of cities.

The results of the classification process, along with other processes in this research, and also the analysis of the results are stated in Chapter 6.

Chapter VI

Application over and area of west London

6.1 Introduction

Chapter 4 and Chapter 5 have shown the whole process for mapping an airborne SAR/IfSAR data in urban areas. Feature extraction process is stated in Chapter 4 and object-oriented feature classification is in Chapter 5. The results for all processes in those previous chapters are illustrated in this chapter. Beginning with description of the dataset and followed by the results. The results are shown in a running order as seen in the flow chart in Chapter 4. This is to provide an easier view to the whole process. The analysis of the results is stated before the conclusion of the chapter.

6.2 Data Set

The SAR data used in this project are from STAR-3I system. The STAR-3I consists of two X-band antennas mounted on the wings of LearJet36. Data collection from the two antennae occurs simultaneously. The set of acquired data is 'interfered' by a digital correlation process to extract terrain height data, which are used to geometrically correct the radar image. STAR-3I uses post-processed Differential Global Positioning System (DGPS) data, together with on-board laser-based inertial measurement data, to attain highly accurate positioning and a little control. Precise terrain height and positioning data are enhanced by calibration of the baseline (the distance between the two antennae for interferometric calculation). There are two operating altitude of the system. In the Table2.1, some parameters and characteristics of the two operating altitudes are listed (Mercer and Gill 1998).

Parameter	Operating Altitude	
	40,000ft	20,000ft
Operational Speed	750 km/h	750km/h
Depression Angle(nom)	33-55 deg.	33-55 deg.
Swath Width(ground plane)	10 km	5 km
Nominal Resolution	3 m	3 m
Pixel Spacing	2.5 m	2.5 m
IfSAR DEM sample Spacing	2.5,5,10 m	2.5,5,10 m

Table 6.1 Parameters of the STAR-3I system (Mercer and Gill 1998).

The data used in this project was collected from the 20,000 ft operating altitude with the intermediate viewing angle of 45 degree. The image is 700x1130 pixels with 5-metre pixel resolution. From the system specification, the system is capable of imaging 30,000 km^2 in a single operational day. And at the lower altitudes, the signal-to-noise ratio is larger and thus the height noise is lower, thereby improving relative accuracy, however, swath width is reduced as it can be compared between the 40,000 ft and 20,000 ft operating altitude specifications. The absolute accuracy claimed by the Intermap Technology, the owner of the system, the DEM is around 1.5-5 meter (Mercer 1998, Mercer and Gill 1998).

The data set was taken over West London around Chiswick and Kew garden area. The area contains river, park, open space, residential buildings, roads, rail tracks and etc. It is a mixed urban area. Figure 6.1 a) shows the SAR intensity image of the area b) shows the IfSAR DEM of the area and c) shows the aerial photographer of the area.

Figure 6.1 a) SAR intensity of the area of West London around Chiswick and Kew Garden area

Figure 6.1 b) IfSAR DEM of the area of West London around Chiswick and Kew Garden area

Figure 6.1 c) Aerial photographer of area of West London around Chiswick and Kew Garden area

6.3 Results

In this section, all of the results from the whole processes from Chapter IV and V are put together. The results from edge detection are in the first part of this section. Then the step-by-step results of generation of bald earth DEM are followed. The region growing from edge detection results and results from classification are the last 2 in this section.

6.3.1 Edge detection

The edge detection used in this research is adopted from the Canny edge detection technique. The technique consists for several step of processing as described in Chapter 4. By using the constrained gradient as the main criteria, the results of the edge detection are not only edges but also corner points as well. As stated in Chapter 4, the edge detection technique would detect edge as long as

there are, in the nearest neighbourhoods, 2 gradient vectors pointing in opposite directions, at each side of the current pixel. And the corner points can be detected by the changes in directions of those 2 gradient vectors. Figure 6.2 displays the result obtained from the process. And in Figure 6.3, the relationships between the original image and detected edges are shown. Edges of features are well represented in the edge image.

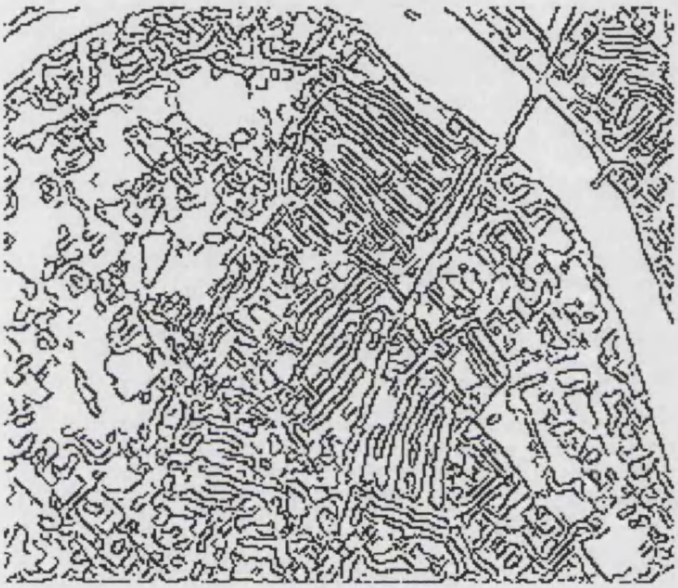

Figure 6.2 The Edge image as a result from Edge detection technique

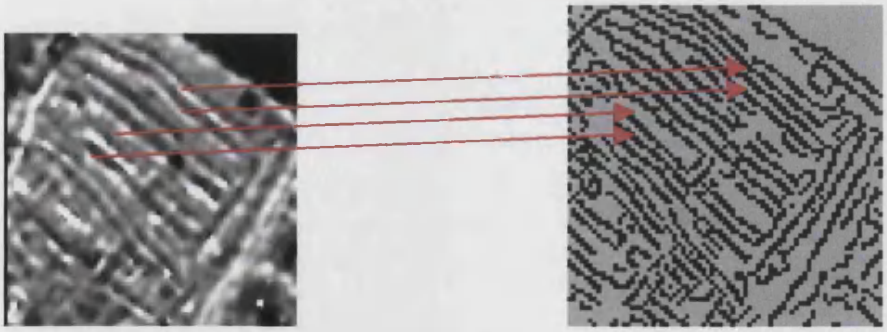

Figure 6.3 The images show the relation between the original image and the detected edge

6.3.2 Generation of bald earth DEM

The concepts and techniques of the generation of bald earth DEM process, as previously described in Chapter 4, use the technique of image pyramid and hierarchical images interpolation techniques. At the first step, the IfSAR DEM is re-sampled by different size of minimum filters for example, 3x3, 5x5, 9x9, 12x12, etc. Each re-sampling result is then assigned as the starting image for each level of interpolation. Figure 6.4 a) displays the starting level for surface from 3x3 minimum resampling DEM b) displays the starting level for surface from 7X7 minimum resampling DEM and c) displays the starting level for surface from 9x9 minimum resampling DEM.

These 3 images along with additional information obtained from variance and slope, shown in figure 6.5, from the original DEM were used in the process of generation of bald earth DEM. The variance and slope are used as additional information in order to obtain the ground points not points on the top of the features and not points on the side of the features.

From the selection criteria set in Chapter 4, surface points at each level were selected. At the bottom level, 3x3 resampling surface, a total of 6360 points were selected. 6358 points were selected from 7x7 resampling surface and 5345 points from the 12x12 resampling surface as shown in Figure 6.6 a) b) c), respectively.

Figure 6.4 a) The starting level for surface from 3x3 minimum resampling DEM

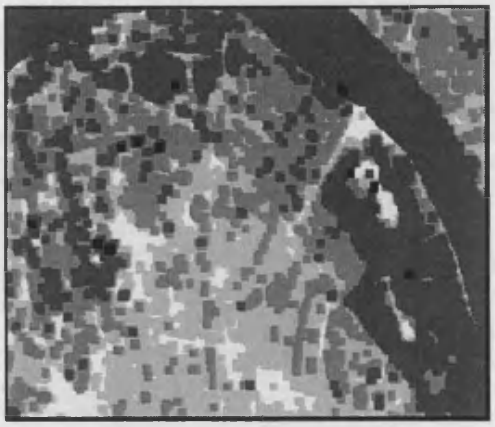

Figure 6.4 b) The starting level for surface from 7x7 minimum resampling DEM

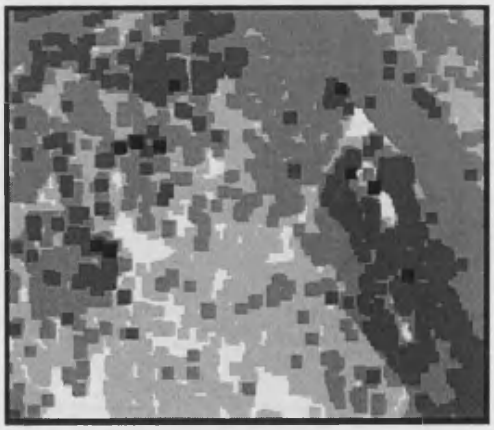

Figure 6.4 c) The starting level for surface from 9x9 minimum resampling DEM

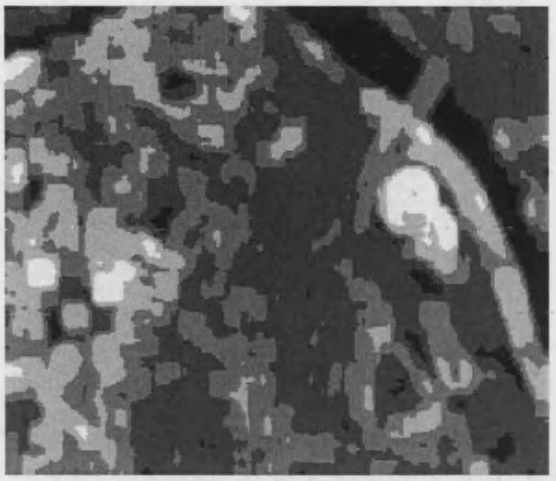

Figure 6.5 a) The Variance of original IfSAR DEM

Figure 6.5 b) The slope image of original IfSAR DEM

Figure 6.6 a) Selected surface points from resampling level of 3x3

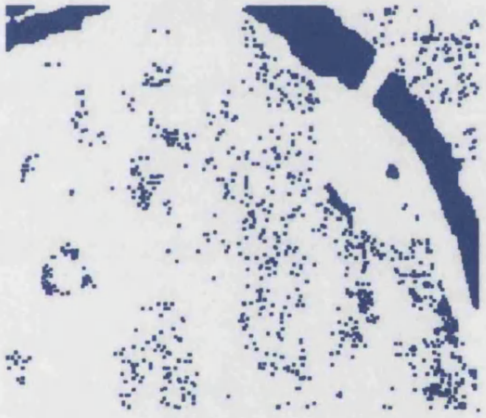

Figure 6.6 b) Selected surface points from resampling level of 7x7

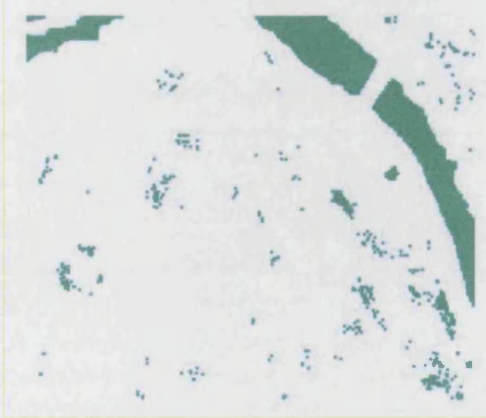

Figure 6.6c) Selected surface points from resampling level of 12x12

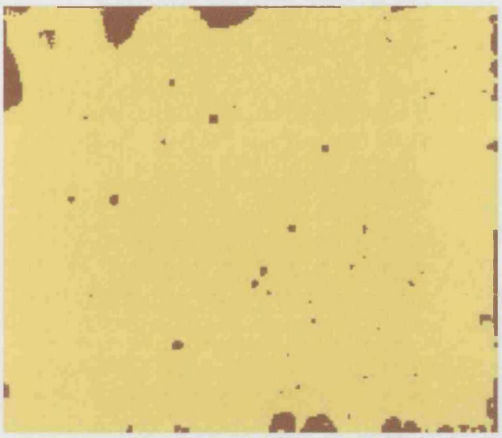

Figure 6.7 Selected point from inter-level surface checking to be used for generate final bald Earth DEM

These points in each level were used to generate a surface. The differences between surfaces were then checked as well as the checked between generated surfaces and the original DEM. Points, in which the differences between surfaces were more than the setting value, would be eliminated. Points, in which the differences were within the value limit, would be used for generation of bald earth DEM. This is to prevent some points which are not the true ground points but as the result of the resampling, become ground points. Figure 6.7 shows the remaining points for generation of bald earth DEM.

The generation of bald earth DEM technique then applied as described in Chapter 4. The bald earth DEM results can be seen in Figure 6.8 a) and the OS DTM is shown in Figure 6.8 b). As clearly shown in the Figure 6.8 a) and b), there are differences between the generated bald earth DEM and the OS DTM. The OS DTM is very smooth compared to the noisy generated DEM. This is believed to be the result of ground points selection and interpolation processes. An accuracy assessment of the generated bald earth DEM is shown in section 6.4.1.

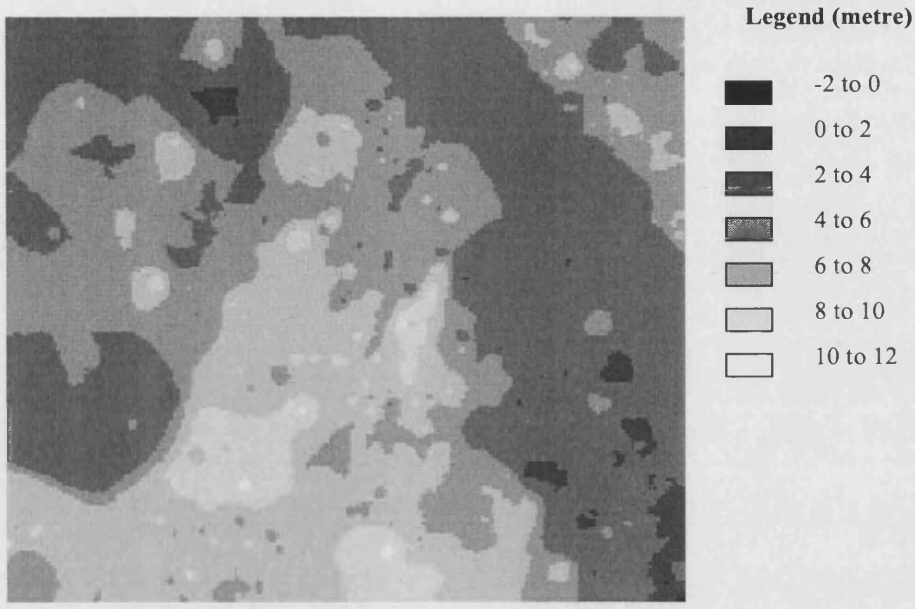

Figure 6.8 a) The Generated Bald Earth DEM

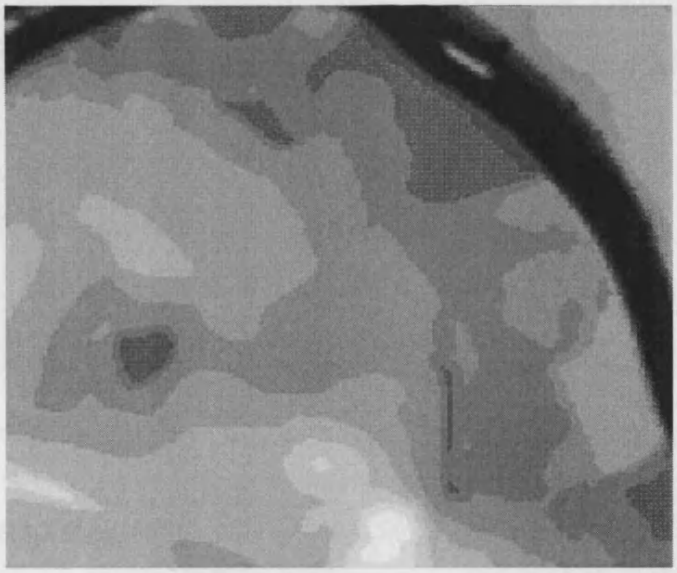

Figure 6.8 b) The Ordnance Survey DTM.

The next process is to create a " feature surface", in which only features would appear on the surface of the DEM It can be done by subtracting the original IfSAR DEM with the generated bald earth DEM. But since the IfSAR

DEM is very noisy, some of the ground points might be left on the feature surface as well. In order to get only the features, the next process of region growing from edges is needed. Feature surface image is shown in Figure 6.9 a) and the original IfSAR DEM is shown in Figure 6.9 b)

Figure 6.9 a) The result of subtracting IfSAR DEM with generated bald earth DEM, so called "Feature surface"

Figure 6.9 b) The original IfSAR DEM.

6.3.3 Region growing from edge detection

From the feature surface, the points on the surface should represent only the height of the features, but there might be some points which represent ground points left in the surface. This might be because of many factors such as accuracy of the generated bald earth DEM, in which described in the section 6.4, the noisy

IfSAR DEM itself which makes the accurate bald earth DEM very difficult. Nevertheless, the regions growing process could over come the problem, by perform the region growing from the edges of the features, the regions obtained from the process would include only pixels represent features. And this process also over come the problem of very small detected edges, which might be detected because of the noisy SAR intensity image. Having edges as seeding points, if there is no feature on the feature surface, those tiny edges will not provide any region from the process and those edges are eliminated automatically.

By overlaying the edges over the feature surface, the region growing process can begun using edges as seeding point. Figure 6.10 shows feature surface overlaid by the edges. The algorithms for the region growing process have been described in Chapter 4.

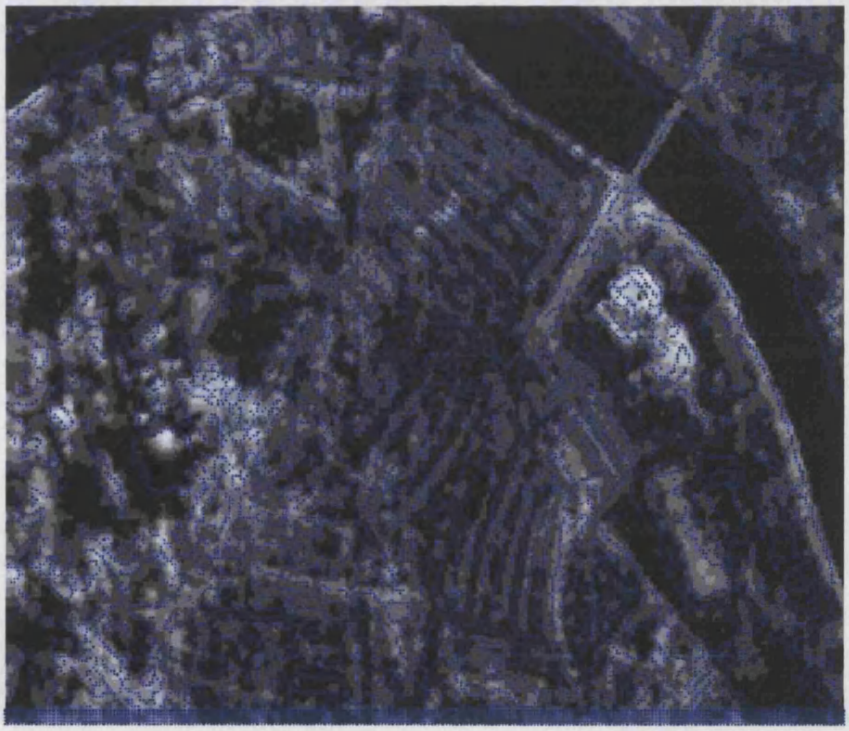

Figure 6.10 The feature surface overlaid by detected edges, which used as seeding point for region growing process.

The results of region growing can be seen in Figure 6.11. It's clearly shown in the result image that even though there are many edges detected, but not all of them represent edges of features on the scene. This is also the automatic screening system of the accuracy of the edge detection. The edge that cannot provide any region bigger than itself is eliminated at this stage. There might really be a feature but it is too small to be included in the feature surface or the edges might just be results of the noisy SAR intensity image.

Figure 6.11 The result of the process of region growing from edge detection

6.3.4 Classification

Having introduced the object-oriented classification technique and classification method in chapter 5, each feature object from the result of region growing process is thus classified by looking at its distribution parameters. Listed in Table 6.2 are parameters of distribution functions of 30 classified objects. The parameters in Table 6.2.which are Mean and Standard Deviation, are the results from the classification. These Mean and Standard Deviation are the most suitable for each object.

Object No.	Mean	Standard Deviation	Classified As
1	4.264	0.416	B
2	30525	0.301	T
3	4.050	0.313	B
4	3.612	0.278	B
5	3.917	0.292	B
6	3.596	0.573	T
7	3.065	0.097	T
8	3.913	0.369	B
9	3.636	0.323	T
10	3.57	0.406	T
11	3.829	0.543	B
12	3.684	0.312	T
13	4.414	0.511	B
14	3.742	0.300	B
15	4.024	0.352	B
16	3.740	0.656	B
17	3.481	0.315	T
18	3.529	0.431	T
19	3.695	0.345	T
20	4.012	0.394	B
21	40142	0.231	B
22	4.147	0.327	B
23	3.867	0.186	B
24	3.756	0.286	B
25	3.886	0.503	T
26	4.275	0.396	B
27	4.272	0.369	B
28	3.692	0.357	T
29	4.145	0.438	B

Table 6.2 The parameters of the classified objects from object-oriented classification technique.

B in Table 6.2 refers to Building and **T** refers to Tree. Mean and Standard Deviation of the feature classified as Tree are the best fit Mean and Standard Deviation of the Gamma Distribution for particular feature. On the other hand, Mean and Standard Deviation of the feature classified as building are the best fit Mean and Standard Deviation of the Log-normal Distribution for the particular feature.

From the samples in Table 6.2, the technique is then applied to the whole data set. The results from the classification are shown in Figure 6.12. Figure 6.12

a) shows the feature objects classified as Building and Figure 6.12 b) shows the feature objects classified as Tree and Figure 6.12 c) shows the merged image of the building and tree features.

Figure 6.12 a) Image of the features that classified as building.

Figure 6.12 b) Image of features that classified as tree.

Figure 6.12 c) The merged image between the building and tree features.

From the results, the classification provides a satisfactory result. But still there are some clearly noticeable errors in the classification such as the missing big building and incorrectly classifications. Assessments of the classification results as well as results from other processes are described in section 6.4.

From the beginning of the process of edge detection to the final part of the classification, the final product can be produced. By overlaying the classified feature surface over the bald earth DEM, the 3D city model can be obtained. In the Figure 6.13a), the blue features are classified as building and green features are classified as tree area Figure 6.13b) is aerial photograph for comparison. Figure 6.14 shows the fly-over view of the 3d city model looking toward the Kew Garden. And Figure 6.15 shows the fly-over view of the 3D city model looking toward buildings south of the National Record Office building.

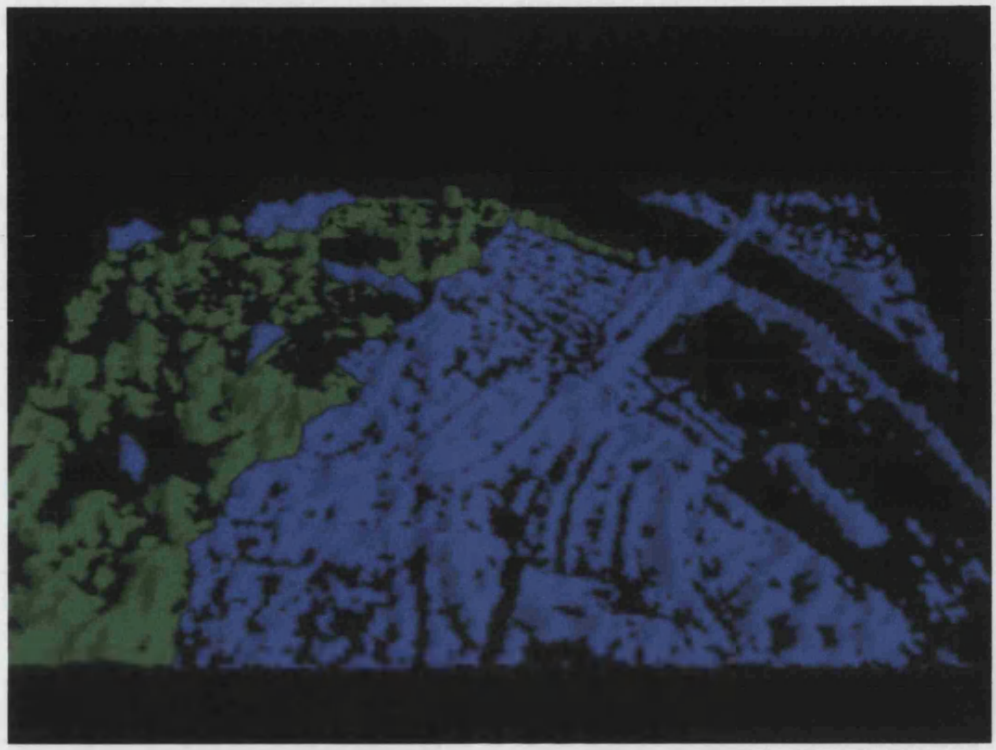

Figure 6.13 a)The 3D city of the data set. Blue represents features classified as buildings and green Represents features classified as trees.

Figure 6.13 b) Aerial photograph of the area.

Figure 6.14 The perspective view of the 3d city model looking toward the Kew Garden

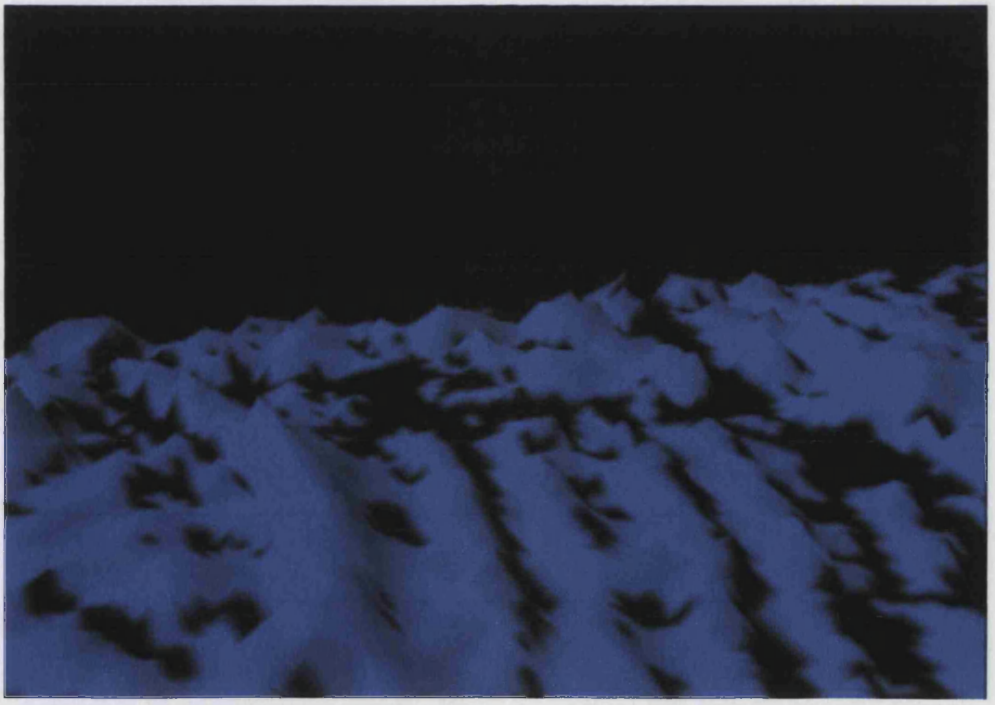

Figure 6.15 The perspective view of the 3D city model looking toward buildings south of the National Record Office building.

6.4 Accuracy Assessment

Even though, the whole process provides a satisfactory level of result. The results need to be assessed in both quantity and quality. In this section, the results from generation of bald earth DEM and Classification are analysed. By using the reference from OS Land-from-profile® DTM, the accuracy of the generated bald earth DEM can be assessed. And By using the colour aerial photography and OS Land-Line Map®, the assessment of feature extraction and classification can be analysed. At the end of this section, the whole process is applied on another data set for assessment and analysis.

6.4.1 Accuracy assessment of generated bald earth DEM

In order to assess the accuracy of the generated bald earth DEM, the OS Land-from-Profile DTM is used as reference. The generated bald earth DEM is then compared with the DTM. The average difference between the generated bald earth DEM from IfSAR DEM and the OS DTM is 0.658m with standard deviation of 1.872m. In the area of Kew garden, the average difference is 1.8m with 3.872m of standard deviation and the average of 0.415m and 1.035m standard deviation in the build-up area. The details of the statistics of the comparison can be seen in Table 6.3.

Area	Mean (m)	Standard Deviation
Whole Area	0.658	1.872
Kew Garden	1.8	3.872
Build-up	0.415	1.035

Table 6.3 The Statistic of the differences between the generated bald earth DEM and reference OS DTM.

The accuracy of the generated bald earth DEM compared with the OS DTM is in a very satisfactory level. The accuracy of the generated DEM is less than 1m, compared with the claimed accuracy of the original IfSAR DEM of 1-2m. From Table 6.3, it can be noticed that accuracy of the generated bald earth DEM in the Kew garden area is lower than in the near by buildings areas. This is

suspected that nature of the area, which consists of many features with mixed heights. The nature of the area could probably affect on the detection of ground point in the generation of bald earth DEM.

Not only the area of the Kew garden that provide less accurate bald earth DEM, but also in the area of the Public Records Office. Since the technique of generation of bald earth DEM and feature extraction technique, together, can detect only the feature that provides height. Feature, which its height is very low or no height at all, cannot be detected. There are many objects of this type of feature around the Public Records Office. This is believed to cause the less accurate area in the generated bald earth DEM.

6.4.2 Accuracy assessment of feature extraction and classification

With the limitations of SAR/IfSAR capabilities, there are levels of feature that can be extracted. The assessment of the feature extraction is done by comparing the extracted features with the OS Land Line® map. By counting the extracted features, which can get along and cannot get along with the features on OS Land Line map, the accuracy of feature extraction can be assessed. But this method of assessment cannot assess the accuracy of extracted trees. Because there is no tree presented on the OS Land Line map. Figure 6.16 displays the overlay image of the OS Land Line map over the feature surface for a) for the residential area and b) for big building area. From the assessment of the overlay image, it is obtained that there are 265 features extracted accurately according to the OS Land Line map. And there are 23 features extracted but these features are not presented on the OS Land Line map. Nevertheless, it cannot be said that those features, which are not presented on the OS Land Line map are incorrectly extracted. These features might be built up later after the production of the OS Land Line map. And this could lead to " change detection" or the process of " map updating". For more accurate assessment, the up-to-date reference or field investigation are needed. However, from the reference it can be assessed that the accurate of feature extraction of the technique is around 92%.

Figure 6.16 a) Overlay image of feature surface and OS Land-Line® map in residential area.

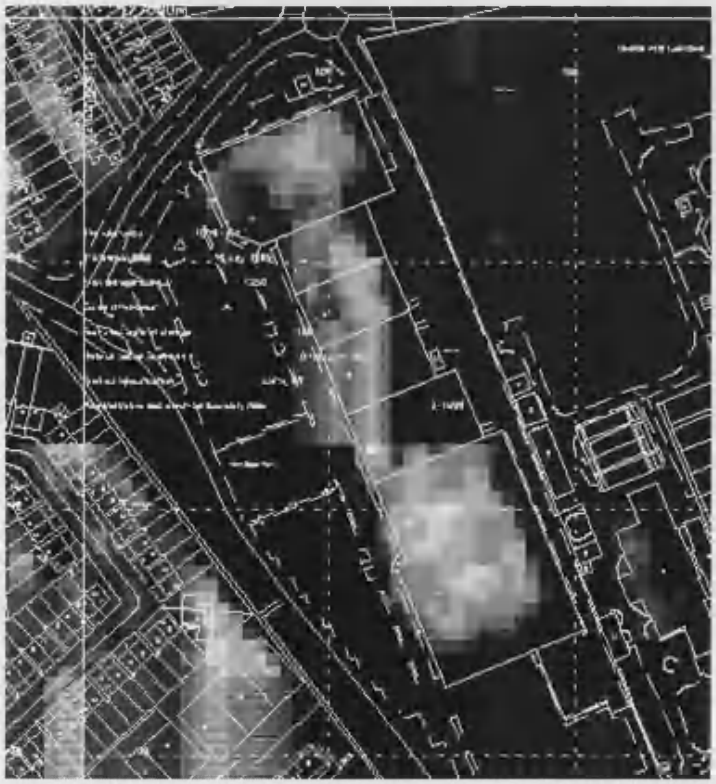

Figure 6.6 b) Overlay image of feature surface and OS Land-Line® map of big building.

Figure 6.17 a) Aerial Photograph of the test area. The red squares marks 2 major classification errors

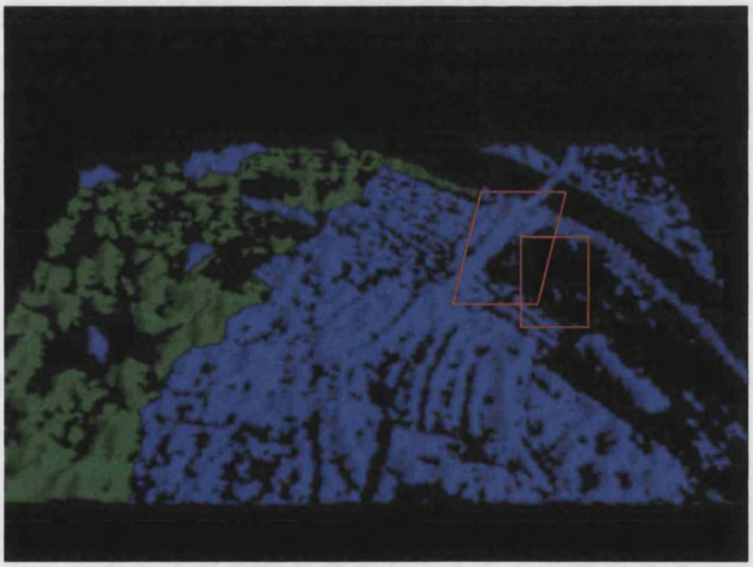

Figure 6.17 b) Classified 3D image of the test area. The red squares marks 2 major classification errors.

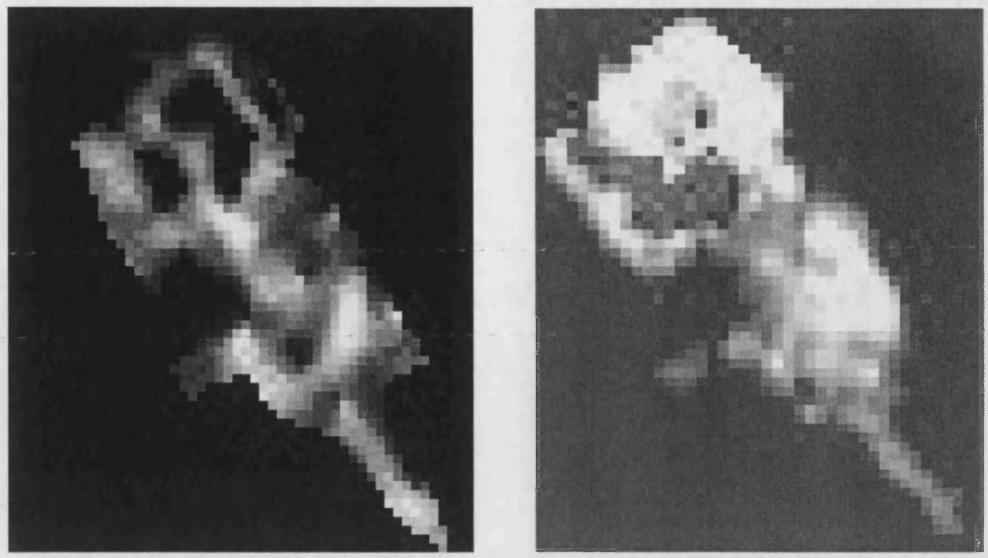

Figure 6.18 The intensity image and Feature object of the big building of National Record Office.

For the second major mis-classification is the tree-covered underground tracks runs closed to the National Record Office. The height of the features is from trees canopy but the intensity is from the reflection of the tracks, which is stronger than the reflection from trees. Figure 6.19 shows the images of underground rail tracks from aerial photograph, IfSAR DEM and from SAR intensity image. This is a classic example of occlusion in SAR image. Within the 5m footprint of SAR system, there are trees and underground rail track. Since the rail tracks are small comparing the tree cover, most of the return signals are from the trees, which later used to generate the IfSAR DEM. But the signal returns from the tracks are very strong, so the strong signal also presents in the intensity image. This occlusion caused a major problem in classification. The smaller resolution would reduce the limitation of SAR/IfSAR feature extraction and classification.

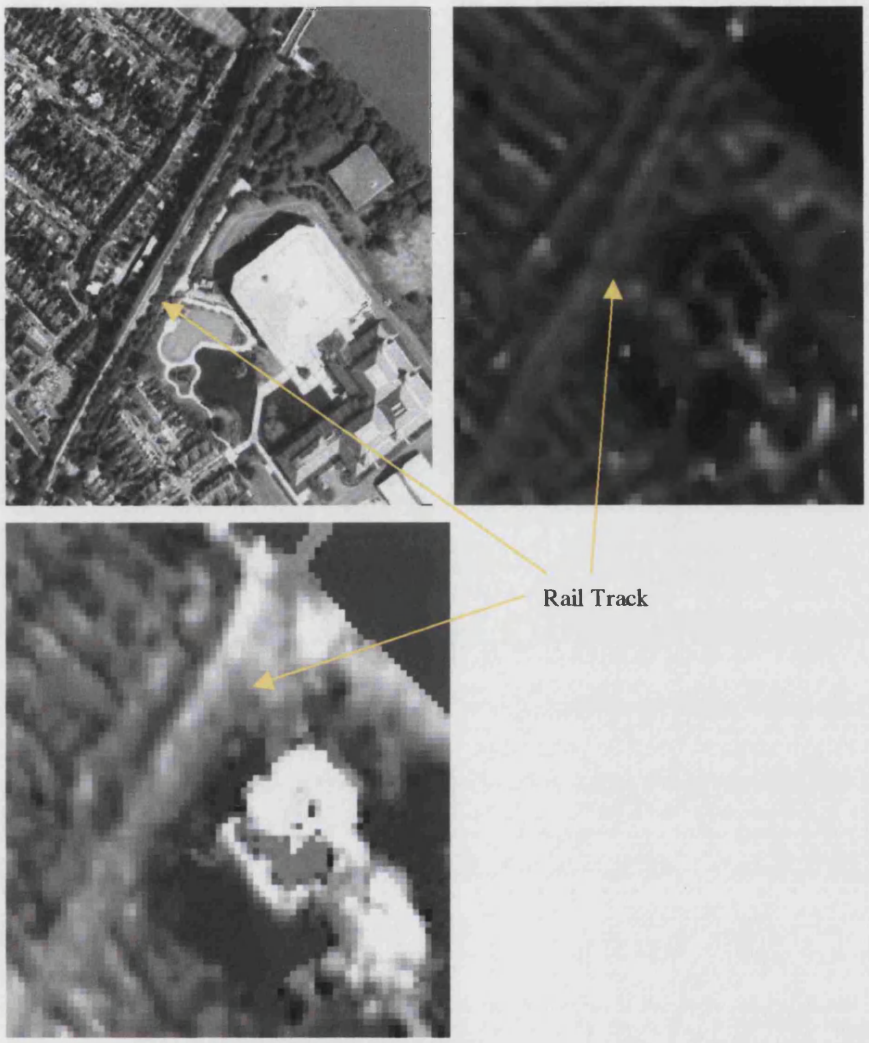

Figure 6.19 a) Aerial photograph of underground rail track b) Intensity image c) IfSAR DEM

6.4.3 Applying the technique on the different data set

To further assess the technique, the whole process is applied on another data set. The 2nd data set is still from Intermap STAR-3i system, which covers area of Shewbury. The area is a suburban area, consists of buildings, tree, open areas and a river. Figure 6.20 shows the SAR intensity image and IfSAR DEM of the area.

Figure 6.20 a) SAR intensity image of Shrewbury area.

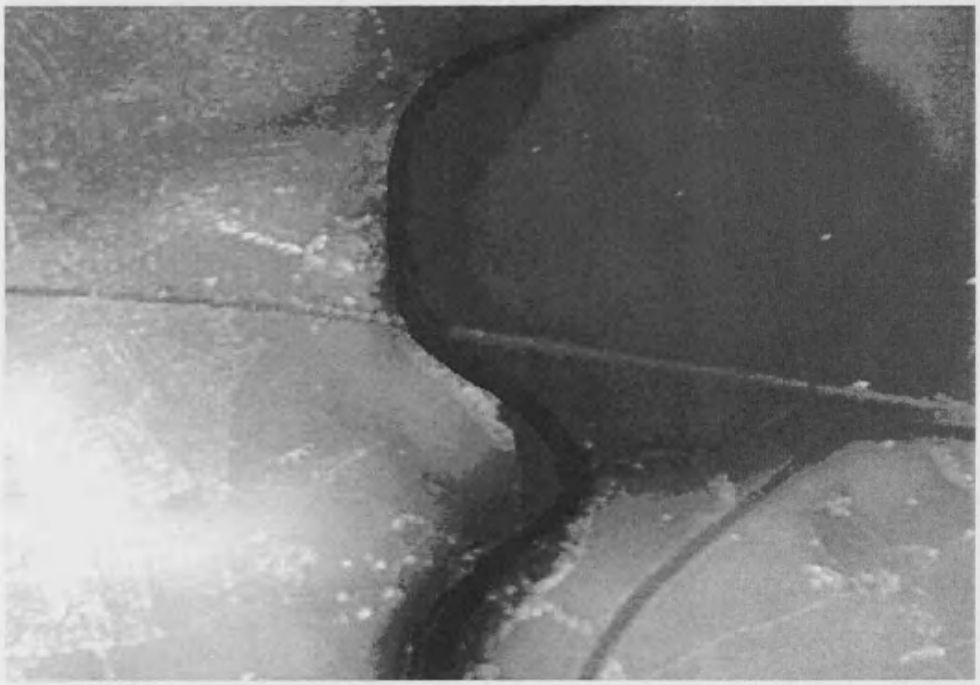

Figure 6.20 b) IfSAR DEM of Shrewbury area.

The process begins with the generation of bald earth DEM. Figure 6.21 shows the generated bald earth DEM of the area. Table 6.4 shows the statistic of

the accuracy of the generated bald earth DEM compared with the bald earth DEM generated by Intermap. Box-like pattern that occurred in the bald earth DEM Figure 6.21 is an error from interpolation process.

Figure 6.21 Generated bald earth DEM of Shrewbury area.

Area	Mean (m)	Standard Deviation
Whole area	0.273	2.752
Building area	0.173	0.714
Open area	0.184	0.284

Table 6.4 The statistic of the comparison between generated bald earth DEM and generated bald earth DEM by Intermap.

The process after the generation of bald earth DEM is calculation of normalise DSM. And the region growing from edge detection can be performed. The results of both processing can be seen in Figure 6.22 and Figure 6.23 respectively.

Figure 6.22 The normalised DSM as the result of subtracting IfSAR DEM by the generated bald earth DEM.

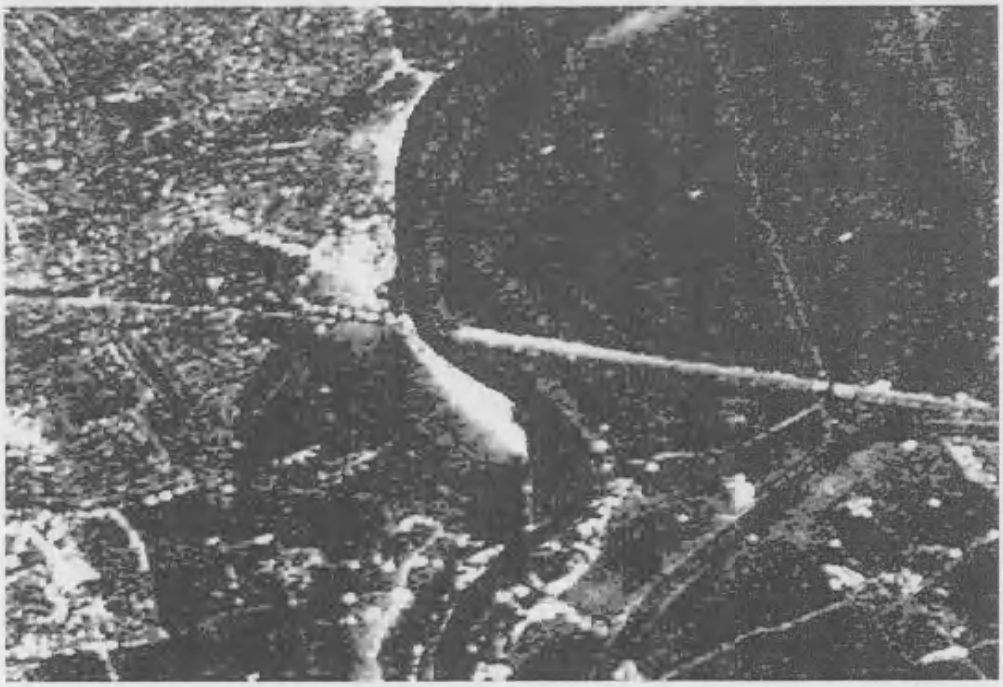

Figure 6.23 The Feature surface as the result of region growing from edge detection process.

The classification of the feature by object-oriented classification technique is applied. But from the feature surface, there are many small features presented, and features are not clearly shaped. The result of the process can just only classify the features but cannot get the accurate shape of features. Figure 6.24 shows the classified 3D-city model of the area.

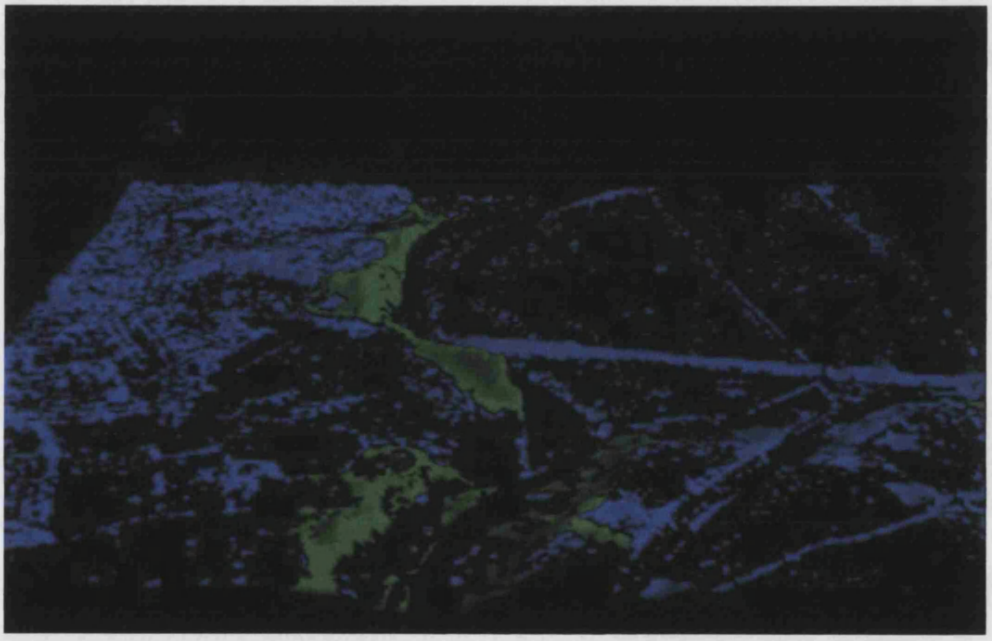

Figure 6.24 Classified 3D city model of Shrewbury area after the process. The blue represents built-up feature. And the green represents tree features.

There are major errors from classification in this data set. The result from the classification is very poor. There are some trees, which locate closed to the building, are classified as buildings. A major problem of the result is that the accurate shape of feature cannot be obtained. It is believed to be effects from occlusion and nature of the area, in which there are many small buildings spread in the image. Unlike the Chiswick area, in which there are not many small buildings.

6.5 Conclusion

The results of the whole processing have been shown and analysed. Even thought there are some difficulties and some errors in the results, but all of them are expected. The classification in the 2nd dataset is a failure. There are too many errors in the result. Since there are many limitation of SAR/IfSAR by its nature, the detection of feature is limited and cannot comparable to the results from Lidar. Further more, in dense built-up areas, mutual intereference of the signals from building may hinder building extraction. Speckle is also the main problem for classification. It degrades the classification technique since the classification technique requires a speckle-free pixels distribution. The errors are also believed to be from the process of object merging-splitting. Having a bad feature extraction and inaccurate features statistic, the object merging-splitting process could render the worse result.

In spite of these limitations and difficulties, SAR/IfSAR can offer the opportunity to sense urban areas even in case of bad weather conditions, if Lidar is not operable. A combined analysis of SAR data from different aspects can enlarge the portion of reliable data. The evidence of the final results can be improved by mutual confirmation of segmentation results. Techniques for the fusion of knowledge from the different SAR/IfSAR data or even from the different sensors would provide a new aspect from mapping SAR/IfSAR in urban areas.

Chapter VII
Conclusion and Discussion

7.1 Summary of thesis

This research began by introducing concept and principles of SAR and IfSAR system. The SAR/IfSAR has strong advantages in its characteristics, which benefit the mapping in an urban area. Since the system is an active remote sensing, provide its own illumination, it can operate at any time of day. Moreover, the SAR signal is capable of penetrating through cloud or thick smoke. So, it can operate at any weather conditions.

The radar capability is very useful for mapping as it was demonstrated through past and present research. In some developing countries that are constantly subject to rain and cloud cover, the SAR/IfSAR may provide the only remotely sensed data available. Moreover, in urban area mapping, it is very difficult to fly the airborne photogrammetry during the date time since the air traffic is very congested, for example London. The only convenient period is during the night, which the photogrammetry is unlikely to be able to operate. Airborne SAR/IfSAR maybe the only convenient and economical choice of data acquisition technique.

Airborne SAR/IfSAR as a tool for urban area mapping was then addressed. Strong areas of interest appear to be in capability of SAR/IfSAR for features extraction and classifications. Further studies have demonstrated its benefits in urban classification. SAR/IfSAR cannot only distinguish between urban and non-urban regions, but also between features in the regions. However, most studies to date have used visual interpretation methods, which are time consuming and not based on a detailed theoretical analysis of the problem. Hence, the need for a detailed understanding of the data backscattering is needed.

The data model is, indeed, a vital clue for classification of the SAR data. Especially in an urban area, in which there are many types of features on the scene. There are many methods and models available for describing the SAR

data, the analysis for selecting suitable methods and models is required to get the accurate results. The information from the data model doesn't only provide the more thorough understanding of the SAR, but also plays as a key method for the object-oriented classification technique, in which data model is needed to described feature objects for classification.

Understanding the Characterisation of the SAR data is also important, in order to fully maximise information which contains in the data. The artefacts, effects, phenomenon contained in the data have been described and analysed. This shows the strong points and as well as the weak points, which can benefit the SAR processing in the way that it can be used directly or it needs to be fixed at first hand. Some effects like cardinal effect or dihedral corner reflection and coherent reflection effects are a very good indication of reflection from buildings even though, they cause problem with later processes.

Speckle is one of the most common artefacts occurred in radar imaging. There is a lot of information contained in speckle. But speckle causes troubles in feature extraction and classification. The speckle reduction is required in order to acquire more accurate results. Speckle has influences on edge detection and feature classification. It is necessary to reduce speckle in the scene before processing begins. Four speckle reduction techniques have been introduced and analysed in their performances. Each technique has its own advantages and disadvantages. Thus, it is important to choose the suitable speckle reduction technique for the processing and also for the end product.

The feature extraction process, which is the main processing on this research, consists of many steps of processing. Edge detection is the first processing procedure, in which adapted from the multi-step canny edge detection technique. The proposed technique used the constrained gradient-based edge detector, which responds as long as there are two gradients pointing in opposite directions, at each side of the current pixel. It is changed from normal canny edge detection to suit the SAR data set. But since the SAR image is very noisy, it results in many small spaghetti edges. The modified non-maximal technique is proposed to eliminate unwanted small edges. The edge detection plays a vital

rule in the processes since it is used as the seeded point for region growing for feature shaping and detection. The next step is to generate the bald earth DEM for subtracting from the original IfSAR DEM to get the "feature surface".

Height provided in IfSAR DEM is height of feature plus height of ground. In order to perform the feature extraction process, only height of feature is needed. There are many methods to calculate height of features from the IfSAR DEM. the method used in this research is to subtract the IfSAR DEM by the bald earth DEM, in which generated from the IfSAR DEM. Pyramid image and hierarchical interpolation techniques to generate bald earth DEM have been described. In each image level, calculation is made to select the ground pixels. Then those selected pixels are checked against other pixel from different level as well as against the original DEM. The bald earth DEM is the used to subtract from the IfSAR DEM to obtain the feature surface. On the feature surface, the region growing from edge detection is performed.

The region growing from edge detection performs by using the edges as the seeded points for the region growing on the feature surface. The parameters used on this operation are topographic structures. Since the edges are parts or boundaries, it is guaranteed those seeded points are correctly selected. Moreover, if an edge is detected from the noisy bits for the SAR intensity image when applying the region growing technique this type of edge doesn't provide any grown region. And this is a self-checking process. The result from the region-growing algorithm comes in the form of polygons for features. This region-growing step is a transformation from raster to vector format, which is more suitable for classification.

Classification proposed in this research is an object-oriented classification technique. The advantages and benefit of the techniques have been described. The technique classifies feature objects or polygons represent features instead of pixels by using the information from the data model. In most of the past researches data model has been used as a tool to describe a whole scene of SAR image. But in this research the data model has been used as a tool to describe a feature object. By analyse the data distribution of the feature object,

classifying applies by fitting the data distribution with a suitable PDF. From the results it has been found that log normal distribution is suitable for describing feature object represents building and gamma distribution is suitable for describing trees.

From the whole process in this research, it shows that an airborne SAR/IfSAR system can be used for mapping in an urban area at the medium scale mapping with any data fusion from other sensors.

7.2 Conclusions and Discussions

From the objectives stated in the first chapter, this research has been demonstrated that all of the four objectives can be completed. Features can be extracted from the methods of gradient-constrained edge detection, generation of bald earth DEM and region growing from edge detection. The extracted features are then classified by the techniques of object-based classification. And the map of the urban areas can be produced.

The major achievement of the research is that the generation of 3D city model of urban areas can be generated by using only airborne SAR/IfSAR data. And it also shows that the new developed techniques provide good performances and satisfactory results: the modified edge detection technique performs very well on the noisy SAR intensity image, the generated bald earth DEM could provide an accuracy around 1.8m compared with the reference DEM, the region-growing from edge detection technique developed by the author can cope with the problem of finding the seeded points and it is a process of transformation from raster to vector, object-based classification shows very promising results, even though some limitations. And it's all to show that SAR/IfSAR data can be used for mapping in urban areas.

It has been learned from this research that it is possible to extract features in an urban area from SAR/IfSAR data, but there are still limitations for mapping in urban. First of all, the resolution of the dataset used in the research is 5m both on the intensity image and IfSAR DEM, which is quite high compare to the size of features present in the scene. Details have been lost or compromised since the

data collecting process. In the dense built-up areas, a building could be smaller than the size of the resolution. The results are believed to be better if finer resolution data is obtained.

There are many artefacts appeared in SAR image, which are neither from incoherent geometric constraints or coherent constraints. These affect the feature extraction in dense urban areas from SAR image. It can be overcome by obtaining another scenes of SAR image of the same area from different angles, then, compared the suspected pixel whether it provides the same intensity value. Thus, the suspected pixel can be evaluated.

Speckle is also classified as artefact in SAR image even though it contains some information of the SAR scene. Speckle has influences in many steps of SAR processing. For example, speckle could lead to errors in phase unwrapping in a generation of IfSAR DEM, speckle could lead to errors in edge detection and also in feature classification. Speckle reduction is necessary and becomes a routine work as pre-processing step. There are many speckle reduction techniques, in which each one has its own strong and weak points. It is important to select a suitable technique for the process and the final product.

The feature extraction technique proposed here cannot extract feature that is flat or doesn't provide height, for example, road, walk way, etc. Apart from that it doesn't provide any height, this kind of feature, somehow, the return signal just blends in with the ground, which is difficult to distinguish it from the ground.

Due to the noisy nature of SAR/IfSAR data, the achieved level of detail was not comparable to the results from Lidar. Furthermore, in dense built-up areas, mutual interference of the signals from buildings may hinder building extraction. In spite of these limitations, IfSAR can offer the opportunity to sense urban areas even in case of bad weather conditions, if Lidar is not operable.

The DEM generated from IfSAR cannot still compete with DEMs derived from other methods, such as photogrammetry, Lidar or other optical sensors. But its potentials, weather independency and automation capabilities were shown. The SAR/IfSAR development is still continuing. The coming better

configuration and smaller resolution systems will help improving feature extraction in an urban area.

In the terms of feature extraction and feature classification, the result from feature extraction technique is quite good, even though there are some limitations as results of the characteristics of the dataset. The main features can be extracted quite successfully but poor results in extraction small features.

There is also a poor result in feature classifications. As stated in the Chapter 6, the classification technique requires a very precise histogram distribution of pixels in each feature. Since many features contain very small amount of pixels and there are some artifact pixels in the features, the precise histogram distribution cannot be generated, which leads to a poor classification result.

There are many new SAR/IfSAR systems with better characteristics. Some limitations can be overcome by better configurations of the systems. For example, with finer resolution, features can be clearer represented, leads to a more accurate feature extraction and feature classification. So, there are many developments in term of equipments and hardware. Thus, the developments in aspect of software are also needed. Future studies should concentrate on feature classification since a more accurate technique is still required. Object-based classification would still be a main concept but the classification rules need to be changed. Only the histogram distribution of the pixels is not enough, additional information is needed, such as coherent image or phase image.

In order to achieve a better result, somehow, a technique of data fusion might be another solution. Airborne SAR/IfSAR data merges with data from photogrammetry or Lidar, or multi-spectral image are believed to develop a more accurate result. But co-registration between dataset is needed and it also needs more financial support to buy additional dataset.

There are more and more people to join SAR/IfSAR processing, and more and more ready-to-use SAR/IfSAR data. This could benefit the community of SAR/IfSAR processing. SAR and SAR Interferometry can be another alternative technology for mapping in urban areas with the capability of

autonomous three-dimensional mapping for every weather condition, by day and night and at any season of the year.

Reference

Abramowitz 1970: Abramoqwitz, M., and Stegun, I.A., Handbook of Mathematical Functions, New York: Dover.

Abramowitz 1972: Abramowitz, M., Stegun I.A., Handbook of Mathematical Functions, Dover Publications, New York, 1972.

Armstrong and Griffiths 1991: Armstrong, B.C., Griffiths, H.D., Modelling Spatially Correlated K-Distributed Clutter, Electron. Lett., Vol.27, pp.1355-1356.

Beal et al., 1983: Beal, R.C., Tillet, D.G., Monaldo, F.M., Large and Small Scale Spatial Evolution of Digitally Processed Ocean Wave Spectral from SEASAT Synthetic Aperture Radar, J. Geophysical Research, Vol.88, No.C3, pp.1761-1768.

Bergholm 1987: Gergholm, F., Edge Focusing, IEEE trans. Pattern Anal., Mach Intell., Vol.9, pp.726-741.

Blacknell 1994: Blacknell, D., A Comparison of Parameter Estimators for the K-Distribution, LEE Proc. Radar Sonar Navig., Vol.141, pp.45-52.

Blacknell 1994: Blacknell D., Texture Anomaly Detection in Radar Imagery, European Conference on SAR Data Processing for Remote Sensing, Romte, SPIE Proceeding, Vol.2316, pp.125-136.

Booth 1969: Booth, R., The Weibull Distribution Applied to the Ground Clutter Backscatter Coefficent, US Army Missile Command, Tech. Repoart RE-TR-69-15, ASTIA Doc. AD 691109.

Burn et al 1986: Burns, J.B., Hanson, A.R., Riseman, E.M., Extracting Straight Lines, IEEE trans. Pattern Anal. March. Intell, Vol.8, pp.425-255.

Canny 1986: Canny, J., A Computational Approach to Edge Detection, IEEE Transactions on Pattern Analysis and Machine Intelligence, Vol.8, pp.679-698, 1986.

Clark 1989: Clark, J.J., Authenticating Edges Produced by Zero Crossing Algorithms, IEEE trans. Pattern Anal., March. Intell., Vol.11(1), pp.43-57.

Coleman, Mercer, 2002: Coleman, M.D., Mercer, J.B., NEXTMap Britain: Completing Phase 1 of Intermap's Global Mapping Strategy, GeoInformatics, December 2002, pp. 16-19.

Crimmins 1985: Crimmins, T.R., Geometric Filter for Reducing Speckle, Appl. Opt., Vol.24, pp.1438-1443.

Cumming 1989: Cumming, I., Gray, L., 1989, Interferometry Radar – A Better Tool for Exploration Geology, the 23rd International Symposium on Remote Sensing of Environment, Bangkok, pp. 1249-1262.

Cumming 1990: Cumming, I., Hawkins, D., Gray, L. 1990, All weather Mapping with Interferometric Radar, The 23rd International Symposium on Remote Sensing of Environment, Bangkok, pp.1249-1262.

Ding, Goshtasby 2001: Ding, L., Goshtasby, A., On the Canny Edge Detector, Pattern Recognition, Vol.34, pp.721-725.

Dobson 1995: Dobson, M.C., Ulaby, F.T., Pierce, L.E., Land-cover classification and estimation of terrain attributes using Synthetic Aperture Radar, Remote Sensing Environment 5, pp.199-214.

Dong et al 2000: Dong, Y., Milme, A., K., and Forster, B., C., A SAR Speckle Filtering Algorithm Towards Edge Sharpening, International Archives of Photogrammetry and Remote Sensing, Vol.333, Part B1, pp.89-95.

Dowman 1993: Dowman, I. 1993, The Current Status of Automated Cartography and Extraction of Global Topographic Data from Earth Observation Sensors, Workshop and Conference "International Mapping from Space", WG IV/2 ISPRS, Hannover.

Elachi, 1988: Elachi, C., 1988, Spaceborne Radar Remote Sensing: Applications and Techniques, IEEE press, New York.

Elder and Zycker 1998: Elder, J.H., Zucker, S.W., Local Scale Control for Edge Detection and Blur Estimation, IEEE trans., Pattern Anal., Mach Intell., Vol.20(7) pp. 699-716.

Evan et al 1988: Evans, D.L., Farr, T.G., Van Zyl, J.J. &Zebher, H.A., 1988, Radar Polarimetry: Analysis Tools and Applications, IEEE Trans. On Geoscience and Remote Sensing, Vol.26, No.6, Noverbmer 1988, pp. 774-789.

Fante 1984: Fante, R. L., Detection of Multiscatter Targets in K-distributed Clutter, IEEE trans., Antennas Propagation, Vol.32, pp. 1358-1363.

FAO 1993: Food and Agriculture Organisation of the United Nation 1993, Radar imagery: Theory and interpretation Lecture Notes, Remote Sensing centre, research and Technology development division, agriculture department, Rome, 1993.

Fay et al 1977: Fay, F.A, Clarke, J., Peters, R.S., Weibull Distribution Applied to Sea Clutter, Int. Conf. Radar'77, IEE conf. Pub. No.155, London: IEE, pp. 101-104.

Fisher and Dowman 2002: Fischer, P., Dowman, I., Validation of IfSAR Digital Elevation Models from Intermap Techonologies, Report for Norwich Union Insurance, Department of Geomatic Engineering, University College London.

Fisher et al 1987: Fisher, N., Lewis, T., and Embleton, J., J., B., Statistical Analysis of Spherical Data, Cambridge University Press.

Fornaro 1996: Fornaro, G., Franceschetti, G., 1996, Interferometric SAR Phase Unwrapping Using Green's Formulation, IEEE trans. on Geoscience and Remote Sensing, Vol.34, pp.720-727.

Forster 1994: Forster, B., 1994, SURV9600 Principle of Remote Sensing course notes 1994, School of Geomatic Engineering, University of New South Wales, Sydney, Australia.

Forster et al 1996: Forster,B.C., Ticehurst, C. & Dong, Y. 1996, Measures of Urban Morphology from Optical and Radar Sensors, Proc. Of the 8th Australasian Remote Sensing Conference, Canberra, Austrailia 25-29 March 1996, pp. 33-40.

Frisch: Frisch, U., Wave Propagation in Random Media, Probabilistic Methods in Applied Mathematics, Vol.1, A.T. Bharrucha-Reid (ed.), New York, Academic Press, pp.75-198.

Frost et al 1983: Frost, V., S., Shanmugan, K., S., and Holtzman, J., C., 1983, A Model for Radar Images and Its Application to Adaptive Digital Filtering of Multiplicative Noise, IEEE Transactions of Patter Analyses and Machine Intelligence, Vol. 4, pp.157-166.

Genderen 1997: van Genderen, Huang, Y., Gens, Y., van Veen, B., Huurneman, G., 1997, The ITC Filter for Improving ERS SAR Interferograms, Proc. 3rd ERS-1 Symposium, Florence.

Goldfinger, 1982: Goldfinger, A.D., Estimation of Spectra from Speckled Images, IEEE trans. Aerospace and Electronic Systems, Vol.AES-18, No.5, pp.675-681.

Goldstein 1988: Goldstein, R.M., Zebker, A., Werner, L., 1988, Satellite Radar Interferometry: Two-dimensional Phase Unwrapping, Radio Sci., Vol.23, No.4, pp. 713-720.

Goldstein et al 1990: Goldstein, R.M., Zebker, A., Werner, L., 1990, Satellite Radar Interferometry: Two-dimensional Phase Unwrapping, Radio Sci., Vol.23, No.4, pp.713-720.

Goodman 1976: Goodman, J.W., Some Fundamental properties of Speckle, J. Opt. Soc. Am. 66, pp. 1145-1149.

Goodman 1986: Goodman, J.W., 1986, A Random Walk through the Field of Speckle, Optical Engineering, Vol.25, No.5, pp.610-612.

Goodmand 1984: Goodman, J.W., Statistical Properties of Laser Speckle Patterns, Laser Speckle and Related Phenomena, J.C. Daintry (ed.), New York: Springer-Verlag, 1984, pp9-75.

Goshtasby and Shyu 1995: Goshtasby, A., Shyu, H-L., Edge Detection by Curve Fitting, Image Vision Comput., Vol.13(3), pp. 169-177.

Graham 1974: Graham L.C. 1974, Synthetic interferometric radar for topographic mapping, Proc. IEEE, vol. 62, pp. 763-768.

Guarieri 1993: Guarnieri, M.A, Parizzi, F., Pasquali, P., Prati, C., Rocca, F., 1993, SAR Interferometry Experiments with ERS-1, Proc. of IGARSS'93, Tokyo, pp. 991-993.

Haala 1999: Haala, N., Brenner, C., Extraction of Buildings and trees in urban environments, ISPRS Journal of Photogrammetry and Remote Sensing, Vol.54, pp.130-137.

Handerson and Lewis 1998: Handerson, F.M., Lewis, A.J., Principles and Application of Imaging Radar: Manual of Remote sensing, 3rd Edition, Vol.2, John Wiley & Son Inc, New York.

Haralic and Shapiro 1992: Haralick, R.M., Shapiro, L.G., Computer and Robot Vision, Vol.1, Addison-Wesley Publishing Company, ISBN 0-201-10877-1.

Haralick 1984: Haralick, R., Digital Step Edges from Zero Crossing of Second Directional Derivatives, IEEE trans. Patter Anal., March. Intell., Vol.6, pp. 58-68.

Hartl 1993: Hartl, P., Reich, M., Thiel, K.H., Xia, Y., 1993, SAR Interferometry Applying ERS-1 – Some Preliminary Test Results, Proc. Second ERS-1 Symposium, Hamburg, pp. 727-732.

Hartl 1995: Hartl, P., Wu, Xiaoqing, 1995, SAR Interferometry-Experiences with Various Phase Unwrapping Methods, Proc. 2nd ERS-1 Symposium, Hamburg, pp.727-732.

Heath et al 1997: Heath, M.D., Sarkar, S., Sanocki, T., Bowyer, K.W., A Robust Visual Method for Assessing the Relative Performance of Edge-Detection Algorithms, IEEE trans. Patter Anal., Mach. Intell, Vol.19(12), pp.1338-1359.

Hummel and Lowe 1988: Hummel, R., Lowe, D., From the Pixels to the Features. Computational Consideratoins in the Convolution and Feature Extraction in Images, Elsevier, Amsterdam.

Jahangir el al 1996: Jahangir, M.D., Blacknell, D., White, R.G., Accurate Approximation to the Optimum Parameter Estimate for K-Distributed Clutter, IEE Proc. Radar Sonar Navig, Vol.143, pp. 383-390.

Jakeman 1980: Jakeman, E., On the Statistics of K-Distributed Noise, J. Phys. A:Math. Gen., Vol.8, pp.31-48.

Jakeman 1980: Jakeman, E., Statistic of Integrated Gamma-Lorentzian Intensity Fluctuations, Opt. Acta, Vol.27, pp.735-814.

Jakeman and Pusey 1975: Jakeman, E., Pusey, P.N., Non-Gaussian Fluctuation in Eletromagnetic Radiation Scattered by a Random Phase Screen, J. Phys. A:Math. Gen. Vol.8, pp. 369-410.

Jakeman and Pusey 1976: Jakeman, E., Pusey, P.N., A Model for Non-Rayleigh Sea Echo, IEEE trans., Antennas Propagation, Vol.24, pp.806-814.

Jakeman and Pusey 1978: Jakeman, E., Pusey, P.N., Significance of K Distribution in Scattering Experiments, Phys. Rev. Lett., Vol.40, pp.546-550.

Jao 1984: Jao, J.K., Amplitude Distribution of Composite Terrain Radar Clutter and the K-Distribution, IEEE Trans. Antennas Propagation Vol.32, pp.1049-1062.

Joughin et al 1993: Joughin, I.R., Pericval, D.B., Winebrenner, D.P., Maximum Likelihood Estimation of K-Distribution Parameters for SAR Data, IEEE trans. Geoscience and Remote Sensing, Vol.31, pp.989-999.

Kenyi 1996: Kenyi, L., Raggam, H., Schardt, M., 1996, SAR Interferometry: Experiences with ERS-1/2 SLC Data, Oesterr, Zeitschrift fuer Verm.&Geo., Heft 2/96.

Kreithen 1991: Kreithen, D.E., Crooks, S.M., Irving W.W., Halversen S.D., Estimation and Detection Using the Product Model, MIT-Lincoln Lab. Report No.STD-3.

Kreithen et al 1991: Keirthen, D.E., Crooks, S.M., Irving, W.W., Halversen, S.D., Estimation and Detection Using the Product Model, MIT-Lincoln Lab. Report No.STD-37.

Kuan et al 1987: Kuan, D., T., Sawchuck, A., A., Strand, T., C., and Chavel, P., 1987, Adaptive Resotration of Images with Speckle, IEEE Transactions on Acoustic Speech and Signal Processing, Vol.35, pp.373-383.

Lacroix 1988: Lacroix, V., A Three Module Strategy for Edge Detection, IEEE trans. Pattern Anal., March. Intell., Vol.10, pp.803-820.

Lacroix and Acheroy 1996: Lacroix, V., Archeroy, M., Comstrained Gradient: Low-Level Tool for Feature Extraction, IAPR/TC-7 Workshop Remote Sensing and Mapping, Technical Univeristy of Graz.

Lacroix and Acheroy 1998: Lacroix, V., Archeroy, M, Feature Extraction using The Constrained Gradient, ISPRS Journal of Photogrammetry and Remote Sensing, Vol.53, pp.85-94.

Laur 1989: Laur, H., Analyse d'images radar en teledetection: discriminateurs radiometriques et texturaux, Ph.D. Thesis, Paul Sabatier University, Tolouse, France.

Laurence 1992: Laurence, A.G., Mattar, K.E., Farris-Manning, P.J., 1992, Airborne SAR Interferometry for Terrain Elevation, IEEE 1992.

Lee 1981: Lee, J., S., 1981, Refined Filtering of Image Noise Using Local Statistics. Computer Graphics and Image Processing, Vol. 15, pp.380-389.

Lee 1983: Lee, J., S., 1983, Digital Image smoothing and The Sigma Filter, Computer Vision Graphics and Image Processing, Vol.24, pp.225-269.

Lewis 1988: Lewis, P, On the Subject of Edge Detection, MSc. Thesis, University Of London.

Li 1998: Li, S.Z., Closed-form Solution and Parameter Selection for Convex Minimisation-Based Edge Preserving Smoothing, IEEE trans. Pattern Anal., Mach. Intell., Vol.20(9), pp.916-932.

Lin 1992: Lin, Q., Vesecky, J.F., Zebker, A., 1992, New Approaches in Interferometric SAR Data Processing, IEEE trans, on Geoscience and Remote Sensing, Vol.30, pp.506-567.

Lombardo 1995: Lombardo, P., Oliver, C.J., Tough, R.J., Effect of Noise on Order Parameter Estimation for K-Distributed Clutter, IEE Proc. Radar Sonar Navig., Vol.142, pp.33-40.

Lombardo and Oliver 1994: Lombardo, P., Oliver, C.J., Estimation of Texture Parameters in K-Distributed Clutter, IEE Proc. Radar Sonar Navig., Vol.141, pp.196-204.

Lombardo and Oliver 1994: Lombardo, P., Oliver, C.J., Simultaneous Segmentation of Texture Properties of K-Distributed SAR images, Euro Conf. on SAR Data Processing for Remote Sensing, Rome, SPIE Proc., Vol.2316, pp.104-114.

Lopes et al 1990: Lopes, A., Touzi, R., and Nezry, E., 1990, Adaptive Speckle Filters and Scene Heterogeneity, IEEE Transactions on Geoscience and Remote Sensing, Vol.28, pp.992-1000.

Lopes et al 1993: Lopes, A., Touzi, R., Nezry, E., and Luar, H., 1993, Structure Detection and Adaptive Speckle in SAR Images, International Journal of Remote Sensing, Vol.14, pp.1735-1758.

Lu et al 1998: Lu, Y., Kubik, K., Brnnamoun, M., An Accurate Approach to Localise House Areas for 3D Terrain Reconstruction. Proceesing of the 9th Australiasian Remote Sensing and Photogrammetry Conference, Sydney, Australia.

Luttrell 1990: Luttrell, S., P., An Adaptive Bayesian Network for Low-Level Image Processing, Proceeding the 3rd International Conference on Artificial Neural Networks, London, IEE, pp313-316.

Madsen 1986: Madsen, S.N., 1986, Speckle Theory, Ph.D. Thesis, Technical Univeristy of Denmark.

Marr 1982: Marr, D., J. Wilson and P. Monsour (Eds). Vision., W.H. Freeman, New York, pp.54-68.

Marr and Hildreth 1980: Marr, D., Hildreth, E., Theory of Edge Detection, Proc. Roy. Soc., London B-207, pp.187-217.

Mckeown 1990: Mckeown, M.D., Towards Automatic Cartographic Feature Extraction, L.F. Pau (Eds.), Mapping and Spatial Modelling for Navigation. Sptringer-Verlag, Berlin, NATO ASI Series, F65.

Mercer 1998: Mercer, J., B., Summary of Independent Evaluations of STATR-3i DEMs, www.intermap.ca.

Mercer and Gill 1998: Merver, J., B., Gill, M., Radar-Derived DEMs for Urban Areas, ISPRS Commission IV Symposium, Stuttgart, September 1998.

Mercer and Schnick: Mercer, J., B. & Schnick, S., Comparison of DEMs from STAR-3i, Interferometric SAR and Scanning Laser, www.intermap.ca.

Mercer and Schnick: Mercer, J.B., Schnick, S., Comarison of DEMs from STAR-3i Interferometric SAR and Scanning Laser, www.intermap.ca.

Moore, 1968: Moore, E.G., 1968. Side-looking Radar in Urban Research: A Case Study, Research Report 40, Northwestern University, Department of Geography, Evanston Ill.

Moreira et al 1995: Moreira, J., et al, X-SAR Interferometry: First Result, IEEE trans on Geoscience and Remote Sensing, Vol.33, pp.950-956.

Nasr & Vidal-Madjar, 1991: Nasr, J.M. & Vidal-Madjar, D. 1991, Image Simulation of Geometric Targets for Spaceborne Synthetic Aperture Radar, IEEE trans. on Geoscience and Remote Sensing, Vol.29, No.6, November 1991, pp. 986-996

Nevatia and Babu, 1980: Nevatia, R., Babu, K.R., Linear Feature Extraction and Description, Computer Graphic, Image processing, Vol.13, pp. 257-269.

Nicholas et al 1997: Nicholas, J.M., Sigelle, M., Thuillier, C., Tupin, F., Images de radar a' ouverture synthetique: transformee de Mellin et multiresolution, Proc. of the 16th conference GRETSI'97, Grenoble, France, September 15-19, 1997, pp.797-800.

Ogawa et al 1987: Ogawa, H.M., Sekine, M., Musha, T, Aota, M., Ohi,M., Fukushi,H., Weibull-Distributed Radar Clutter Reflected from Sea Ice, Trans IEICE Japan, Vol.E70, pp.116-120.

Oliver 1984: Oliver, C.J., A Model for Non-Rayleigh Scattering Statistics, Opt. Acta, Vol.31, pp.701-722.

Oliver 1985: Oliver, C.J., Correlated K-Distributed Clutter Models, Opt. Acta, Vol.32, pp.1515-1547.

Oliver 1986: Oliver C.J., The Interpretation and Simulation of Clutter Textures in Coherent Images, Inv. Problems, Vol.2, pp.481-518.

Oliver 1988: Oliver, C.J., Representation of Correlated Clutter in Coherent images, Inv. Problems, Vol.4, pp.843-866.

Oliver 1991: Oliver, C.J., Review Article Information from SAR Images, J. Phys. D: Appl. Phys., Vol.24, pp. 1493-1514.

Oliver 1993: Oliver, C.J., Optimum Texture Extimators for SAR Clutter, J. Phys. D: Appl. Phys., Vol.26, pp.1824-1835.

Oliver 1993: Olvier, C.J., Optimum Texture Estimators for SAR Clutter, J. Phys. D: Appl. Phys., Vol.26, pp.1824-1835.

Oliver 1994: Oliver, C.J., Edge Detectoin in SAR Segmentation, Europto Conf. on SAR Data Processing for Remote Sensing, Rome, SPIE Proc., Vol.2316, pp.80-91.

Oliver and Tough 1986: Oliver, C.J., Tough, R.J.A., On the Simulation of Correlated K-Distributed Random Clutter, Opt. Acta, Vol.33, pp.223-250.

Oliver and Quegan 1998: Oliver C., J., and Quegan S., Understanding Synthetic Aperture Radar Image, Artech House, London 1998.

Prati 1994: Prati, C., Rocca, F., Guarineri, A.M., 1994, SAR Interferometry Experiments with ERS-1, Proc. 1st ERS-1 Symposium, Cannes, pp.211-218.

Press et al 1994: Press, W.H., Teukolsky S.A., Vetterling, W.T., Flannery B.P., Numerical Recopes in C, Cambridge, UK, Cambridge University Press.

Pritt 1994: Pritt, D.M., Shipman, J.S., 1994, Least-Square Two-Dimesional Phase Unwrapping using FFT's, IEEE trans on Geoscience and Remote Sensing, Vol.32, pp. 706-708.

Pritt 1996: Pritt, D.M., Xia, Y., Kaufmann, H., Massmann, F.H., Timmen, L., Bodechtel, J., Frei, M., Impact of Precise Orbits on SAR Interferometry, Proc. of FRINCE'96, Unversity of Zurich-Irchel, Zurich.

Raghavan 1995: Raghavan, R.S., A Method for Estimating Parameters of K-Distributed Clutter, IEEE trans., Vol.AES-27, pp.238-246.

Robinson 1993: Robinson W.D., Reid, Graeme, T. (ed.), 1993, Interferogram Analysis Digital Fringe Pattern Measurement Techniques, Institute of Physics, London.

Rogers and Ingalls, 1969: Rogers, A.E.E. and R.P.Ingalls (1969) "Venus: Mapping the surface reflectivity by radar interferometry," Science, Vol. 165, pp. 797-799.

Santitamnont 1998: Santitamnont, P., 1998, Interferometric SAR Processing for Topographic Mapping, Wissenschaftliche Arbeiten, Der Fachrichtung Vermessungswesen Der Universitat Hannover, ISSN 0174-1454, Hannover, 1998.

Schleher 1975: Schleher, D.C., Radar Detection in Weibull Clutter, IEEE trans., Vol.AES-12, pp.736-743.

Schreier 1993: Schreier, G., SAR Geocoding: Data and Systems, Gunter Schreier (ed.), Karlsruhe, Wichman, 1993.

Schumann, 1996: ERS Applications to Forestry, Agriculture and Soil Moisture. Individual paper distributed at the 8th Australasian Remote Sensing Conference, Canberra.

Sekine et al 1979: Sekine, M., Ontani, S., Musha, T., Irabu, T., Kiuchi, E., Hagisawa,T., Tomita, Y., On Weibull-Distributee Weather Clutter, IEEE trans., Vol.AES-15, pp.824-830.

Sekine et al 1980: Sekine, M.T., Musha, T., Tomita, Y., Hagisawa, T., Irabu, T., Kiuchi, E., Log Weibull Distributed Sea Clutter, IEE Proc. F, Vol.127, pp.225-228.

Sekine et al 1981: Sekine, M., Ontani, S., Musha, T., Irabu, T., Kiuchi, E., Hagisawa,T., Tomita, Y., Weibull-Distributed Ground Clutter, IEEE, Trans., Vol.AES-17, pp. 596-598.

Sekine et al, 1983: Sekine, M., Musha, T., Tomita, Y., Hagisawa, T., Irabu, T, Kiuchi, E., Weibull-Distributed Sea Clutter, IEE Proc. F, Vol.130, p.476.

Shaw and Wheeler 1994: Shaw, G., and Wheeler, D., Statistic Techniques and Geographical Analysis, Chichester Wiley, 1994.

Shepard 1968: Shepard, D., A Two-dimensional interpolation function for irregularly-spaced data, Proceedings to the 23rd National Conference ACM, ACM, pp.517-524.

Soergel et al, 2000: Soergel, U., Thoennessen, U., Gross, H. and Stilla, U., Segmentation of Interferometric SAR Data for Building Extraction, International Archives of Photogrammetry and Remote Sensing.

Solaas 1994: Solaas, G.A., 1994, ERS-1 Interferometric Baseline Algorithm Verification, ES-TN-DPE-OM-GS02, Ver.1.0, ESA-ESRIN, Italy.

Stephens 1970: Stephens, M., A., Use of the Kolmogorov-Smirnov, Cramer-von Mises and Released Statistic Without Extensive Tables, Journal of Royal Statistical Soceity, Vol.32, pp.115-122, 1970.

Sties et al 2000: Sties, M., Kruger, S., Mercer, J.B., Schnick, S., Comparison of Digital Elevation Data from Airborne Laser and IfSAR Systerm, ISPRS Conference, Vol.XXXIII, Amsterdam, The Netherlands.

Sties et al 2000: Sties, M., Kruger, S., Mercer, J.B., Schnick, S., Comparison of Digital Elevation Data from Airborne Laser and interferometric SAR Systems. International Archives of Photogrammetry and Remote Sensing, Vol.33(3), pp.866-873.

Takajo88: Takajo, H., Takahashi, T., 1998, Non-iterative method for Obtaining the Exact Solution for the Normal Equation in Least-Squares Phase Estimation from the Phase Difference, J.Opt.Soc.Am.A, Vol.5, No.11, pp.1818-1827.

Takbasjsh et al 1994a: Tajbakhsh, S., Kim, M.-J., Berenyi, H.M., Burge, R.E., Applications of An Extended GTD Model to Synthetic Aperture Radar Simulation, Europto Conf. On SAR Data Processing for Remote Sensing, Rome, SPIE Proc., Vol. 2316, pp. 202-215.

Takbasjsh et al 1994b: Tajbakhsh, S., Kim, M.-J., Berenyi, H.M., Burge, R.E., Images of Urban Areas by a Synthetic Aperture Radar Simulator, Europto Conf. On SAR Data Processing for Remote Sensing, Rome, SPIE Proc., Vol.2316, pp.290-295.

Tao et al 2001: Tao, C.V., Wang, Y., Mercer, B., Zhang, Y., Automatic Reconstruction of Bald Earth Digital Terrain Models from Digital Surface Models Generated from an Airborne SAR System, Proceeding of the 3rd International Symposium on Mobile Mapping Technology, Cairo, Egypt, January 3-5, 2001.

Taylor 1972: Taylor, J., Scattering Theory, New York: Wiley, 1972.

Ticehurst 1998: Ticehurst, C., 1998, Development of Models for Monitoring the Urban Environment Using Radar Remote Sensing, UNISURV REPORT S-54, School of Geomatic Engineering, University of New South Wales, Sydney, Australia.

Trunk 1970: Trunk, G.V., George, S.F., Detection of Targets in Non-Gaussian Sea Clutter, IEEE trans., Vol.AES-6, pp.602-628.

Trunk 1972: Trunk, G.V., Radar Properties of Non-Rayleigh Sea Echo, IEEE trans., Vol.AS-8, 1972, pp.196-204.

Tsang et al 1985: Tsang, L., Kong, J.A., Shin, R.T., Theory of Microwave Remote Sensing, Wiley, New York, 1985.

Tur et al 1982: Tur, M., Chin, K.C., Goodman, J.W., 1982, When is Speckle Noise Multiplicative?, Applied Optics, Vol.21, No.7, pp.1157-1159.

Ulaby et al., 1981: Ulaby, F.T., Moore,R.K. & Fung, A.K., 1981, Microwave Remote Sensing: Active and Passive, Vol.1, 2 & 3 Addison-Wesley Publishing Company, Massachusetts, pp. 2162.

Ulaby, 1990: Ulaby, F.T., Elachi, C., Radar Polarimetry for Geoscience Applications, Artech House, Norwood, MA, 1990.

Ulupinar and Mdeioni 1990: Ulupinar, F., Medioni, G., Refining Edges Detected by a Log Operator, Comput. Vision, Graphics, Image Process., Vol. 51, pp.275-298.

Unser 1999: Unser, M., Splines: A Perfect Fit for Signal and Image Processing, IEEE Signal Processing Magazine, Vol.16, no.6, pp.22-38, November 1999.

Vachon 1987: Vachon, P.W., 1987, Synthetic Aperture Radar Imaging of the Ocean Surface: Theoretical Considerations and Experiments with Simulated and Actual SAR Imagery. Ph.D. Thesis, The University of British Columbia, Vancouver, BC, Canada.

Vachon and Raney 1988: Vachon, P.W., Raney, R.K., Estimation of SAR Transfer Fucntion through Processor Defocus, IEEE trans. on Geoscience and Remote Sensing, Vol.30, No.3, pp.627-630.

Valensuela 1972: Valensuela, G.R., Laing, M.B., Point-Scatterer Formulation of Terrain Clutter Statistics, Naval Research Laboratory Report 7459, Washington DC.

Van Zyl 1987: van Zyl, J.J., The effect of topography on radar scattering from vegetated areas, IEEE trans. Geoscience and Remote Sensing 24, pp.235-245.

Van Zyl 1993: van Zyl, J.J., Zebker, H.A., Elachi, C., Imaging Radar Polarisation signatures, Theory and Observation, Radio Sci., Vol.22(4), pp. 153-160.

Ward 1981: Ward, K.D., Compound Representation of High Resolution Sea Clutter, Electron, Lett., Vol.17, pp.561-565.

Ward 1982: Ward, K.D., A Radar Sea Clutter Model and Its Application to Performance Assessment, Int. Conf. RADAR'82, IEE conf. Pub. 216, London: IEE, pp.203-207.

Warden 1970: Warden, M.P., An Experimental Study of Some Clutter Characteristics, AGARD Conf. Proc. on Advanced Radar Systems, No.66.

Watts 1987: Watts, S., Radar Detection Prediction in K-Distributed Sea Clutter and Thermal Noise, IEEE, trans. AES, Vol.23, pp.40-45.

Whitt et al 1990: Whitt, M.W., Ulaby, F.T. and Sarabandi, K., Polarimetric Scatterometer Systems and Measurements, Radar Polarimetry for Geoscience Applications, Norwood, MA: Artech House, 1990, pp. 191-272.

Xia & Henderson, 1997: Xia, Z.G., Henderson, F.M. 1997, Understanding the Relationships, between Radar Response Patterns and the Bio- and Geophysical Parameters of Urban Areas, IEEE trans. on Geoscience and Remote Sensing, Vol.35, No.1, January 1997, pp. 93-101.

Xia, 1996: Xia, Z.G., 1996, Applications of Multi-Frequency, Multi-Polarisation and Multi-incident Angle SAR Systems in Urban Land Use and Land Cover Mapping, Proc. of IGARSS'96, Lincoln, USA, 27-31 May 1996, Vol.4, pp.2310-2314.

Xiaopen et al: Xiaopeng, L., Baker, A.B., Dickenson, G., Accuracy Assessment of Mapping Products from the STAR-3i Airborne IfSAR System, www.intermap.ca.

Yueh et al 1989: Yueh, S.H., Kong, J.A., Jao, J.K., Shin, R.T., Novak, L.M., K Distribution and Polarimetric Terrian Clutter, J. Electromagnetic Waves and Appl., Vol.3, pp. 747-768.

Zebker 1986: Zebker, H.A., Goldstein, R.M., 1986, Topographic Mapping from Interferometric Synthetic Aperture Radar Observation, JGR, Vol.91, No.B5, pp.4993-4999.

Zebker 1987: Zebker, H.A., van Zyl, J.J., Held, D.N., Imaging Radar, Polarimetry from Wave Synthesis, J. Geophys. Res. 92(1), pp.638-701.

Zebker 1992: Sebker, A., Villasenor, J., Madsen, S.N., 1992, Topographic Mapping from ERS-1 and SEASAT Radar Interferometry, IEEE trans. on Geoscience and Remote Sensing, pp. 387-388.

Zebker 97: Zebker, H., Lu, Y., 1997, Phase Unwrapping Algorithms for Radar Interferometry, Residue-cut, Least-Squares and Synthesis Algorithms, Submitted to JOSA-A.

Zhang and Tao 1999: Zhang, Y. and Tao, V.C., Automatic Reconstruction of Ground DEMs from Airborne SAR DSMs. International Project Report, Department of Geomatics Engineering, The University of Calgary.

Ziou 2001: Ziou, D., The Influence of Edge Direction on the Estimation of Edge Contrast and Orientation, Pattern Recognition, Vol.34, pp.855-863.

Zisk 1972: Zisk, S.H., A new Earth-based radar technique for the measurement of lunar topography, Moon, Vol.4, pp. 296-300, 1972.

Appendix

1. Algorithms used in this thesis

1.1 Speckle Reduction Techniques

- Multilook Processing
- Lee-sigma Filter
- Frost Filter
- Gamma-Map Filter
- Local Region Filter

1.2 Edge Detection

- Adopted Canny Edge Detection (Ding and Goshtasby 2001)
- Constrained Gradient-based Edge Detection (Lacroix and Acheroy 1998)
- Constrained Gradient-based Corner Detection (Lacroix and Acheroy 1998)
- Non-Maximal (Lewis 1988)

1.3 Generation of Bald Earth DEM

- Generation of Bald Earth DEM by Hierarchical surface Fitting
- Generation of Image Pyramid
- Hierarchical Interpolation of Bald Earth DEM
- Interpolation of Bald Earth Surface by Inverse Distance Weighted (IDW)

1.4 Region Growing from Edge Detection

- Region Growing using Edge as Seeding Point
- Using Mathematical Properties of Topological Structure as main parameters

1.5 Object-oriented Classification

- Texture analysis from Data Model
- Object-oriented Classification

1.6 Classification

- Classify by Fitting
- Direct Classification